Artificial Neural Network Treatment Of Casson Fluid Flow Over Radially Stretching sheet

A thesis submitted to
NATIONAL INSTITUTE OF TECHNOLOGY WARANGAL, (T.S.)
for the award of the degree of
DOCTOR OF PHILOSOPHY
in
MATHEMATICS

by
SHRAVAN KUMAR . R
(Roll No. 718161)

UNDER THE SUPERVISION OF
Prof. D. SRINIVASACHARYA

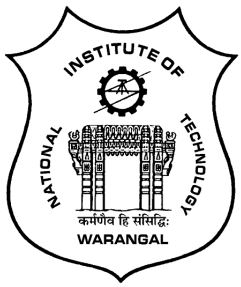

DEPARTMENT OF MATHEMATICS
NATIONAL INSTITUTE OF TECHNOLOGY
WARANGAL - 506 004, INDIA

MARCH 2023

C E R T I F I C A T E

This is to certify that the thesis entitled " **Artificial Neural Network Treatment Of Casson Fluid Flow Over Radially Stretching Sheet** " submitted to National Institute of Technology Warangal, for the award of the degree of ***Doctor of Philosophy***, is the bonafide research work done by **Mr. SHRAVAN KUMAR . R** under my supervision. The contents of this thesis have not been submitted elsewhere for the award of any degree.

Dr. D. Srinivasacharya
Professor
Department of Mathematics
National Institute of Technology,
Warangal, T.S., INDIA

.

Dedicated to

My Parents

R. Purushotham Sharma , Vijaya

&

Lord Sri Lakshminrusimha Swamy(Sundilla)

ACKNOWLEDGEMENTS

It is a rare privilege and boon that I could associate myself with Dr. D. Srinivasacharya, Professor of Mathematics, National Institute of Technology Warangal, India, for pursuing my research work. I sincerely record my gratitude for his invaluable guidance and constant encouragement throughout the preparation of this thesis and his involvement and meticulous supervision while my work was in progress. With his inimitable qualities as a good teacher, he chiseled my path towards perfection. He has been a perpetual source of inspiration, spiritual guidance, encouragement, and enlightenment since I first met him. He is the one who ensured that the duration of my research work was both educational and fun. He has been a great source of motivation and inspiration. The thesis would not have seen the light of the day without his unrelenting support and cooperation. I deem it a privilege to have worked under his amiable guidance. My vocabulary is inadequate to express my gratitude.

I am grateful to Prof. H. P. Rani, Head, and Dr. P. Muthu former Head, Department of Mathematics for providing necessary help and support throughout my research period.

I take this opportunity to thank Prof. Y. N. Reddy, Prof. Debashis Dutta and Prof. J. V. Ramana Murthy, Department of Mathematics for their valuable suggestions, moral support and encouragement during my stay.

I thank the members of the Doctoral Scrutiny Committee, Prof. K. N. S. Kasi Viswanadham and Dr. Ch. Ramreddy, Department of Mathematics, and Dr. S. Sreenath, Department of Chemical Engineering for their valuable suggestions, moral support, and encouragement while my work was in progress.

I place on record my gratitude to all the faculty members of the Department of Mathematics, for their constant encouragement.

I express my sincere thanks to the Director, National Institute of Technology, Warangal for providing me Fellowship (GATE) to carry out my research work.

I thank Dr. Pavankumar Reddy, Dr. Shivakumar Reddy, Dr. Dipak Barman, Dr. Abhinav Srivasthav, Dr. K. Sita Ramana, Mr. Atul Kumar Srivastva, Mr. B. Rajendar, Ms. Nidhi Humnekar, Mr. Harlal, Mr. Subhabratha Rath, Mr. Bikas Modak, Mr. Naresh and all other research colleagues in the Department of mathematics and my friends, who helped me during my Ph.D. for being cooperative and also for making my stay in the NITW campus fruitful and enjoyable every moment.

My heartfelt gratitude goes to my parents, R. Purushotham Sharma and Smt. R. Vijaya, whose encouragement and blessings inspired me to finish my job ahead of schedule. I am overjoyed to thank my family members for their contributions to the completion of this job. All of their prayers, support, love, and affection have been the driving force behind what has happened.

My thanks, choked with emotion, to my innocent Son, Arihanth and Daughter, Anupama for their understanding and adjustment while I missed them, when I was engrossed in my research. Also, most importantly, I would like to thank my better half, Deepika for her support, prayers, patience and understanding that were vital to complete this thesis. Without her help and encouragement, I would not have been finished this thesis. I thank to my extended Family consisting of My Brothers Swaroop and Sujith and family, for their continuous support and constant encouragement over the years. All of their love and affection have been motivating force behind what I am today.

Shravan Kumar . R

A B S T R A C T

In recent years, among the diverse machine intelligence approaches, artificial neural network (ANN) methods have emerged as powerful tools for solving differential equations emanating from engineering challenges. In most of the studies on the boundary layer flows, the authors used ANN to train the numerical values obtained by using computational methods and to calculate the skin friction coefficient, Nusselt number, and Sherwood number. Here, in this study we have not used predefined data in finding the solution. The purpose of this thesis is to study the applicability of Artificial Neural Networks for the Casson fluid flow over Radially stretching sheet.

This thesis consists four Parts and ten chapters. Part - I consists of a single chapter which is devoted to the basic concepts and a review of the pertinent literature. Part-II contains four chapters (i.e. chapters 2, 3, 4 and 5) and deals with the Casson fluid flow past an unsteady radially stretching surface with Soret and Dufour effects, bioconvection effect and magnetic field and chemical reaction on entropy generation. Part-III, which consists of the chapters 6, 7, 8 and 9, is devoted to study the Casson fluid flow across a steady radially stretching surface in the presence of an magnetic field and thermal radiation, chemical reaction and viscous dissipation, motile microorganisms bioconvection and magnetic field and viscous dissipation on entropy generation.

In all the above chapters the partial differential equations governing the flow are transformed into a system of non-linear ordinary differential equations via similarity transformations. Artificial neural networks are then used to compute the solution to these nonlinear ordinary differential equations. A multi-layer perceptron neural network with adjustable parameters (the biases and weights) is used in the trial functions. The Adam optimization algorithm is adopted to determine adjustable parameters of the trial solution. The present results are compared to the results of published works as well as the shooting method and found to be in good agreement. An extensive quantitative analysis has been performed based on numerical results in order to estimate the efects of pertinent parameters on various physical quantities by means of their graphical representations

Part - IV consists of a single chapter, i.e. Chapter - 10, which consists of the main conclusions of the thesis and the directions in which further investigations may be carried out.

NOMENCLATURE

C	Fluid concentration.
C_f	Skin friction.
c_p	Specific heat capacity.
C_w	Concentration at the surface
C_∞	Free stream concentration.
D_s	Diffusion coefficient.
D_m	Motile diffusion coefficient.
f	Dimensionless function.
g	Acceleration due to gravity.
k	Thermal conductivity.
$\mathbb{N}$	Bioconvection
N_u	Nusselt number.
$\mathbb{N}_\infty$	Free stream density of motile microrganism.
P_e	Bioconvection Peclet number.
Pr	Prandtl number.
q_m	Mass flux.
q_n	Motile microorganism flux.
q_w	Heat flux.
R_e	Reynolds number.
S	Suction/Injection parameter.
Sb	Bioconvection Schmidth number.
Sc	Schmidth number
Sh	Sherwood number
T	Fluid Temperature.
T_w	Surface Temperature.
T_∞	Free stream temperature.
U_w	Stretching velocity.

Greek Symbols

β	Casson fluid parameter.
β_T	Thermal expansion coeeficient.
β_C	Concentration expansion coefficient.
β_N	Bioconvection expansion coefficient.
χ	Dimensionless Bioconvection variable
η	Non-dimensional variable.
λ_C	Concentration buoyancy parameter.
λ_T	Thermal buoyancy parameter.
λ_N	Bioconvection buoyancy parameter.
ρ	Density of the fluid.
σ	Sigmoid activation function.
θ	Dimensionless temperature.
μ	Dynamic Viscosity of the fluid.
ν	Kinematic viscosity.
τ_w	Shear stress.
α	Thermal Diffusivity
ψ	Stream function.
ϕ	Dimensionless Concentration
σ_b	Dimensioless bioconvection constant.

Subscripts

w	wall condition.
∞	Ambient condition.

Contents

[1] Communicated to "**Engineering Transactions**"

[2] Published in "**Journal of Thermal Analysis and Calorimetry**", 22 (2021): 100830

[3] Communicated to" **Heat Transfer**"

[4]Communicated to "**Mathematical Methods in the Applied Sciences**"
[5]Communicated to "**Arabian Journal for Science and Engineering**"
[6]Communicated to "**Journal of Applied Mathematics and Computing**"
[7]Communicated to "**International journal of Applied and Computational Mathematics**"

[8] Communicated to "**Engineering Applications of Computational Fluid Mechanics**"

Chapter 1

Preliminaries and Review

1.1 Introduction

Fluid mechanics deals with the behavior of liquids and gases at rest or in motion. It stands central to much of science and engineering and impacts defense, transportation, manufacturing, environment, medicine, energy, etc. It encompasses a vast variety of practical problems ranging from the flow of blood in capillaries to flow of oil in huge pipelines and from the flight of birds to supersonic flights of airplanes. This subject has established itself as a challenging and exciting subject of modern sciences due to its applications in every aspect of our daily lives. The pursuit of a profound knowledge about the topic has not only stimulated the development of the subject itself but has additionally proposed the progress in the supporting areas, such as applied mathematics, numerical computing, and experimental techniques.

Fluid flow problems are governed primarily by non-linear differential equations. It is usually not possible to solve these non-linear differential equations analytically, necessitating the use of a special method. Unfortunately, not every non-linear differential equation can be solved using a single numerical technique. Some of the popular methods that are

available to solve these non-linear differential equations are Homotopy Perturbation Method [28], Parameterized Perturbation Method [27] Homotopy Analysis Method [44], Adomian Decomposition Method [2] , and Variational Iteration Method [26]. Although these methods are extremely powerful and can deal with a wide range of nonlinear differential equations, they have some limitations and drawbacks. Computational Fluid Dynamics (CFD) is a subset of fluid dynamics research that focuses on modelling different types of fluid flows using computer simulations and the aforementioned special techniques. It has been used to create simulations of annealing, civil engineering, and weather predictions by utilizing the ability of computers to achieve more efficient computation. Recently, researchers in the field of fluid dynamics have been examining neural networks and their ability to solve challenging problems quickly. The Feed Forward Neural Network has been the most widely used model to date. This model takes several inputs, then passes the data through hidden layers to generate an output. Backpropagation is a technique used by the network to optimise its output. This method modifies the weights of specific "neural pathways" to make them more influential on the final output.

1.2 Artificial Neural Networks

An Artificial Neural network (ANN) is a mathematical model or computational model that simulates the computational model like the biological neural networks. It consists of an interconnected artificial neurons and processes information using a connectionist approach. Neural networks, like human brains, can learn complex patterns by adjusting the strength of connections between neurons. Neural networks, in principle, are large, parameterized functions with some very useful properties. In most cases an ANN is an adaptive system that changes its structure based on external or internal information that flows through the network during the learning process.

1.2.1 Architecture

Neural networks are defined by the weights of the connections between neurons and the biases of these neurons. ANNs perform factual computation by means of weighted connections, which are hidden in one or more layers. Each neuron evaluates the weighted average of its input neurons and weights, adds its bias to the result, and feeds the resulting value through a nonlinear activation function. Other than these components, all neural networks also have an input layer and an output layer.

Feed forward neural networks are the most basic type of artificial neural network. The feed forward neural network was the very first and admittedly easiest kind of artificial network developed. Neurons in a feed-forward neural network are organised in layers. Neurons in a layer gain the previous layer's input and send their results to the subsequent layer. Network connections to the same or previous layers are not permitted. The data is fed from the input node to the output node in an exclusively feed-forward manner. The outcome of any layer doesn't really influence the same layer. The following figure 1.1 shows the block diagram of the feed-forward neural network.

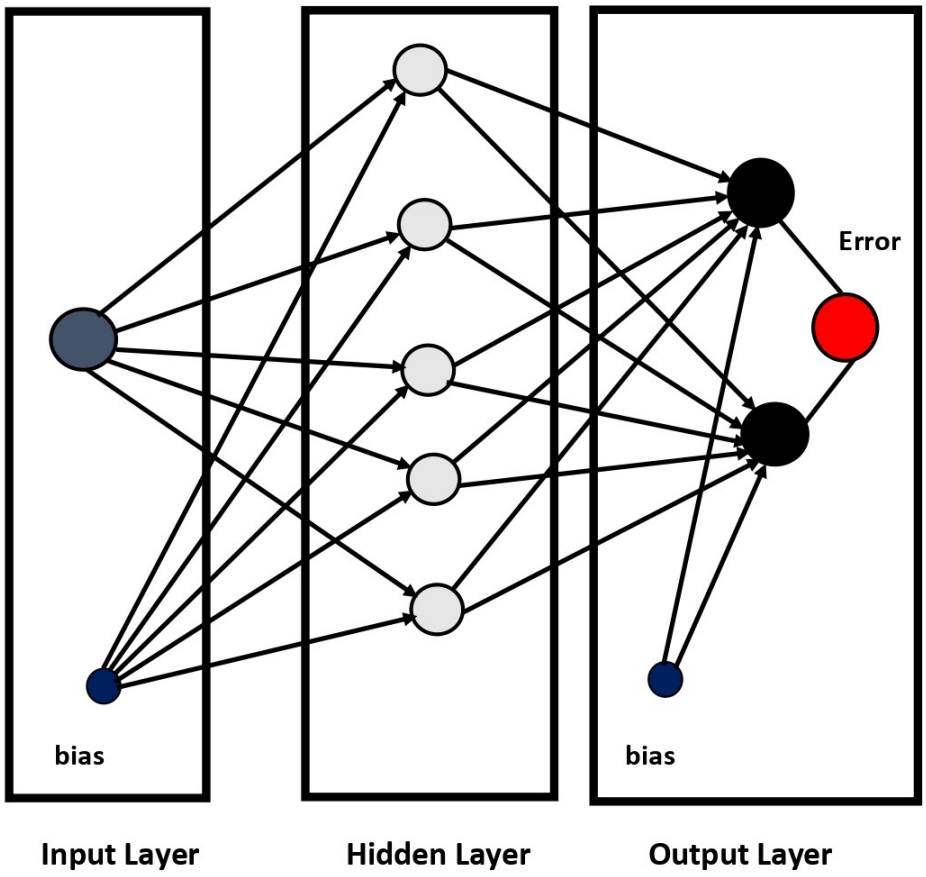

Figure 1.1: Feed Forward Neural Network

The most frequent type of feed forward network is the multi-layer perceptron (MLP). The multilayer perceptron is the most basic deep neural network configuration. All neurons in such neural networks are arranged in ordered layers, and each neuron is connected to all neurons in neighbouring layers. In ANNs, learning is accomplished using specific training procedures that are expanded in line with the learning rules

1.2.2 Universal approximation

An artificial neural network can perform a nonlinear mapping from the inputs to the outputs of the corresponding system of neurons, which is useful for analysing problems characterised by initial/boundary value problems that have no analytical solutions or are difficult to com-

pute. The global approximation of a real valued multi-variable function in a closed analytic form is one of the applications of the multilayer feed forward neural network. Such neural networks are known as universal approximators. It has been discovered in the literature that multilayer feed forward neural networks with one hidden layer and arbitrary squashing functions are capable of estimating any Borel measurable function with any desired degree of accuracy from one finite dimensional space to another.

It has been shown that feedforward neural networks are able to approximate any function arbitrarily well given sufficient neurons and when using certain activation functions [29]. This property makes neural networks very powerful tools in theory. It has also been shown by Hornik *et al.* [30] that when the activation function is sufficiently differentiable, then neural networks can simultaneously approximate the function and its derivatives arbitrarily well . This property is important in the setting of solving differential equations.

1.2.3 Loss function

The difficulty in using neural networks is determining weight sets that produce accurate approximations. No direct methods to find such weights appear to exist. Hence, the problem of finding good weights can be converted into a minimization problem by defining a kind of distance measure between the parametrized function that a neural network defines and the function one intends to approximate. Such distance measures are known as loss functions. Let the input vector be $\mathbf{x}$ and θ be the set of weights and biases of the neurons. A neural network defines a function $f(\mathbf{x}, \theta)$, where f has same dimension as the number of neurons int he output layer. Let $\mathbf{g}(\mathbf{x})$ be $n-$ dimensional scalar function to be approximated and known through the input-output pairs $(\mathbf{x}_i, y_i), i = 1, 2, \cdots N$. Now, it is simple to obtain a loss function by computing the mean square error as

$$L(\theta) = \frac{1}{N} \sum_{i=1}^{N} (f(\mathbf{x}_i, \theta) - y_i)^2$$

Minimizing such a loss function is called training. For notational convenience, let us arrange the parameters contained in θ in a vector, denoted by θ. The only requirement for loss functions is that their minima correspond to accurate approximations; they do not need to be true distance measures. Although some of minimization algorithms, viz, Stochastic Gradient Descent, ADAM, Broyden-Fletcher-Goldfarb-Shanno algorithm etc., are general-purpose optimization algorithms and can be used in other contexts, they gained popularity through neural networks. One among them is ADAM algorithm

1.2.4 ADAM Optimization

Adaptive Moment Estimation (ADAM) [38] is one of the most common training algorithms for neural networks. It is first order gradient based optimization method. Adam uses an exponential moving average of the gradients with respect to the network parameters to update these parameters. Furthermore, the algorithm reduces the learning rate based on an exponential moving average of the variance of these gradients, such that noisy loss functions are more carefully traversed. Being computationally efficient, ADAM requires less memory and outperforms on large datasets. It combines the advantages of AdaGrad(which works well with sparse gradients) and RMSProp (which works well in non-stationary settings)

Let α denote the learning rate and $\mathbf{m}_i$ denote the moving average of the gradients and $\mathbf{v}_i$ denote the moving average of the variance of the gradients, These moving averages decay with rates β_1 and β_2 respectively. Then, the i^{th} iteration of Adam takes the form

$$
\begin{aligned}
&\mathbf{g}_{i+1} = \nabla L(\theta_i), \\
&\mathbf{m}_{i+1} = \beta_1 \mathbf{m}_i + (1-\beta_1)\mathbf{g}_{i+1}, \\
&\mathbf{v}_{i+1} = \beta_2 \mathbf{v}_i + (1-\beta_2)\mathbf{g}_{i+1} \odot \mathbf{g}_{i+1}, \\
&\hat{\mathbf{m}}_{i+1} = \frac{\mathbf{m}_{i+1}}{(1+\beta_1^{i+1})} \\
&\hat{\mathbf{v}}_{i+1} = \frac{\mathbf{v}_{i+1}}{(1+\beta_2^{i+1})} \\
&\theta_{i+1} = \theta_i - \alpha \hat{\mathbf{m}}_{i+1} \oslash (\sqrt{\hat{\mathbf{v}}_{i+1}} + \epsilon)
\end{aligned}
\tag{1.1}
$$

Here $\odot$ and $\oslash$ denote Hadamard multiplication and division respectively, whihc are elementwise operations. The square root is also applied elementwise.

1.3 Artificial Neural Network Method for Solving Differential Equations

1.3.1 Advantages in ANN method

A neural network study for differential equation provides some advantages over the existing numerical methods. ANN can be seen as an effective alternative to analytical and numerical approaches that do not involve the solution of complex mathematical concepts. It can be used as a powerful tool to tackle complicated engineering challenges in a variety of real-world applications with considerable cost and time savings

- Trial solutions of ANN include a single independent variable regardless of the dimension of the problem.
- The method is general and can be applied to ordinary differential equations (ODEs), systems of ODEs and to partial differential equations (PDEs) as well.
- The required number of model parameters is far less than any other solution technique and therefore, compact solution models are obtained, with very low demand on memory space.
- The method is general and can be applied to the systems defined on irregular arbitrary shaped boundaries.
- The method can be realized in hardware, using neuroprocessors, and hence offer the opportunity to tackle in real time difficult differential equation problems arising in many engineering applications.
- The method can also be implemented on parallel architectures.

There are different neural network methods for the solutions of differential equations. Feed forward neural networks [41] in which the information moves in only one direction forward from the input nodes to output nodes. Recurrent neural networks [5, 43] in which information can go back from output nodes to input nodes. Radial basis function networks [42] in which three layers (input layer, basis function layer as hidden layer, output layer) exist where each node in the hidden layer represents a Gaussian basis function for all nodes and output node have a linear activation function Hopfield network [94, 90] in which a set of neurons with unit delay is fully connected to each other and forming a feedback neural network. Cellular network [15, 31] which features a multidimensional array of neurons and local interconnections among cells. Finite element neural network [95] have the finite element model converted into the parallel network form. Wavelet element network [47] which is an alternative to feed forward neural network for approximating arbitrary nonlinear functions as an alternative and have waveleons instead of neurons.

Among these neural network methods, feed forward neural networks are popular tools due to their structural flexibility, good representation capabilities and availability of a large number of training algorithms. The primary objective of ANNs is to simulate a trial solution based on the function estimation competence of feed-forward neural networks and yields in the development of the solution. The square of the difference between the exact solution and constructed solution gives rise to an error and thus reflects some resemblance to the loss function of a neural network. The parameters of the feed-forward neural network (biases and weight) are to be modified or trained to minimize the error (loss). For this optimization techniques are to be employed which involve error gradient calculation with respect to neural network and inputs parameters.

We consider an artificial feedforward neural network (ANN) with n inputs, m outputs and a single hidden layer with k units. The output of the network, $N_m(\bar{\eta}, \{w, \bar{b}\})$ can be written as

$$N_m(\bar{\eta}, \{w, \bar{b}\}) = \Sigma_{k,n} w^f_{mk} \sigma\{w^h_k \eta_n + b^h_k\} + b^f_m \tag{1.2}$$

where the activation function σ is the sigmoid activation function which is applied element wise to each unit, and h and f are hidden and final layers, respectively. To forecast solutions

to m linked differential equations, we employ a single neural network with m outputs.

A set of m coupled j^{th} order differential equations can be expressed in the general form,

$$F_m(\bar{x}, \phi_m(\bar{x}), \nabla\phi_m(\bar{x}), ..., \nabla^j\phi_m(\bar{x})) = 0 \tag{1.3}$$

with boundary or initial conditions imposed on the solutions $\hat{\phi_m}(\bar{x})$. Writing the differential equations in such a way allows us to easily convert the problem of finding a solution into an optimization one. An approximate solution $\hat{\phi_m}(\bar{x})$ is one which approximately minimizes the square of the left-hand side of (1.3), and thus the analogy can be made to the loss function of a neural network.

In previous approaches ([41], [48], [40]) is the trial solution $\hat{\phi_m}(\bar{x})$ was considered as the sum of two terms, the first of which satisfies the conditions on the boundary and the second of which is related to the neural network parameters. This, however, necessitates the selection of a specific type of initial solution that is reliant on the conditions on the boundary. For certain boundary conditions, choosing such an initial/trial solution is very difficult. Instead, Piscopo *et al.* [65] proposed the trial solution as the network output $\hat{\phi_m}(\bar{x}) \equiv N_m(\bar{\eta}, \{w, \bar{b}\})$ and included the boundary conditions in the loss function as additional terms. If the domain is discretized into a finite number of training points $\bar{x}^i$, then approximations to the solutions, $\hat{\phi_m}(\bar{x})$, can be obtained by finding the set of weights and biases, $\{w, \bar{b}\}$, such that the neural network loss function is minimized on the training points. For i_{max} training examples, the full loss function that we use is

$$\mathfrak{E}(\{w, \bar{b}\}) = \frac{1}{i_{\max}} \sum_{i,m} \hat{F}_m(\bar{x}^i, \hat{\phi}_m(\bar{x}^i), ..., \nabla^j\hat{\phi}_m(\bar{x}^i))^2 + \sum_{B.C} (\nabla^p\hat{\phi}_m(\bar{x}_b) - K(\bar{x}_b))^2 \tag{1.4}$$

where the second term represents the sum of the squares of the boundary conditions, defined at the boundaries $\bar{x}_b$. These can be Dirichlet or Neumann, or they can be initial conditions if defined at the initial part of the domain.

The problem is then to minimize $\mathfrak{E}(\{w, \bar{b}\})$ by optimizing the weights and biases in the network, for a given choice of network setup. To calculate the loss, it is necessary to

compute the derivatives of the network output with respect to its input. Since each part of the network, including the activation functions, are differentiable, then the derivatives can be obtained. The optimization can then proceed via backpropagation by further calculating the derivatives of the loss itself with respect to the network parameters.

As with any neural network, the choice of hyperparameters will have an effect on the performance. For our setup, the important parameters are the number of hidden layers, the number of units in each hidden layer, the number of training points $\bar{x}^i$ (corresponding to the number of anchors in the discretization of the domain of the differential equation), the sigmoid activation function in hidden layer, the optimization algorithm, and the learning rate. The benefits of ANN is that the output of the network for selective number of points can be used to find out the outcome for any other new point using the same parameters for interpolation and extrapolation.

1.4 Casson fluid

Most of the fluids that encounter in industrial form or physical, other than water and air, are non-Newtonian fluids. The research on non-Newtonian fluid flow stimulated the interest of various investigators owing to its application to a wide range of engineering challenges, including crude oil extraction from petroleum products, the creation of plastic materials, material processing, crystal growing, cooling of nuclear reactors, movement of biological fluids, and the production of syrup medications. There is no unique fluid model that accurately depicts all non-Newtonian fluid properties. Therefore, during the last century, several fluid models, including power-law fluids, Williamson fluid, Jaffery fluid, couple stress fluids, micro-polar fluids, and so on to characterize the real fluid behavior were being reported in the literature. The governing equations for Non-Newtonian fluid flows are much more complex, and modeling the flows of such fluids yields higher order, nonlinear, coupled partial differential equations when compared to the analogous flows of a viscous fluid.

The Casson fluid model, proposed by Casson in 1959 [13], belongs to the category of

non-Newtonian fluid models. Casson fluid is a shear-thinning fluid with a yield stress below which no flow occurs, infinite viscosity at zero shear rate, and a no viscosity at an infinite shear rate. It gives a convenient approach for determining the two parameters, apparent yield stress and Casson viscosity, for practical applications. Over the last few years, a wide range of theoretical and computational research has been reported using the Casson fluid model owing to its vast applications in drilling operations, metallurgy, food processing, manufacturing of pharmaceutical products, synthetic lubricants, polymer processing industries, preparation of printing ink, biomedical field, etc.

1.5 Basic Terminology

Convective Heat Transfer

The exchange of internal energy between particular constituents or regions of the medium under consideration is referred to as heat transfer. It always happens in a downward direction from a higher to a lower temperature location. There are three modes by which heat transfer occurs. They are conduction, convection, and radiation. The molecular transport of heat in bodies or between bodies in the thermodynamical system is referred to as conduction. Heat transfer caused by the movement of fluid from one region of the medium to another is called convection. Radiation heat transfer is a mechanism in which the internal energy of a substance is converted into radiant energy. The transport of heat by convection together with conduction is known as *"convective heat transfer"*. Forced, free, and mixed convections are the three types of convective heat transfer. Forced convection is caused by an external agent unrelated to heating effects that causes fluid to flow over the heated body. Natural forces such as buoyancy forces, which originate from density variations in a fluid, cause free or natural convection. The temperature gradients within the fluid cause these density variances. In Mixed Convection the order magnitude of the buoyancy force is comparable with the externally maintained pressure drop to force the flow.

Dufour and Soret Effects

In simultaneous heat and mass transfer mechanisms, density differences brought on by temperature or concentration gradients, as well as material composition, all act simultaneously to drive the flow. The term "Dufour effect", often referred to as the "diffusion-thermo effect" refers to the heat flux produced by the concentration gradient. The term "thermal diffusion", which is also known as "thermo-diffusion" or "the Soret effect" [86] refers to the process by which species interactions emerge in an initially homogenous fluid subjected to a temperature gradient. These effects are classified as 2^{nd} order influences and have the potential to be significant in fields such as geosciences, hydrology, and petrology. Many instances of the Dufour effect were explored by Eckert and Drake [18]. The Soret effect had been used to discriminate between isotopes and mixtures of gases with medium (N_2, air) and very light (H_2, He) molecular weights.

Bioconvection

Microorganisms, such as microalgae and bacteria, have a higher density than water and so move upwards against gravity. A density distribution that is unstable is produced when microbe accumulation makes the top layer of suspension denser than the bottom layer. Convective instability occurs as a result, which may result in convection patterns. The spontaneous and unpredictable movement patterns of microorganisms in suspension are referred to as "bioconvection". The term bioconvection pertains to a macroscopic convection motion of fkuid-induced by a density gradient generated by motile microorganisms swimming together. These selfpropelled motile microorganisms cause bioconvection by increasing the density of the base fluid by swimming in a specific direction. Chemical processes have a vital role in bioconvection in the occurrence of motile bacteria due to their importance in food processing, material synthesis, polymer creation, bioreactors, fuel cells, and biodiesel fuels.

Viscous dissipation and Chemical Reaction

The viscous dissipation is defined as mechanical energy which is irreversibly converted to thermal energy due to viscous effects in the fluid. It is critical in viscous fluids such as polymers and oils. It has numerous uses in industry and technology. Viscous dissipation is commonly used in electrical equipment like light bulbs, electric heaters, electric stoves, and electric fuses.

Chemical reaction is the reaction in which the rate of reaction is directly proportional to the species concentration. Depending on the occurrence at an interface or as a single-phase volume reaction, the chemical reaction can be termed as either heterogeneous or homogeneous. In many fields of engineering, industry, and research, the influence of chemical processes plays a critical role in the investigation of heat and mass transfer.

Entropy generation

Entropy and entropy generation are fundamental quantities. They play essential role in understanding of many diverse phenomena ranging from cosmology to biology. A physical quantity termed entropy defined in the second law of thermodynamics is a measure of irreversibility of systems. Entropy generation is not a property because it depends upon the process path. To comprehend the function of entropy generation mechanism, it makes practicality to concentrate on the irreversibility of fluid flow and heat transfer procedures. To optimize the performance of engineering systems containing devices in which simultaneous heat and mass exchange occur, their irreversibilities of individual devices must be minimized. This approach was suggested by Bejan[11, 12]. Since the total irreversibility of a system is the sum of the component irreversibilities, this procedure improves the system performance. The factors that cause irreversibilities include friction, inelastic deformation of solids, unrestrained expansion, heat transfer across a finite temperature difference, electric resistance, mixing of two fluids, and chemical reactions. The second law of thermodynamics can be combined with the principles of fluid mechanics and heat transfer to acquire knowledge about irreversibilities that influence the working efficiency of the system and processes.

Radiation

Thermal radiation is the transfer of heat caused by the emission of electromagnetic waves. The importance of radiation becomes intensified at high absolute temperature levels. It is well known that the thermal radiation heat transfer does not require any intermediate medium by electromagnetic waves, or photons, which may travel a long distance without interacting with medium. Thus thermal radiation is of great importance in vacuum and space applications. The transfer of energy by radiation depends on differences of the individual absolute temperature of the bodies.

Using the Rosseland approximation [87], the radiation heat flux q_r is given by

$$q_r = -\frac{4\sigma^*}{3k^*}\frac{\partial T^4}{\partial y} \tag{1.5}$$

where σ^* denotes Stefan-Boltzman constant and k^* denotes the mean absorption coefficient. This approximation is good only for intensive absorption and is valid at points optically far from the bounding surface,i.e., for an optically thick boundary layer. We assume the variation in the temperature of the fluid to be appropriately minimum such that $\widetilde{T}^4$ may be shown as a linearly continuous function of the temperatures and enlarged in a Taylor Series around T_m and removing highest order terms, we get $T^4 = 4T_m^3\,T - 3T_m^4$.

Magnetohydrodynamics

The branch of continuum mechanics known as "Magnetohydrodynamics (MHD)" examines how the magnetic field and an electrically conducting fluid interact with one another. A magnetic field interacts with a fluid through body force and body coupl peer unit mass when the fluid is electrically conductive and incompressible. In the absence of gravitational effects, the regular magneto-fluid dynamics assumption is $\rho\vec{f} = \rho_e\vec{E} + \vec{J}\times\vec{B}$, where ρ_e, $\vec{E}$ $\vec{B}$ are the free charge density, the electric field and the total magnetic field, respectively. $\vec{J}$ is the current density and given by the Ohm's law $\vec{J} = \sigma\Big[\vec{E} + \vec{q}\times\vec{B}\Big]$. Since $\vec{J}\times\vec{B} \gg \rho_e E$, the later can be neglected. Hence, by adding the electromagnetic force term to the momentum

equation of the fluid, the fluid dynamical aspects of MHD can be studied.

The motion of a conducting liquid in an applied magnetic field causes an induced magnetic field, which is added to the applied magnetic field to produce the total magnetic field in the medium. The magnetic Reynolds number describes the relative strength of the induced magnetic field. When the magnetic Reynolds number is modest, it is reasonable to ignore the induced magnetic field. The motion of a conducting fluid through a magnetic field induces electric currents and the fluid experiences a force. This force is called Lorenz force $(\vec{J} \times \vec{B})$ and it alters the motion of the fluid.

1.6 Literature Review

The convective heat and mass transfer caused by a contiguously stretching surface is of considerable practical and theoretical importance because of their broader applications in polymer technology and metallurgy. Applications include the wire and fiber coating, extrusion process, foodstuff processing, polymer processing, crystal growing, production of glass fiber, drying/cooling of paper and/or textiles, continuous casting, hot rolling, fiber spinning, equipment for chemical processing and the design of different types of heat exchangers and so on. Stretching will give the extrudate a single direction orientation, therefore the heat transfer rate and collection may have an effect on both the quality of the final product and the cost of production. As a result, analyzing momentum, energy, and solute transfers within a fluid on a continuously stretching surface is critical for acquiring a basic knowledge of such processes. Further, the flow past a linear / exponential / radial stretching sheets, on the other hand, is of considerable significance and presents many challenges to researchers, engineers, and mathematicians. The first researcher to examine boundary layer behaviour on a constantly moving solid surface, or the Blasius type of flow, was Sakiadis[77, 78]. The concept of boundary layer flow was then extended for the first time by Crane [16], by taking stretching surfaces into account. For the viscous fluid across a planar stretched sheet, he developed an analytical solution. Later, several investigations have been reported on the boundary layer flows past planer stretching sheet by considering different types of fluids sub-

ject to diverse physical conditions. For the flow and stability of the Casson fluid across an extended sheet, Hamid *et al.* [24] obtained two solutions Awais *et al.* [8] examined the energy and solute transport characteristics in a Casson fluid-saturated porous media over a shrinking sheet in the existence of a heat sink/source and a transverse magnetic field. Sohail *et al.* [85] discussed the entropy generation in a Casson fluid flow across a nonlinear bi-directional stretching surface exhibiting variable heat conductance and thermal conductivity.

The research on flow across a radially stretching sheet is of great significance in view of its applications in metallurgy, chemical engineering, and biomedical engineering. Wang [94] was the first to consider the natural convection on a vertical radially stretching surface. Ariel [7] investigated the axisymmetric flow over a radially stretching sheet with slip effects and obtained exact and numerical solutions. Since then, numerous investigators have examined the flow, energy and solutal transfer characteristics over a radially stretched sheet. Khan *et al.* [35] examined the flow and heat transfer of cross fluid on a radially stretching sheet. Sreelakshmi *et al.* [88] considered the unsteady flow of a Jeffrey nanofluid over a radially stretching surface with convective thermal conditions. Shahzad *et al.* [81, 82] studied the time-dependent axially symmetric flow and heat transfer across a time-dependent radially stretched surface.

In recent years, significant advancements have been made in the investigation of magnetohydrodynamic (MHD) flow and heat transfer because of the impact of magnetic fields on the regulation of boundary layer flow and the effectiveness of numerous systems using electrically conducting fluids. The majority of the boundary layer studies that are currently in existence have been relooked by numerous researchers to incorporate magnetic field effects into consideration. The significance of an oblique magnetic force and radiation on the flow of Sisko fluid across a radially stretched sheet was examined by Ahmed *et al.* [4]. El-Aziz *et al.* [19] used the Casson fluid model to analyze the MHD stagnation point flow across a stretching surface. The consequence of Newtonian heating on the magneto Casson fluid flow on a sheet which was stretching nonlinearly was quantitatively examined by Hussanan *et al.* [32]. Gireesha *et al.* [23] explored the characteristics of MHD flow and melting heat transfer of a dusty Casson fluid over a stretching sheet. Devi *et al.* [17] examined the steady

flow of 2D non-orthogonally electrically conducting Casson fluid on a stretching sheet with orthogonal and inclined outer velocity flow.

The presence of thermal radiation on heat transfer phenomena has numerous applications in a wide range of technological operations, such as gas turbines, solar power technology, nuclear power plants, satellites, missiles, space vehicles, different aircraft propulsion systems and other industrial areas. The relevance of radiation on the stagnation-point flow of an upper convected Maxwell Casson fluid across a stretching/shrinking sheet was examined numerically by Alkasasbeh *et al.* [6] Zhou *et al.* [97] reported the impact of radiation and heat source on the unsteady stagnation point flow of a Casson fluid across a permeable stretched surface.

The study of heat and mass transfer with chemical reactions has gained significant attention due to its relevance in chemical and hydro-metallurgical manufacturing polymer production, and so on. Kumar *et al.* [39] conducted a thorough investigation on the coupled viscous and Joule dissipation impacts on MHD stagnation point flow of a Casson fluid via a permeable stretched surface with chemical reaction, multiple slips and thermal radiation. Khan *et al.* [37] analyzed the nanofluid flow across a stretching sheet with chemical reaction, multiple slips, magnetic effects, and radiation. Nayak *et al.* [58] considered the effect of chemical reaction with mass transfer on the flow across a radially stretched sheet. Vijaya *et al.* [93] studied binary chemical reaction along with activation energy of MHD Casson fluid flow induced due to stretching surface. Reza-E-Rabbi *et al.* [74] analyzed the heat and mass transfer of Casson nanofluid flow across a stretching surface along with magnetohydrodynamics, chemical reaction and thermal radiation effects. Nagaraja *et al.* [52] reported the significance of chemical reaction and a magnetic force on Casson fluid flow on a curved stretched sheet under convective heat and mass flux circumstances.

The mechanism of changing the energy obtained from the motion of the fluid by viscosity into internal energy, that is partially irreversible, is known as viscous dissipation. It is critical in viscous fluids such as polymers and oils. It has numerous uses in industry and technology. Shateyi *et al.* [84] explored the free convection in a Casson fluid towards a time dependent permeable stretched sheet featuring thermal radiation, viscous dissipation, and chemical

reaction. Afify *et al.* [3] quantitatively explored the effects of viscous dissipation along with multiple slips on the boundary layer flow of a Casson nanofluid over a stretching surface. Ibrahim *et al.* [33] reported a boundary layer study of Casson nanofluid MHD flow over a nonlinear stretching sheet with viscous dissipation and chemical reaction effects. Nawaz *et al.* [57] explored the influence of viscous dissipation, joule heating, and time-dependent thermal conductivity on a stretching sheet in a flow of Casson fluid. Reddy *et al.* [71] reported that the Eckert number has a significant effect on the heat transfer rate of Casson fluid when compared to Maxwell fluid. The contribution of viscous dissipation on naturally convective chemically reacting flow through a porous medium past an exponential stretching sheet was investigated by Reddy *et al.* [72]

The interactions between the fluxes and driving potentials get complex when heat and mass transfer occur simultaneously in a fluid motion. Cross diffusion effects (Dufour and Soret) refer to how mass flux affects temperature gradients and how energy flux affects concentration. There has been a significant amount of study that has been reported on viscous and non-Newtonian fluid flows in different configurations, with an emphasis on cross diffusion effects. Pal *et al.* [61] numerically investigated the importance of the Dufour and Soret effect on the mixed convection of nanofluids over a non-linear shrinking and stretching sheets with the thermal radiation effect. Oyelakin *et al.* [60] analyzed the impact of corss diffusion on the flow of a Casson nanofluid toward an unstable stretched sheet while heat generation and thermal radiation are present. Venkateswarlu *et al.* [55] reported the effect of cross diffusion, viscous dissipation, chemical reaction and variable thermal conductivity on the MHD flow of a Casson fluid past a stretching sheet. Ullah *et al.* [91] investigated the unsteady flow of Casson fluid towards a nonlinearly stretching sheet with convective thermal conditions and slip under the influence of heat generation/absorption, Soret, Dufour, and viscous dissipation. Narayan *et al.* [54] studied the combined effects of Soret and Dufour on magnetohydrodynamics boundary layer flow of a Jeffrey fluid past a stretching surface with chemical reaction and heat source. Raza *et al.* [70] scrutinized the simultaneous impact of radiation and velocity slip across a convectively heated elongated sheet. Saravana *et al.* [80] inspected the effects of an aligned magnetic field, diffusion-thermo and thermal-diffusion

on Casson fluid flow over a stretching sheet with varying thicknesses. Faraz *et al.* [22, 21] studied the unsteady flow of a Casson over a radially stretching surface with Soret, chemical reaction, multiple slips, and magnetic effects. Mouli *et al.* [50] considered the influence of cross diffusion on the steady, viscous dissipative Casson fluid flow along a linear stretching sheet. Venkata Ramudu *et al.* [66] addressed the impact of diffusion-thermo and thermal-diffusion on the magneto Casson liquid motion towards a convective sheet.

Bioconvection is a phenomenon that occurs when convection instability is induced by upswimming microorganisms that are heavier than their suspending medium (5 - 10% denser). Due to upswimming, the microorganisms involved, such as gyrotactic microorganisms like algae, tend to concentrate in the upper portion of the fluid layer thus causing a top-heavy density stratification that often becomes unstable. It appears in dense cultures of free-swimming micro-organisms in appropriate aqueous environments, such as oceans and rivers, puddles, and droplets. Its characteristic feature is the spontaneous self-organization or self-concentration of swimmers into a macroscopic pattern. Pal *et al.* [62] analyzed the impact of thermal radiation on the heat transport of a water-based nanofluid containing motile gyrotactic microrganisms over an exponentially stretching sheet. Pedley [63] coined the term bioconvection to describe tiny convection caused by motile microorganisms. Pal [62] explored the role of radiation and motile gyrotactic microbes on a water-based nanofluid on an exponentially elongating sheet. Ray [69] numerically considered the consequences of viscous dissipation and magnetic field on the bioconvection flow of a Casson thin film with uniform thickness over a flat elastic surface evolving from a slit. Sabir [75] explored the effects of gyrotactic microorganisms and chemical reactions on the Casson nanofluid over a permeable stretching sheet. Magagula [46] studied the Casson nanofluid bioconvection flow across a nonlinearly expanding double dispersed sheet. Sankad [79] considered bioconvection flow of a Casson fluid embracing gyrotactic microorganisms above a surface stretching linearly with magnetic field. Kumaraswamy [53] focused on the consequence of thermal heat flux and motile gyrotactic microorganisms on the flow of a Casson nanoliquid across an elongated plate.

Among the various machine learning methodologies, artificial neural network (ANN)

methodologies have been developed as viable tools for solving differential equations arising from engineering issues in recent years. Because of their operational flexibility, excellent modeling competences, and access to a broad range of training processes, feed forward neural networks are significant tools among them [41]. The ability of feed forward neural networks to analyze differential equations, whether ordinary or partial, is based on their parameterization abilities [40]. The multi-layer perceptron (MLP) has become the most prevalent form of feed forward network [64]. Yadav [96] gave an in-depth summary of neural networks in a book, in addition to a detailed discussion of neural network - based methods for resolving differential equations. A book by Chakravarty and Susmita [14] described newly established innovative ANN models for handling a variety forms of differential equations. Meade [49] utilized FFNN to deal with non-linear differential equations. Lagaris [40] employed ANN to find the solution of ordinary and partial differential equations by using two factors in the trail solution, one associated with the initial/boundary condition and the other with the neural network parameters. In most of the studies on the boundary layer flows the authors used ANN to train the numerical values obtained by using computational methods and to calculate the skin friction factor, Nusselt number, and the Sherwood. Behrang [10] used a hybrid neural network and particle swarm optimization to solve a nonlinear differential equation deriving from the similarity solution of an inverted cone immersed in a porous medium subject to wall temperature boundary conditions. Shahri [76] solved equations governing the flow and heat transfer from a porous plate in a power-law fluid in the existence of a magnetic field using the Keller - Box method. An ANN framework was developed and trained using these numeric data using the MATLAB neural network toolkit to acquire the values of skin friction and Nusselt number. Ziaei-Rad [98] employed a double precision Euler's procedure to solve the governing equation for flow over a horizontal permeable stretching flat plate in the presence of a magnetic field. An effective multilayer ANN was applied to calculate the skin friction factor and Nusselt number. Reddy [73] employed the shooting technique to solve the non-linear equations governing the flow over a permeable stretching cylinder with magnetic, chemical reaction, and slip effects. The ANN was trained using the numerical values obtained for all of the parameters, and then the backpropagation was used to forecast the skin friction coefficient, Nusselt number, and Sherwood. Elayarani [20] applied the shooting technique in

conjunction with Runge-Kutta fourth-order method to solve the governing boundary layer equations of stagnation point flow past a permeable stretching sheet with heat generation and magnetic effects. The skin friction coefficient and Nusselt number are then predicted using ANN. Mutuk [51] considered the solution of the Blasius equation using feed forward neural networks and presented a complete comparison with earlier investigations. Rashidi *et al.* [68] stated that intelligent methods, such as ANNs, are preferred in terms of accuracy compared with the correlation for modeling the properties of hybrid nanofluids. Rashidi *et al.* [67] modeled thermal conductivity of EG-Water-based nanofluids with alumina particles by utilizing Multi-Layer Perceptron (MLP) and Group Method of Data Handling (GMDH) as two efficient intelligent approaches. Nazari *et al.* [59] provided applications of data-driven methods in solar desalination system modeling.

1.7 Aim and Scope

The aim of the present thesis is to utilize artificial neural networks to study the flow, heat and mass transfer due to laminar and incompressible Casson fluid flow over a steady and unsteady radially stretching surface. The influence of magnetic field, radiation, viscous dissipation, chemical reaction, Soret number, Dufour number and bioconvection on the flow characteristics such as coefficient of skin friction, the rates of heat and mass transfer rate are analyzed numerically.

The novelty of this work is to use of neural networks for solving the governing differential equations. Instead of constructing the trial solution separately such that it satisfies the boundary conditions of the given problem, here we have taken the neural network output consisting of weights and bias terms as parameters as the trial solution itself for the simultaneous nonlinear differential equations. The mean square error is then calculated and the parameters are updated to minimize the error term using the ADAMS optimization technique.

1.8 Overview of the Thesis

This thesis consists of FOUR parts and TEN chapters

Part - I consists of single chapter i.e. Chapter - 1. This chapter serves as an introduction and motivation for the research conducted throughout the thesis. A review of relevant literature is provided, emphasising the significance of the problems presented in the thesis. The rheological equation for an incompressible and isotropic flow of a Casson fluid are presented in this chapter.

Part-II deals with deals with the Casson fluid flow past an unsteady radially stretching surface. This consists of four Chapters i.e. chapter 2 to chapter 5 . In each of these chapters, suitable transformations are used to derive the set of non-linear ordinary differential equations from the equations describing the flow. Artificial neural networks are used to find the solutions of these differential equations. A multi-layer perceptron neural network with adjustable parameters is used for the trial functions (biases and weights). The trial solution's adjustable parameters are determined using the Adams (Adaptive Moment Estimation method) optimization technique.

In Chapter - 2, the incompressible and laminar Casson fluid flow over an unsteady radially stretching sheet is considered. The non-dimensional coefficient of skin friction and Nusselt number for distinct values of unsteadiness parameter, Prandtl number, suction/injection parameter and Casson fluid parameter were studied through graphs. The findings are in good accord with those that have already been published and have also been compared with shooting method.

Chapter - 3 deals with the cross diffusion effects on the unsteady Casson fluid flow over a radially stretched sheet. Artificial neural networks are utilized to compute the solution of the problem. Graphs are used to show how important parameters affect physical quantities. In order to corroborate our conclusions, a comparison based on published research is provided. An excellent comparison is discovered, supporting the findings of our research..

The bioconvection in an unsteady Casson fluid flow across a radially elongated sheet is

presented in Chapter - 4. The solution of this problem is computed utilising Artificial Neural Networks. The prevailing approach's outcomes are confirmed using the shooting method. the analysis revealed that the performance of the ANN-based method strengthens as the number of neurons in neural network's hidden layer intensifies. In addition, graphs illustrate the effect of major considerations on physical quantities.

Chapter - 5 investigates the impacts of magnetic field and chemical reaction on entropy generation throughout boundary layer flow and heat transfer due to a unsteady radially extending sheet. The impact of relevant parameters on skin friction coefficient, rates of heat and mass transfer, and entropy generation is displayed through graphs.

Part-III deals with the Casson fluid flow across a steady radially stretching surface. This consists of four chapters i.e. Chapter 6 to Chapter 9. Using similarity transformations, the governing equations of the flow were converted to ODE in all of these chapters. Artificial neural networks are used to compute the solution to these problems. A multi-layer perceptron neural network with adjustable parameters is used for the trial functions (biases and weights).

Chapter - 6 deals with Casson fluid flow past a radially stretching sheet with the impacts of magnetic field and thermal radiation. Artificial neural networks are used to compute the solution of the flow. The results of the current method are validated utilizing shooting method in conjunction with the Runge-Kutta fourth-order method.

In Chapter - 7, the flow and heat transmission of a Casson fluid towards a steady radially stretched sheet in the presence of chemical reaction and viscous dissipation, is presented. Similarity transformations are implemented on the flow's equations to get a system of non-linear ODEs. Then the solution is computed using ANN .

Chapter - 8 considers the bioconvection in a Casson fluid flow over a steady radially extending sheet. A multi-layer perceptron neural network is used to obtain the solution of the governing equations. The effect of unsteadiness parameter, bio convection Peclet number, suction / injection parameter, bioconvection Schmidth number, Schmidt number and bioconvection constant on the coefficient of skin friction, rates of heat and mass transfer, and motile microorganism rate is displayed through graphs.

The impacts of magnetic field and viscous dissipation on the generation of the entropy throughout boundary layer flow and heat transfer due to a steady radially extending sheet is presented in Chapter - 9. The impact of relevant parameters on skin friction coefficient, rate of heat transfer coefficient and Entropy generation is displayed through graphs.

Part - IV consists of single chapter i.e. Chapter - 10. The key conclusions of the previous chapters are summarised in this chapter, along with possible future research directions.

A bibliography is provided at the end of the thesis and is organised alphabetically.

A considerable part of the work in the thesis is published/accepted for publication in reputed International Journals. The remaining part is communicated for publications. The details are presented below.

List of papers Published

1. "Artificial neural network modeling of the Casson fluid flow over unsteady radially stretching sheet with Soret and Dufour effects.", *Journal of Thermal Analysis and Calorimetry*,147, pages 14891-14903(2022).

List of papers Accepted

2. "An artificial neural network solution for the casson fluid flow past a radially stretching sheet with magnetic and radiation effect.", *Mathematical Models and Computer Simulation.*

List of papers communicated

3. "Study of Casson fluid flow over a time-dependent radially stretching sheet using artificial neural networks", Communicated to *Engineering Transactions.*

4. "Computational analysis for bioconvection flow of a Casson fluid past an unsteady radially stretching sheet using artificial neural networks", Communicated to *Heat Transfer*

Research.

5. "Artificial neural network approach to study the Casson fluid flow past a radially stretching sheet with viscous dissipation and chemical reaction effect", Communicated to *Archives of Computational methods in Engineering.*

6. "Neural network analysis for bioconvection flow of casson fluid over a vertically extending sheet", Communicated to *International journal of Applied and Computational Mathematics.*

7. "Simultaneous effects of chemical reaction and magnetic field on entropy generation in a Casson fluid flow over a radially stretching sheet: A Neural Network based analysis", Communicated to *Mathematical Methods in the Applied Sciences.*

8. "A neural network based analysis for entropy generation of Casson fluid flow over radially expanding sheet with magentic effect and viscous dissipation", Communicated to *Engineering Applications of Computational Fluid Mechanics.*

Chapter 2

Study Of Casson Fluid Flow Over A Time-Dependent Radially Stretching Sheet Using Artificial Neural Networks [1]

2.1 Introduction

2.2 Introduction

The analysis of flow over a radially stretching sheet is important because of its applications in paper production, polymer extrusion, liquid metal, and glass fiber, among others. Several researchers have analyzed the heat and mass transfer features of the flow of Newtonian and non-Newtonian fluids. Khan *et al.* [35] anlayzed the cross fluid flow across a radially stretching sheet. Ahmed *et al.* [4] studied the consequence of inclined magnetic field and radiation on the flow of Sisko fluid over a radially stretching sheet. Sreelakshmi *et al.* [88]

[1] Communicated to "**Engineering Transactions**"

considered the unsteady flow of a Jeffrey nanofluid on a radially stretching surface with convective boundary conditions. Khan *et al.* [37] analyzed the axisymmetric flow of the nanofluid past a stretching sheet with multiple slips, magnetic effects, chemical reaction, and radiation. Nayak *et al.* [58] considered the effect of chemical reaction with mass transfer flow through a radially stretched sheet. Most of the investigations on the radially stretching sheet are restricted to steady-state. However, when flow depends on time, unsteadiness becomes an important component of study in a variety of engineering procedures. Shahzad *et al.* [81, 82] analyzed the unsteady axially symmetric flow and heat transfer across a time-dependent radially stretched surface.

In this chapter, we investigate the flow and energy transfer of a Casson fluid on a time-dependent radially stretched sheet. The equations of the flow are transfigured into a set of non-linear ODEs by employing suitable transformations. Artificial neural networks are used to compute the solution to these nonlinear differential equations. Comparisons are made between the findings of the current method and those obtained using the Runge-Kutta method of fourth order. The findings demonstrate that the ANN-based method provides significant accuracy. As the neural network's number of neurons increases, the solution becomes more effective. Graphs are also used to show the effect of relevant parameters on physical quantities.

2.3 Mathematical Formulation

Consider the flow of Casson fluid over unsteady radially stretching sheet as shown in figure 2.1. In formulating the problem following assumptions are made and are considered throughout the thesis

- The flow is unsteady, incompressible and two-dimensional.
- Cylindrical polar coordinate system (r, θ, z) is chosen by taking r-direction along the stretching sheet and z-direction is vertical to it with origin fixed.

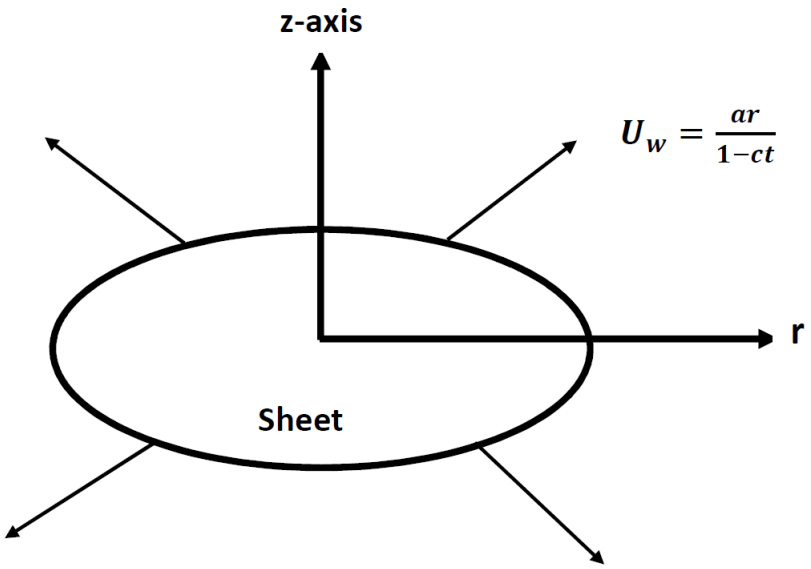

Figure 2.1: "Geometry and coordinate system of the problem."

- The stretching velocity $U_w(r,t) = \dfrac{ar}{1-ct}$.
- Surface temperature of the sheet is $T_w(r,t) = T_\infty + \dfrac{br}{1-ct}$, where T_∞ is the ambient temperature of the medium with $T_w > T_\infty$, where a, b and c are positive constants with dimension per time with $ct < 1$.
- All physiological quantities do not depend on θ because of rotational symmetry of the flow.

With the above assertions, the equations describing the flow are given by [81, 22]

$$\frac{\partial u}{\partial r} + \frac{u}{r} + \frac{\partial w}{\partial z} = 0 \tag{2.1}$$

$$\frac{\partial u}{\partial t} + u\frac{\partial u}{\partial r} + w\frac{\partial u}{\partial z} = \nu\left(1 + \frac{1}{\beta}\right)\frac{\partial^2 u}{\partial z^2} \tag{2.2}$$

$$\frac{\partial T}{\partial t} + u\frac{\partial T}{\partial r} + w\frac{\partial T}{\partial z} = \alpha\frac{\partial^2 T}{\partial z^2} \tag{2.3}$$

where $u(r,z,t)$ represents the velocity components in r direction, $w(r,z,t)$ represents the velocity components in z direction, $T(r,z,t)$ represents the temperature, ν represents the kinematic viscosity, $\beta = \dfrac{\mu_\beta\sqrt{2\pi_c}}{\tau_y}$ represents the Casson fluid parameter and α represents the

thermal diffusivity.

The associated boundary conditions are

$$\left.\begin{array}{ll} \text{At} \quad z=0: & u=U_w(r,t)=\dfrac{ar}{1-ct}; \quad w=W_0 \quad T=T_w(r,t)=T_\infty+\dfrac{br}{1-ct} \\ \text{As} \quad z\to\infty: & u\to 0; \quad T\to T_\infty. \end{array}\right\} \tag{2.4}$$

where $W_0=-2S\left(\dfrac{\nu U_w}{r}\right)^{1/2}$. Here, $W_0<0$ $(S>0)$ indicates suction and $W_0>0$ $(S<0)$ indicates injection.

In order to get dimensionless form of Eqs. (2.1) – (2.3), introduce the stream function $u=-\dfrac{1}{r}\dfrac{\partial\psi}{\partial z}$ and $w=\dfrac{1}{r}\dfrac{\partial\psi}{\partial r}$ and the following similarity transformations [81]

$$\psi(r,z)=-r^2U_wRe^{-1/2}f(\eta), \quad \eta=\frac{z}{r}Re^{1/2} \quad and \quad \theta=\frac{T-T_\infty}{T_w-T_\infty} \tag{2.5}$$

where $Re=\dfrac{rU_w}{\nu}$ represents the local Reynolds number.

Putting Eq, (2.5) in Eqs. (2.1)-(2.3), we obtain

$$(1+\frac{1}{\beta})f'''+2ff''-f'^2-A(f'+\frac{1}{2}\eta f'')=0 \tag{2.6}$$

$$\frac{1}{\mathrm{Pr}}\theta''+2f\theta'-f'\theta+A(\theta+\frac{1}{2}\eta\theta')=0 \tag{2.7}$$

The dimensionless form of conditions (2.4) are:

$$f(0)=S, \quad f'(0)=1, \quad \theta(0)=1 \quad ; f'(\infty)\to 0, \quad \theta(\infty)\to 0 \tag{2.8}$$

where $A=\dfrac{a}{c}$ represents the unsteadiness parameter and $\mathrm{Pr}=\dfrac{\mu c_p}{k}$ denotes the Prandtl number.

The parameters of the engineering interest are the coefficient of skin friction and heat

transfer rate (Nusselt number), which are defined as

$$C_f = \frac{2\mu}{\rho U^2}\left(\frac{\partial u}{\partial z}\right)\Big|_{z=0} \quad \text{and} \quad N_u = \frac{r}{k(T_w - T_\infty)}\left(\frac{\partial T}{\partial z}\right)\Big|_{z=0} \tag{2.9}$$

In non-dimensional form these quantities are given by

$$\frac{1}{2}{R_e}^{1/2} C_f = f''(0) \quad and \quad {R_e}^{-1/2} N_u = -\theta'(0) \tag{2.10}$$

2.4 Method of Solution

Consider a multilayered perceptron consisting of 3 – layers namely Input layer - consisting of 'n' inputs $\bar{\eta}$=$(\eta_1, \eta_2, ...\eta_n)$, hidden layer - consisting of 'k' neurons and output layer consisting of two neurons to estimate the solutions to two coupled ordinary differential equations as shown in the Fig. 2.2.

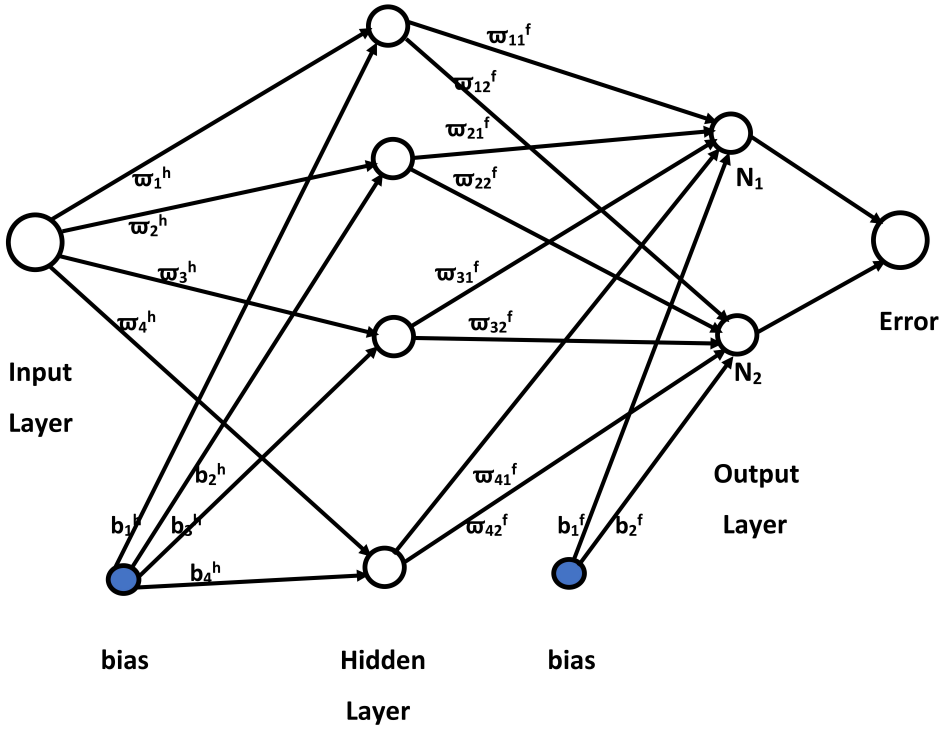

Figure 2.2: "Feed Forward Neural Network."

The output of the network, $N_m(\bar{\eta}, \{w, \bar{b}\})$ can be written as

$$N_m(\bar{\eta}, \{w, \bar{b}\}) = \Sigma_{k,n} w^f_{mk} \sigma\{w^h_k \eta_n + b^h_k\} + b^f_m \tag{2.11}$$

where σ is the activation function which is applied on each unit element by element, superscript h is for hidden layer and f is for final layer. To determine the solutions of system of m differential equations, a single neural network with m outputs can be used.

Since we have two coupled differential equations we have considered two outputs $N_1(\eta_i, P_1)$ and $N_2(\eta_i, P_2)$. These Network outputs $N_1(\eta_i, P_1)$ and $N_2(\eta_i, P_2)$ denote the trial solution for f and θ respectively with the adjustable parameters P_1 and P_2 respectively, which are given by the expressions

$$\left.\begin{aligned} N_1(\eta_i, P_1) &= \sum_{j=1}^{k} \varpi^f_{1j} \sigma\{\varpi^h_j \eta_i + b^h_j\} + b^f_1 \\ N_2(\eta_i, P_2) &= \sum_{j=1}^{k} \varpi^f_{2j} \sigma\{\varpi^h_j \eta_i + b^h_j\} + b^f_2 \end{aligned}\right\} \tag{2.12}$$

where, ϖ^h_j represents the weights from the input layer to the j^{th} hidden neuron, b^h_j is the bias term in the hidden layer, ϖ^f_{1j} is the weight from the j^{th} hidden neuron to the first output neuron, b^f_1 is the bias term and ϖ^f_{2j} is the weight from the j^{th} hidden neuron to the second output neuron, b^f_2 is the bias term. P_1 corresponds to the parameters ϖ^h_j, b^h_j, ϖ^f_{1j}, b^f_1 and P_2 corresponds to the parameters ϖ^h_j, b^h_j, ϖ^f_{2j} and b^f_2 respectively.

Since no data has been collected to learn from the differential equation, we have to insert Eq. (2.12) in the differential equations Eq.(2.6) and Eq. (2.7). Hence, we get

$$\begin{aligned} E_f = &\left(1 + \frac{1}{\beta}\right) {N_1}'''(\eta_i, P_1) + 2N_1(\eta_i, P_1){N_1}''(\eta_i, P_1) - {N_1}^2(\eta_i, P_1) - A({N_1}'(\eta_i, P_1) \\ &+ \frac{1}{2}\eta_i {N_1}''(\eta_i, P_1)) \end{aligned} \tag{2.13}$$

$$\begin{aligned} E_\theta = &\frac{1}{Pr}{N_2}''(\eta_i, P_2) + 2N_1(\eta_i, P_1)N_2(\eta_i, P_2) - {N_1}'(\eta_i, P_1)N_2(\eta_i, P_2) - A(N_2(\eta_i, P_2) \\ &+ \frac{1}{2}\eta_i {N_2}'(\eta_i, P_2)) \end{aligned} \tag{2.14}$$

where E_f and E_θ represents the errors or residuals with respect to the equations Eq. (2.6) and Eq. (2.7) respectively. If the trial/constructed solutions for f and θ given in Eq. (2.12) are close to exact solution then the errors E_f and E_θ tend to zero.

Similarly, the errors in the boundary conditions are given by:

$$N_1(\eta_1, P_1) = S; \quad N_1'(\eta_1, P_1) = 1; \quad N_2(\eta_1, P_2) = 1; \quad N_1'(\eta_n, P_1) = 0; \quad N_2(\eta_n, P_2) = 0. \tag{2.15}$$

The mean square of error (MSE) is calculated by taking $1/n$ times the sum of the squared errors of differential equations (Eqs. (2.13) - (2.14)) along with the error in the boundary conditions Eqs. (2.15) on the training set and then minimized. The solution produced by determining a set of biases and weights that minimizes the MSE (or loss function) after training is the final solution of the problem. Hence, the MSE or loss function $\mathfrak{E}(P_1, P_2)$ is given by

$$\begin{aligned} \mathfrak{E}(P_1, P_2) = \frac{1}{n} \sum_{i=1}^{n} & (E_f)^2 + (E_\theta)^2 + [N_1(\eta_1, P_1) - S]^2 \\ & + [N_1'(\eta_1, P_1) - 1]^2 + [N_1'(\eta_n, P_1)]^2 + [N_2(\eta_1, P_2) - 1]^2 + [N_2(\eta_n, P_2)]^2 \end{aligned} \tag{2.16}$$

where 3^{rd} – 7^{th} terms represent error terms corresponding to the boundary conditions.

The problem is to minimize $\mathfrak{E}(P_1, P_2)$ by optimizing the biases and weights in the network for a given network configuration. The derivatives of the network output with respect to its input must be computed in order to compute the error $\mathfrak{E}(P_1, P_2)$. The derivative of networks output $N_1(\eta_i, P_1)$ and $N_2(\eta_i, P_2)$ with respect to input vector η_i are calculated using Python package called autograd. Backpropagation can then be used to pursue the optimization by evaluating the derivatives of the loss function with respect to the network parameters. Here in this paper, we used a single hidden layer, Sigmoid activation function, the Adam optimizer [38] with an initial learning rate of 0.01.

To apply this method the semi-infinite domain of the given problem i.e. $[0, \infty]$ is reduced to $[\eta_1, \eta_\infty]$ where $\eta_1 = 0$, η_∞ is the parameter used to recover the boundary conditions at

infinity. We start with training points that are chosen from the domain of the given problem i.e. $[0, \eta_\infty = 10]$ and the weights and bias terms, which are generated randomly and we train the model to modify the parameters in the given domain of the problem.To ensure that the boundary conditions in the loss are integrated into each network parameter update, we use the entire set of training points. In general, we find that a single hidden layer with a small number of units is enough to get very exact results.

To check the convergence of the solution of the method, the dimensionless coefficient of skin friction ($f''(0)$) and rate of heat transfer ($\theta'(0)$) at the surface for A=0.5, S=-1.0,Pr=1.0 are calculated by choosing different number of training points 30, 50 and 100 and different number of neurons 5, 10 and 15 in the hidden layer and. The computed results are presented in the Tables 2.1 and 2.2. It is evident from the Tables 2.1 and 2.2 that the solution has convergence of 10^{-4} when the Data points are 50 and Hidden neurons are 10.

Number Of training points	$f''(0)$	$\theta'(0)$
30	-0.62046424	-0.62045657
50	-0.62040682	-0.62044375
100	-0.62040601	-0.62041189

Table 2.1: "Convergence analysis for the values of $f''(0)$ and $\theta'(0)$ for A=0.5, S=-1.0,Pr=1.0 by the present method with different number of Data points and number of Neurons as 10".

Number Of Neurons	$f''(0)$	$\theta'(0)$
5	-0.62058754	-0.62049965
10	-0.62040682	-0.62044375
15	-0.62040513	-0.62044375

Table 2.2: "Convergence analysis for the values of $f''(0)$ and $\theta'(0)$ for A=0.5, S=-1.0,Pr=1.0 by the present method with different number of Hidden neurons and number of Data points fixed as 50".

2.5 Computational Results and Discussion

In the present study, the coefficient of skin friction C_f and Nusselt Number N_u are computed for different values of Casson fluid parameter β, the unsteadiness parameter A, Prandtl number Pr and suction/injection parameter S and depicted graphically.

The method's correctness is validated by comparing the current numerical values of the coefficient of skin friction and the Nusselt number with the reported data of Shahzad *et al.* [81] for distinct values of unsteadiness parameter A, suction/injection parameter S, Prandtl number Pr and for large values of Casson fluid parameter β. The computed results are presented in Table 2.3. It is apparent from Table 2.3 that the existing values are in accordance with the findings of Shahzad *et al.* [81].

A	S	Pr	$f''(0)$		$\theta'(0)$	
			Present Value	Shahzad *et al.* [81]	Present Value	Shahzad *et al.* [81]
0.5	-1	1	-0.620406	-0.620400	-0.620443	-0.620400
0.5	-0.5	1	-0.887208	-0.887200	-0.887623	-0.887200
0.5	0	1	-1.308334	-1.308999	-1.308925	-1.308999
0.5	0.5	1	-1.906700	-1.907999	-1.908495	-1.907999
0.5	1	1	-2.653536	-2.655999	-2.656215	-2.655999
0	0.5	1	-1.798938	-1.798999	-1.799092	-1.798999
1	0.5	1	-2.015453	-2.016999	-2.017439	-2.016999
0.5	0.5	0.5	-1.906859	-1.907999	-1.121147	-1.119999
0.5	0.5	0.7	-1.907159	-1.907999	-1.450060	-1.450000

Table 2.3: "Comparative analysis for the values of $f''(0)$ and $\theta'(0)$ by the present method with the results of Shahzad *et al.* . [81]".

The effectiveness of the method is also validated by relating the current numerical results of skin friction coefficient and Nusselt number are calculated using the shooting method in conjunction with the Runge-Kutta fourth order method for $A = 0.5$, $S = -1.0$ and $Pr = 1.0$. The computed results are presented in the Table 2.4. It is evident from the Table 2.4 that the present results are consistent with the results obtained by using shooting method.

A	S	Pr	$f''(0)$		$\theta'(0)$	
			Present method	Shooting method	Present method	Shooting method
0.5	-1	1	-0.62040682	-0.620400	-0.62044375	-0.620400

Table 2.4: "Comparative analysis for the values of $f''(0)$ and $\theta'(0)$ at the surface by the present method with the results of Shooting method".

Fig. 2.3 illustrates the plot of error (between ANN method and Shooting technique results) in the values of $f'(\eta)$ and $\theta(\eta)$ for 7 equispaced positions in $[0, 6]$. The present

method's (ANN method) conclusions are in perfect accord with those produced by Shooting method. as shown in Figure 2.3.

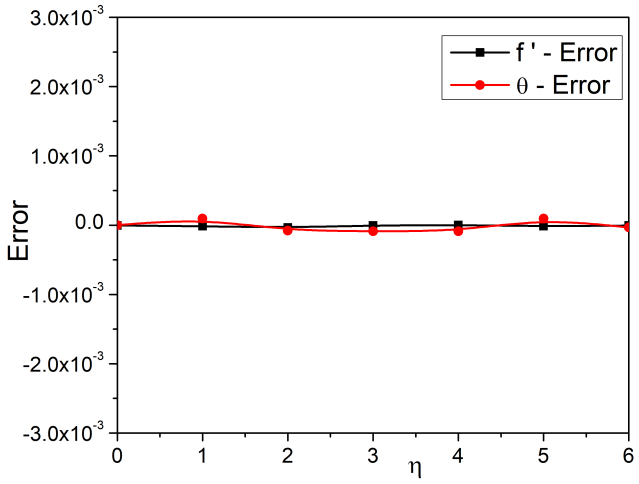

Figure 2.3: "Error plot between the results obtained by Artificial Neural Network method and Shooting method for the values of velocity and temperature profiles".

Figure 2.4 refers the significance of unsteadiness parameter A on the velocity and temperature profiles for fixed values of other parameters. It is observed from figures 2.4(a) and 2.4(b) that, both the velocity and temperature are decreasing in the beginning and enhancing afterwards for a growth in the unsteadiness parameter A.

The impact of Casson fluid parameter β on the velocity and temperature is portrayed in Figure 2.5. It is perceived from the figure 2.5(a) that, the velocity is decreasing with an enhancement in the Casson fluid parameter. A rise in the value of β causes the temperature to rise as shown in figure 2.5(b).

The impact of Prandtl number Pr on the velocity and temperature is portrayed in Figure 2.6. It is perceived from the Figure 2.6(b) that, the temperature is decreasing with an enhancement in Prandtl number.

The variation of the velocity and temperature with suction/injunction parameter S is displayed in figures 2.7(a) - 2.7(b). It has been shown that increasing the suction/injunction parameter reduces both velocity and temperature values.

Figure 2.8 provides the influence of the unsteadiness parameter A on the skin friction and Nusselt number. As the unsteadiness parameter A increases, the skin friction coefficient decreases as shown in the figure 2.8(a). According to figure 2.8(b), the rate of heat transmission increases as the unsteadiness parameter A rises.

The effect of Prandtl number Pr on the skin friction and Nusselt number is presented in Figure 2.9. Nusselt number is increasing with an increase in the Prandtl number Pr and there is no significance on skin friction, as shown in the figures 2.9(a) and 2.9(b).

The impact of suction/injection parameter S on the skin friction and Nusselt number is depicted in Figure 2.10. It is noticed from the figures 2.10(a) and 2.10(b) that, skin friction is decreasing and Nusselt number is increasing for the increasing values of suction / injection parameter S.

2.6 Conclusions

The primary objective of this research was to use the Artificial Neural Network approach to solve coupled nonlinear differential equations emerging from the flow of a Casson fluid over a radially expanding sheet with the influence of suction/injection at the surface. The Adams optimization method was used to minimize the error function and to determine the optimal values for the trial function's adjustable parameters. The numerical results achieved show extremely good precision when compared to those acquired utilizing the shooting method. Furthermore, the accuracy of the neural network improves as the number of neurons increases. The influences of A, β, Pr and S on the relevant physical quantities are investigated.

- The velocity reduces as the Casson fluid and suction/injection parameters increase.
- The temperature rises as the Casson fluid parameter rises, while it falls as the Prandtl number and suction / injection parameter rise.
- The skin friction coefficient reduces when the suction/injunction parameter and unsteadiness parameter increases.

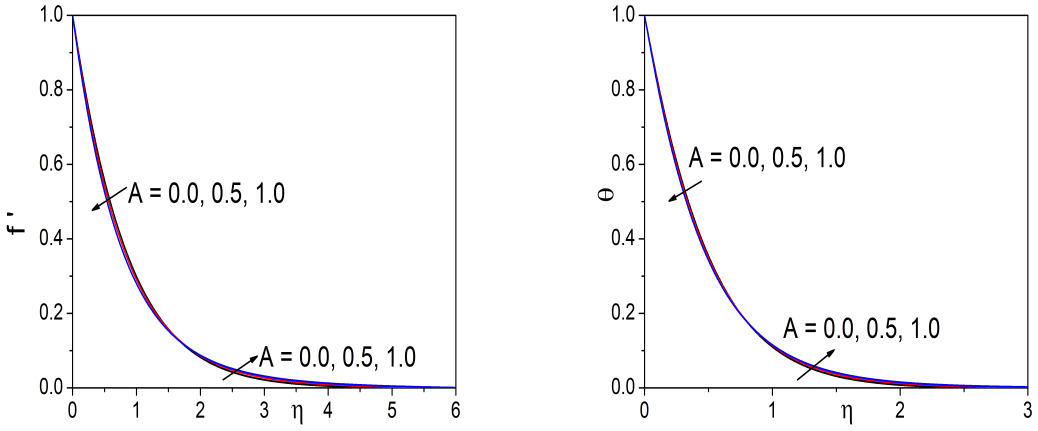

(a) (b)

Figure 2.4: "The variation of velocity and temperature profiles with unsteadiness parameter."

- The rate of heat transfer enhances as unsteadiness parameter, Prandtl number and suction / injection parameter increases.

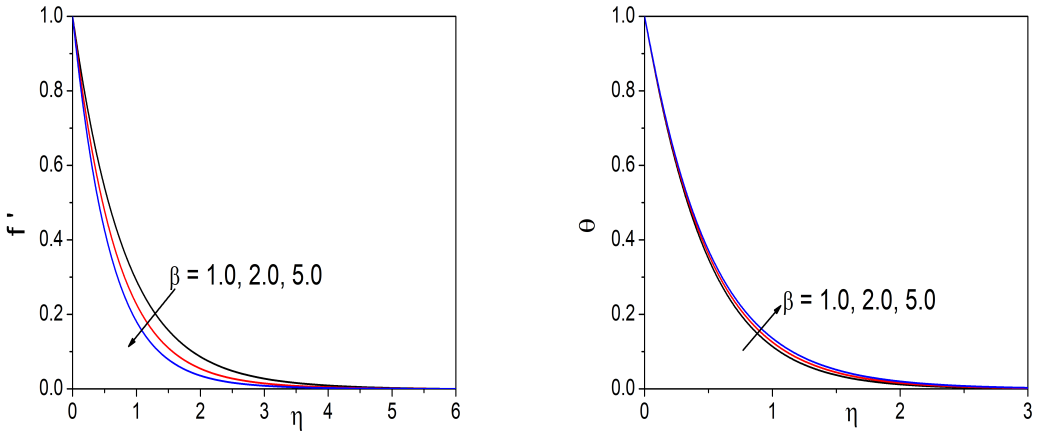

(a) (b)

Figure 2.5: "The variation of velocity and temperature profiles with Casson fluid parameter".

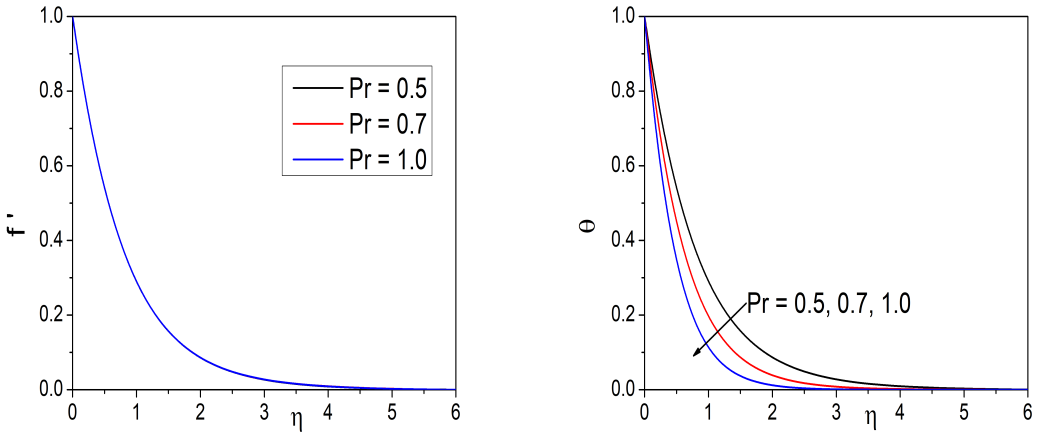

(a) (b)

Figure 2.6: "The variation of velocity and temperature profiles with Prandtl number".

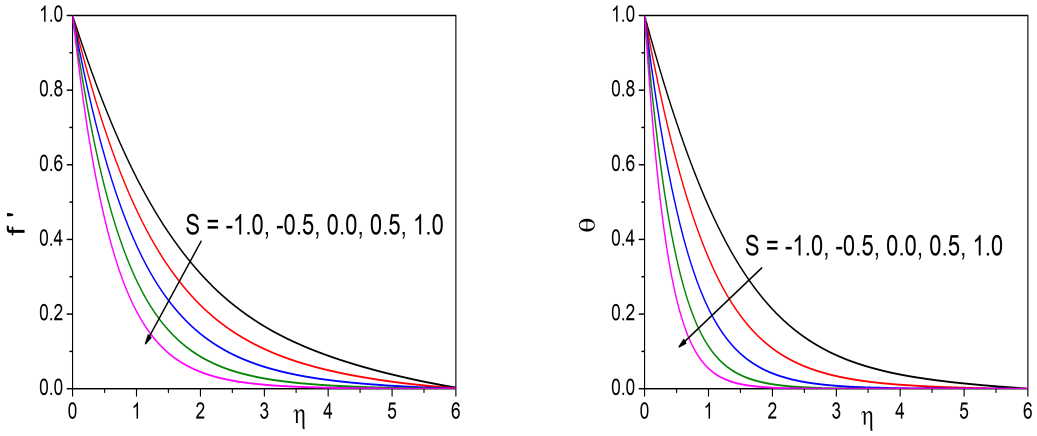

(a) (b)

Figure 2.7: "The variation of velocity and temperature profiles with suction / injection parameter".

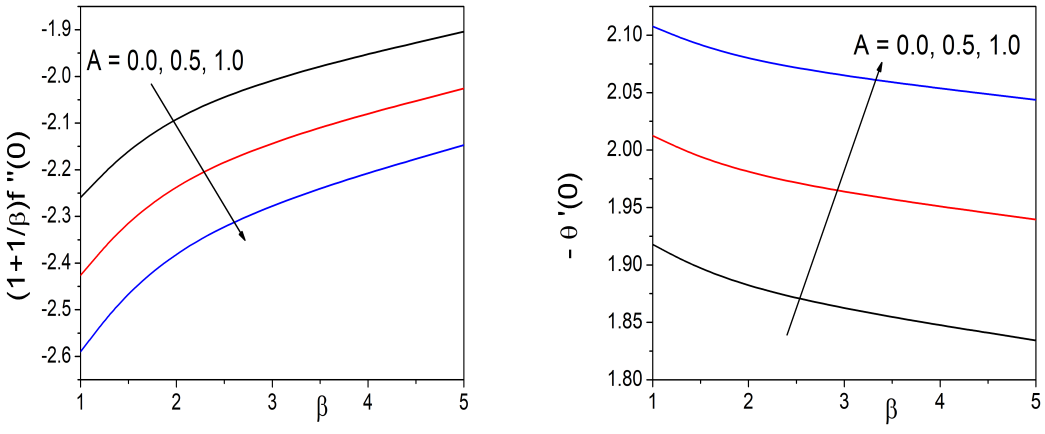

(a) (b)

Figure 2.8: "Plot of skin friction coefficient and heat transfer rate for distinct values of Casson fluid parameter".

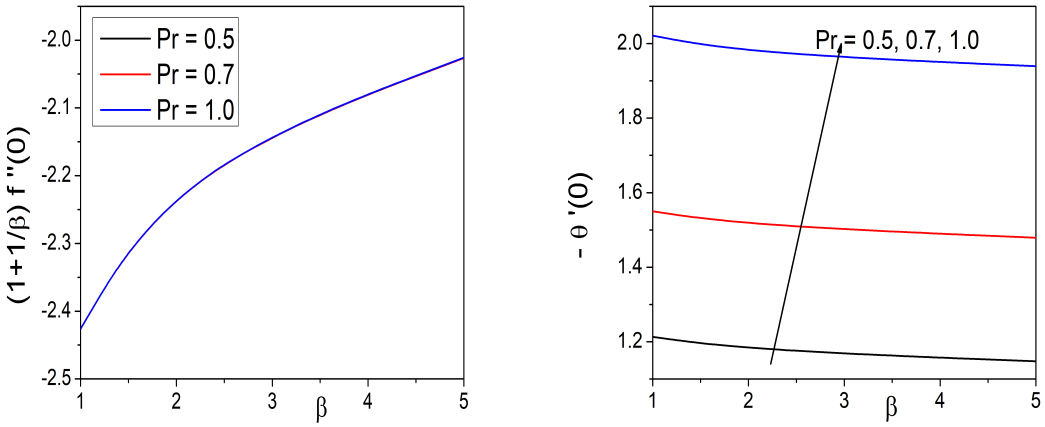

(a) (b)

Figure 2.9: "Plot of skin friction coefficient and heat transfer rate for distinct values of Prandtl number".

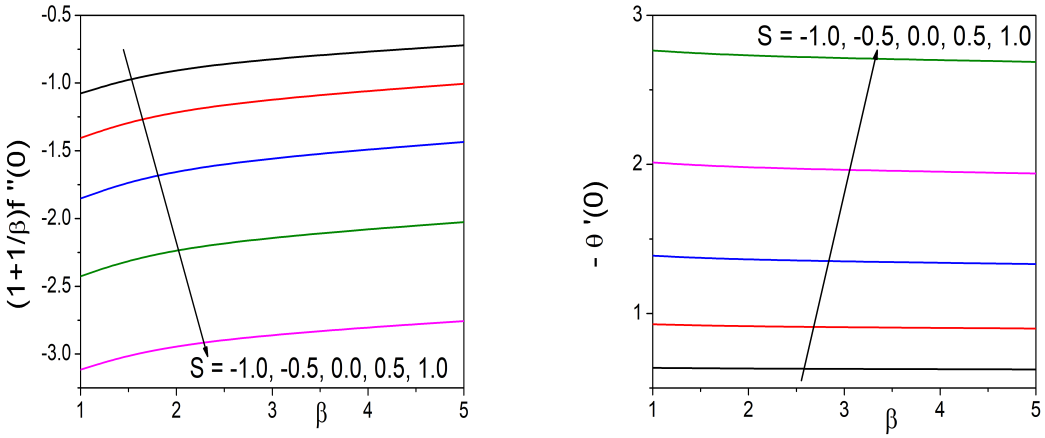

(a) (b)

Figure 2.10: "Plot of skin friction coefficient and heat transfer rate for distinct values suction / injection parameter".

Chapter 3

Artificial Neural Network Modeling of The Casson Fluid Flow Over Unsteady Radially Stretching Sheet With Soret and Dufour Effects [1]

3.1 Introduction

The relationships amongst the fluxes and the driving potentials are complex when heat and mass transfer exist at the same time in a flowing fluid. Both concentration and temperature gradients have been found to induce energy fluxes. The Dufour effect can be described as the heat flux produced by a concentration gradient. The Soret effect takes place when species interact in a fluid subjected to a temperature gradient [86]. These aspects are generally ignored in heat and mass transfer research as they have a lower order of magnitude than behaviour defined by Fourier's and Fick's laws. There has been a significant number of papers presented in the literature on the fluid flows in different cross sections, with a emphasis on the Soret and Dufour effects. Hayat *et al.* [25] considered the Soret, Dufour and magnetic

[1] Published in "**Journal of Thermal Analysis and Calorimetry"**, 22 (2021): 100830

effects on the flow of the Casson fluid across a stretched surface. In the framework of Soret and Dufour impacts, Kameswaran *et al.* [34] investigated the flow of a Casson fluid over a elongated sheet. Sharad [83] dealt the impacts of Soret and Dufour, thermal radiation and chemical reaction on MHD mixed convection flow of a Casson fluid over an exponentially elongated sheet. Oyelakin *et al.* [60] presented the Dufour and Soret effects on the Casson nanofluid flow over a stretched sheet with thermal radiation and heat generation. Venkateswarlu *et al.* [55] reported the effect of Soret and Dufour, viscous dissipation, variable thermal conductivity and chemical reaction on the MHD flow of a Casson fluid past a stretching sheet. Khan *et al.* [36] addressed MHD stagnation point flow of Casson fluid towards a stretching sheet. Raza *et al.* [70] analyzed the simultaneous impact of radiation and velocity slip across a convectively heated stretching sheet. Saravana *et al.* [80] inspected the effects of an aligned magnetic field and cross diffusion on Casson fluid flow over a stretched surface with varying thicknesses. Mouli *et al.* [50] studied the influences of Soret and Dufour on steady, viscous dissipative Casson fluid flow along a linear stretching surface.

In this chapter, the current research examines the applicability of the ANN technique for unsteady axisymmetric flow across a radially stretched sheet while taking into account the Soret and Dufour effects. The influences of pertinant parameters governing the flow and geometry on the skin friction coefficient, Nusselt number and Sherwood number are discussed in detail.

3.2 Formulation of the Problem

Consider a unsteady two dimensional and laminar flow of a Casson fluid over a stretching surface $z = 0$ as shown in Fig. 2.1. In addition to the assumptions made in Chapter 2, here we assume that the concentration at the stretching surface is $C_w = C_\infty + \dfrac{dr}{1-ct}$, where C_∞ ($C_w > C_\infty$) is the ambient concentration.

The equations describing the flow are given by [81, 22],

$$\frac{1}{r}\frac{\partial}{\partial r}(ru) + \frac{\partial w}{\partial z} = 0 \tag{3.1}$$

$$\frac{\partial u}{\partial t} + u\frac{\partial u}{\partial r} + w\frac{\partial u}{\partial z} = \nu(1 + \frac{1}{\beta})\frac{\partial^2 u}{\partial z^2} \tag{3.2}$$

$$\frac{\partial T}{\partial t} + u\frac{\partial T}{\partial r} + w\frac{\partial T}{\partial z} = \alpha\frac{\partial^2 T}{\partial z^2} + D_{TC}\frac{\partial^2 C}{\partial z^2} \tag{3.3}$$

$$\frac{\partial C}{\partial t} + u\frac{\partial C}{\partial r} + w\frac{\partial C}{\partial z} = D_S\frac{\partial^2 C}{\partial z^2} + D_{CT}\frac{\partial^2 T}{\partial z^2} \tag{3.4}$$

where $C(r, z, t)$ is the concentration, D_{TC} is Dufour type diffusivity, D_{CT} is Soret type diffusivity and the solutal diffusivity is represented by D_S

The corresponding boundary conditions are:

$$\left.\begin{aligned} &u = U_w = \frac{ar}{1-ct},\ w = W_0,\ T = T_w = T_\infty + \frac{br}{1-ct}, \\ &C = C_w = C_\infty + \frac{dr}{1-ct} \text{ at } z = 0 \\ &u \to 0, \quad T \to T_\infty, \quad C \to C_\infty \quad \text{as} \quad z \to \infty \end{aligned}\right\} \tag{3.5}$$

where $W_0 = -2S\left(\frac{\nu U_w}{r}\right)^{1/2}$ and U_w the stretching velocity. Here at the surface, $W_0 > 0$ ($S < 0$) represents injection and $W_0 < 0$ ($S > 0$) represents suction.

In order to non-dimensionalize the Eqs. (3.1)-(3.4), define the following similarity transformations

$$\psi(r, z) = -r^2 U_w Re^{-1/2} f(\eta),\ \eta = \frac{z}{r}Re^{1/2},\ \ \theta(\eta) = \frac{T - T_\infty}{T_w - T_\infty} \text{ and } \phi(\eta) = \frac{C - C_\infty}{C_w - C_\infty} \tag{3.6}$$

where, $\psi(r, z)$ denote the stream function given by $ru = -\frac{\partial \psi}{\partial z}$, $rw = \frac{\partial \psi}{\partial r}$ and $R_e = \frac{rU_w}{\nu}$ denote the local Reynolds number.

Putting Eq, (3.6) in Eqs. (3.1)-(3.4), we obtain the the following dimensionless equations:

$$(1+\frac{1}{\beta})f'''+2ff''-f'^2-A(f'+\frac{1}{2}\eta f'')=0 \tag{3.7}$$

$$\frac{1}{P_r}\theta''+D_f\phi''-f'\theta+2f\theta'-A(\theta+\frac{\eta}{2}\theta')=0 \tag{3.8}$$

$$\frac{1}{Sc}\phi''+S_r\theta''-f'\phi+2f\phi'-A(\phi+\frac{\eta}{2}\phi')=0 \tag{3.9}$$

where $S_r=\frac{D_{CT}}{\nu}\frac{T_w-T_\infty}{C_w-C_\infty}$ represent Soret number and $D_f=\frac{D_{TC}}{\nu}\frac{C_w-C_\infty}{T_w-T_\infty}$ represent the Dufour number.

The boundary conditions given in Eq. (3.5) are transformed into the following form[81]:

$$\left.\begin{aligned} &f(\eta)=S,\ f'(\eta)=\theta(\eta)=\phi(\eta)=1 \text{ at } \eta=0,\\ &f'(\eta)\to 0,\ \theta(\eta)\to 0\ \phi(\eta)\to 0 \text{ as } \eta\to\infty \end{aligned}\right\} \tag{3.10}$$

The non-dimensional form of the skin friction coefficient C_f, Nusselt number N_u, and Sherwood number Sh are given by

$$\frac{1}{2}{R_e}^{1/2}C_f=(1+\frac{1}{\beta})f''(0),\ {R_e}^{-1/2}N_u=-\theta'(0)\,\text{and}\,{R_e}^{-1/2}S_h=-\phi'(0) \tag{3.11}$$

3.3 Method of Solution

Consider a multilayered perceptron consisting of three layers namely input layer consisting of 'n' inputs $\bar{\eta}$=$(\eta_1,\eta_2,...\eta_n)$, hidden layer - consisting of 'k' neurons and output layer consisting of 'm' neurons to estimate the solutions to 'm' coupled ordinary differential equations.

The output of the network, $N_m(\bar{\eta},\{w,\bar{b}\})$ can be written as

$$N_m(\bar{\eta},\{w,\bar{b}\})=\Sigma_{k,n}w^f_{mk}\sigma\{w^h_k\eta_n+b^h_k\}+b^f_m \tag{3.12}$$

where σ is the activation function which is applied on each unit element by element, super-

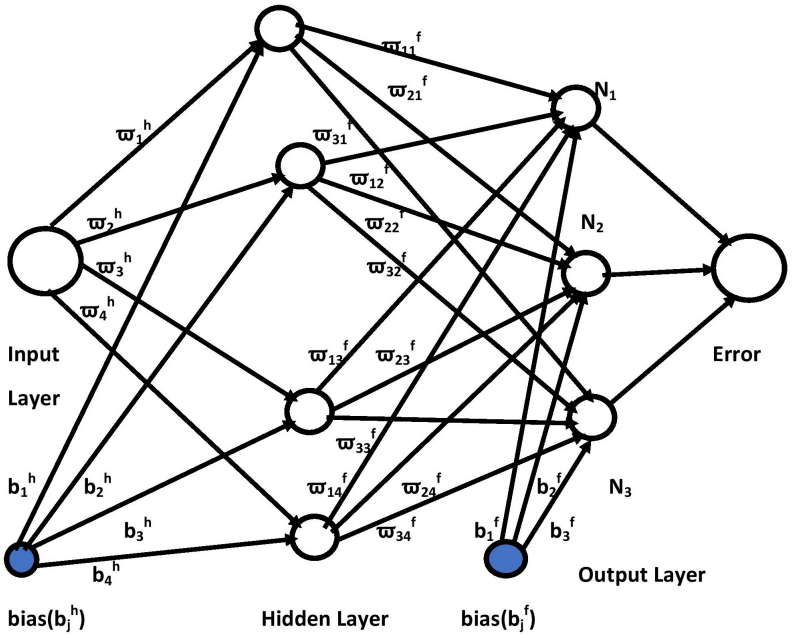

Figure 3.1: "Feed Forward Neural Network."

script h is for the hidden layer and f is for the final layer. To determine the solutions of a system of m differential equations, a single neural network with m outputs can be used.

Since we have three coupled non-linear differential equations, we have considered three outputs $N_1(\eta_i, P_1)$, $N_2(\eta_i, P_2)$ and $N_3(\eta_i, P_3)$ as shown in Fig. (3.1). These Network outputs $N_1(\eta_i, P_1)$, $N_2(\eta_i, P_2)$ and $N_3(\eta_i, P_3)$ denote the trial solution for f, θ and ϕ respectively with the adjustable parameters P_1, P_2 and P_3 respectively, which are given by the expressions.

$$\left.\begin{aligned} N_1(\eta_i, P_1) &= \sum_{j=1}^{k} \varpi_{1j}^f \sigma\{\varpi_j^h \eta_i + b_j^h\} + b_1^f \\ N_2(\eta_i, P_2) &= \sum_{j=1}^{k} \varpi_{2j}^f \sigma\{\varpi_j^h \eta_i + b_j^h\} + b_2^f \\ N_3(\eta_i, P_3) &= \sum_{j=1}^{k} \varpi_{3j}^f \sigma\{\varpi_j^h \eta_i + b_j^h\} + b_3^f \end{aligned}\right\} \tag{3.13}$$

where, ϖ_j^h represents the weights from the input layer to the j^{th} hidden neuron, b_j^h is the bias term in the hidden layer, ϖ_{1j}^f is the weight from the j^{th} hidden neuron to the first output

neuron, b_1^f is the bias term and ϖ_{2j}^f is the weight from the j^{th} hidden neuron to the second output neuron, b_3^f is the bias term and ϖ_{3j}^f is the weight from the j^{th} hidden neuron to the third output neuron b_3^f is the bias term. P_1 corresponds to the parameters ϖ_j^h, b_j^h, ϖ_{1j}^f, b_1^f, P_2 corresponds to the parameters ϖ_j^h, b_j^h, ϖ_{2j}^f and b_2^f respectively and P_3 corresponds to the parameters ϖ_j^h, b_j^h, ϖ_{3j}^f, b_3^f.

Substituting Eq. (3.13) in the differential equations Eq. (3.7) - Eq. (3.9), we get

$$E_f = (1+\frac{1}{\beta})N_1'''(\eta_i,P_1) + 2N_1(\eta_i,P_1)N_1''(\eta_i,P_1) - (N_1'(\eta_i,P_1))^2 - A(N_1'(\eta_i,P_1) + \frac{\eta_i}{2}N_1''(\eta_i,P_1)) \tag{3.14}$$

$$E_\theta = \frac{1}{Pr}N_2''(\eta_i,P_2) + D_f N_3''(\eta_i,P_3) - N_1'(\eta_i,P_1)N_2(\eta_i,P_2) + 2N_1(\eta_i,P_1)N_2'(\eta_i,P_2) - A(N_2(\eta_i,P_2) + \frac{\eta_i}{2}N_2'(\eta_i,P_2)) \tag{3.15}$$

$$E_\phi = \frac{1}{Sc}N_3''(\eta_i,P_3) + S_r N_2''(\eta_i,P_2) - N_1'(\eta_i,P_1)N_3(\eta_i,P_3) + 2N_1(\eta_i,P_1)N_3'(\eta_i,P_3) - A(N_3(\eta_i,P_3) + \frac{\eta_i}{2}N_3'(\eta_i,P_3)) \tag{3.16}$$

where E_f, E_θ and E_ϕ represents the errors or residuals with respect to the equations Eq. (3.7), Eq. (3.8) and Eq. (3.4) respectively. If the trial/constructed solutions for f, θ and ϕ given in Eq. (3.13) are close to exact solution then the errors E_f, E_θ and $E_\phi$tend to zero.

The corresponding boundary conditions are transformed to:

$$\left.\begin{aligned} &N_1(\eta_1,P_1) = S;\ N_1'(\eta_1,P_1) = 1;\ N_2(\eta_1,P_2) = 1;\ N_3(\eta_1,P_3) = 1 \\ &N_1'(\eta_n,P_1) = 0;\ N_2(\eta_n,P_2) = 0 \,\text{and}\, N_3(\eta_n,P_3) = 0 \end{aligned}\right\} \tag{3.17}$$

The mean square of error (MSE) is calculated by taking $1/n$ times the sum of the squared errors of differential equations (Eqs. (3.14) - (3.16)) along with the error in the boundary conditions Eqs. (3.17) on the training set and then minimized. The solution produced by determining a set of biases and weights that minimizes the MSE (or loss function) after training is the final solution of the problem. Hence, the MSE or loss function $\mathfrak{E}(P_1,P_2,P_3)$

is given by

$$\mathfrak{E}(P_1, P_2, P_3) = \frac{1}{n}\sum_{i=1}^{n} (E_f)^2 + (E_\theta)^2 + (E_\phi)^2 + [N_1(\eta_1, P_1) - S]^2 + [N_1'(\eta_1, P_1) - 1]^2$$
$$+ +[N_1'(\eta_n, P_1)]^2 + [N_2(\eta_1, P_2) - 1]^2 + [N_2(\eta_n, P_2)]^2 + [N_3(\eta_1, P_3) - 1]^2 + [N_3(\eta_n, P_3)]^2 \tag{3.18}$$

where 4^{th} - 11^{th} terms in the above expression represents represent error terms corresponding to the boundary conditions.

The goal is to reduce $\mathfrak{E}(P_1, P_2, P_3)$ by optimising the weights and biases of the network for a particular network configuration. The derivatives of the network output with respect to its input must be computed in order to compute the error $\mathfrak{E}(P_1, P_2, P_3)$. The derivative of networks output $N_1(\eta_i, P_1)$, $N_2(\eta_i, P_2)$ and $N_3(\eta_i, P_3)$ with respect to input vector η_i are calculated using Python package called autograd. Backpropagation can then be used to pursue the optimization by evaluating the derivatives of the loss function with respect to the network parameters. Here in this paper, we used a single hidden layer, Sigmoid activation function, the Adam optimizer [38] with an initial learning rate of 0.01.

To apply this method the semi-infinite domain of the given problem i.e. $[0, \infty]$ is reduced to $[0, \eta_\infty]$ where η_∞ is the parameter used to recover the boundary conditions at infinity.We start with training points that are chosen from the domain of the given problem i.e. $[0, \eta_\infty]$, where ($\eta_\infty = 6.0$) and the weights and bias terms, which are generated randomly and we train the model to modify the parameters in the given domain of the problem. We use the entire set of training points to ensure that the boundary conditions in the loss are incorporated into each network parameter update. In general, we find that a single hidden layer with a small number of units is enough to get very exact results. Here in this paper, we used a single hidden layer, Sigmoid activation function, the Adam optimizer [38] with an initial learning rate of 0.01.

To check the convergence of the solution of the method, the dimensionless coefficient of skin friction ($f''(0)$), rate of heat transfer ($\theta'(0)$) and Sherwood number ($\phi'(0)$) are calculated by choosing different number of training points 30, 50 and 100 and different number of

neurons 5, 10, 15 and 30 in the hidden layer.The computed results are presented in Tables (3.1) and (3.2). It is evident from Tables (3.1) and (3.2) that the solution has convergence of 10^{-4} when the data points are 50 and hidden neurons are 10.

Number Of Data points	$f''(0)$	$\theta'(0)$	$\phi'(0)$
30	-1.45817261	-1.17214455	-0.57090268
50	-1.45802749	-1.17205221	-0.57088971
100	-1.45790606	-1.17202807	-0.57087213

Table 3.1: "Convergence analysis for the values of $f''(0)$, $\theta'(0)$ and $\phi'(0)$ at the surface for $A = 0.5$, $S = 0.5$, $Pr = 1.0$, $Sc = 0.2$, $D_f = 0.5$ and $S_r = 0.2$ with different number of Data points."

Number of neurons	$f''(0)$	$\theta'(0)$	$\phi'(0)$
5	-1.45817261	-1.17214455	-0.57090268
10	-1.45785345	-1.17215167	-0.57096305
15	-1.45806307	-1.17195968	-0.5709956
30	-1.4579798	-1.17220332	-0.57086201

Table 3.2: "Convergence analysis for the values of $f''(0)$, $\theta'(0)$ and $\phi'(0)$ at the surface $A = 0.5$, $S = 0.5$, $Pr = 1.0$, $Sc = 0.2$, $D_f = 0.5$ and $S_r = 0.2$ with different number of hidden neurons".

3.4 Computational Results and Discussion

In present study, the coefficient of skin friction C_f, Nusselt Number N_u and Sherwood number Sh are computed for different values of unsteadiness parameter A, Casson fluid parameter β, Prandtl number Pr, suction / injection parameter S, Schmidth number Sc, Dufour number D_f and Soret number S_r and depicted graphically. To evaluate the impact of factors involved, numerical computations are done with $A = 0.5$, $S = 0.5$, $Pr = 1.0$, $\beta = 1.0$, $Sc = 0.2$, $S_r = 0.2$ and $D_f = 0.5$ unless otherwise stipulated. The Artificial Neural Network method (ANN) along with Adam optimization is applied to solve the Eqs. (3.7) - (3.9) The code is written in Python and executed for different parameters.

The effectiveness of the method is also validated by relating the current numerical results of coefficient of skin friction, heat transfer coefficient and mass transfer coefficient with *bvp4c* routine of MATLAB for $A = 0.5$, $S = 0.5$, $Pr = 1.0$, $Sc = 0.2$, $D_f = 0.5$ and $S_r = 0.2$. The

computed results are presented in Table 3.3. It is evident from Table (3.3) that the present results are are consistent with the results obtained by using bvp4c method.

$f''(0)$		$\theta'(0)$		$\phi'(0)$	
Present	bvp4c	Present	bvp4c	Present	bvp4c
-1.45806307	-1.45776561	-1.17195968	-1.17114305	-0.5709956	-0.55784575

Table 3.3: "Comparative analysis for the values of $f''(0)$, $\theta'(0)$ and $\phi'(0)$ at the surface by the present method with the results of bvp4c method".

A comparison of obtained results is established for Skin friction coefficient and Nusselt number with existing works for $\beta = \infty$, $D_f = 0.0$, $Sc = 0.0$ and $S_r = 0.0$. Table 3.4 shows a well justifying comparisons of our results and [81] results for $f''(0)$ and $\theta'(0)$.

A	S	Pr	$f''(0)$		$\theta'(0)$	
			Present Value	Shahzad *et al.* [81]	Present Value	Shahzad *et al.* [81]
0.5	-1	1	-0.620406	-0.620400	-0.620443	-0.620400
0.5	-0.5	1	-0.887208	-0.887200	-0.887623	-0.887200
0.5	0	1	-1.308334	-1.308999	-1.308925	-1.308999
0.5	0.5	1	-1.906700	-1.907999	-1.908495	-1.907999
0.5	1	1	-2.653536	-2.655999	-2.656215	-2.655999
0	0.5	1	-1.798938	-1.798999	-1.799092	-1.798999
1	0.5	1	-2.015453	-2.016999	-2.017439	-2.016999
0.5	0.5	0.5	-1.906859	-1.907999	-1.121147	-1.119999
0.5	0.5	0.7	-1.907159	-1.907999	-1.450060	-1.450000

Table 3.4: "Comparative analysis for the values of $f''(0)$ and $\theta'(0)$ by the present method with the results of Shahzad *et al.* [81]".

Fig. 3.2 illustrates the plot of error (between ANN method and Shooting technique results) in the values of $f'(\eta)$, $\theta(\eta)$, and $\phi(\eta)$ for 7 equi-spaced positions in $[0, 6]$. The present method's (ANN method) conclusions are in perfect accord with those produced by Shooting method. as shown in Figure 3.2.

The impact of unsteadiness parameter on the coefficient of skin friction ($f''(0)$), rate of heat transfer ($-\theta'(0)$) and rate of mass transfer ($-\phi'(0)$) is presented in Figs. 3.3. An escalate in the parameter A declines the skin friction coefficient $f''(0)$ as shown in Fig. 3.3(a). It is observed from Figs. 3.3(b) and 3.3(c) that $\theta'(0)$ and ($\phi'(0)$) are enhancing as the value of the parameter A enhances.

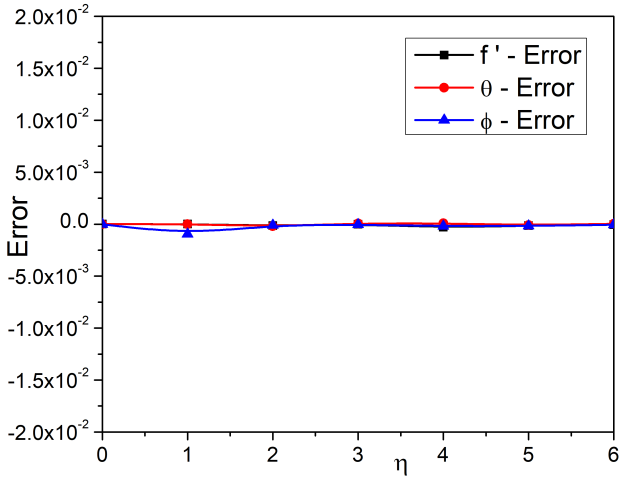

Figure 3.2: "Error plot between the results obtained by Artificial Neural Network method and Shooting method for the values of velocity, temperature and concentration profiles."

Figure 3.4 provides the impact of Dufour number D_f on $f''(0)$, $-\theta'(0)$ and $-\phi'(0)$. As shown in Fig. 3.4(a), the skin friction coefficient appears to be unaffected by changes in D_f. Figures 3.4(b) and 3.4(c) show that as D_f increases, the Nusselt number decreases and the Sherwood number increases.

In Fig. 3.5, the significance of the Prandtl number Pr on the coefficient of skin friction $f''(0)$, heat transfer rate $(-\theta'(0))$ and mass transfer rate $(-\phi'(0))$ is presented. The Nusselt number rises and the Sherwood number falls when the Prandtl number Pr rises, as seen in Figs. 3.5(b) and 3.5(c), although Skin friction remains constant as given in Fig. 3.5(b)

The impact of suction/injection parameter S on $f''(0)$, $-\theta'(0)$ and $-\phi'(0)$ is presented in Fig. 3.6. It is seen from Fig.3.6(a) that the skin friction is decreasing as the as the values of S increases. The values of $-\theta'(0)$ and $-\phi'(0)$ are increasing as the values of S is increasing as depicted in Figs.3.6(b) and 3.6(c).

In Fig. 3.7 the effect of Schmidth number Sc on the coefficient of skin friction $f''(0)$, Nusselt number $(-\theta'(0))$ and Sherwood number $(-\phi'(0))$ is discussed. It is observed that skin friction coefficient remains unchanged with the change in Sc as given in Fig.3.7(a). It is observed from the Figs. 3.7(b) and 3.7(c) thatt the Nusselt number diminishes and the

Sherwood number rises as Sc increases respectively.

In Fig. 3.8 the effect of Soret number S_r on the coefficient of skin friction $f''(0)$, Nusselt number $(-\theta'(0))$ and Sherwood number $(-\phi'(0))$ is presented. The skin friction coefficient does not vary with the change in S_r, as seen in Fig.3.8(a). As S_r rises, the Nusselt number rises and the Sherwood number falls, as shown in 3.8(b) and 3.8(c).

3.5 Conclusions

The coupled nonlinear differential equations emerging from the boundary layer flow of a Casson fluid over a radially expanding sheet with the influence of suction/injection at the surface, Soret and Dufor is solved Artificial Neural Network approach. The Adams optimization method was used to minimize the error function and to determine the optimal values for the trial function's adjustable parameters. The numerical results achieved show extremely good precision when compared to those acquired utilizing the shooting method. Furthermore, the accuracy of the neural network improves as the number of neurons increases. The influences of the parameters A, β, Pr, Sc, D_f, S_r and S on the relevant physical quantities are investigated. The important findings are presented below.

- The skin friction decreases with the enhancement in unsteadiness parameter and suction/injection parameter.
- The Nusselt number increases when unsteadiness parameter, Prandtl number, suction/injection parameter and Soret number increases and there is a decrement in it with the increased values of Dufour number and Schmdith number.
- The Sherwood number rises as unsteadiness parameter, Dufour parameter, suction/injection parameter and Schmidth number increases and reduced when Prandtl number and Soret number increased.

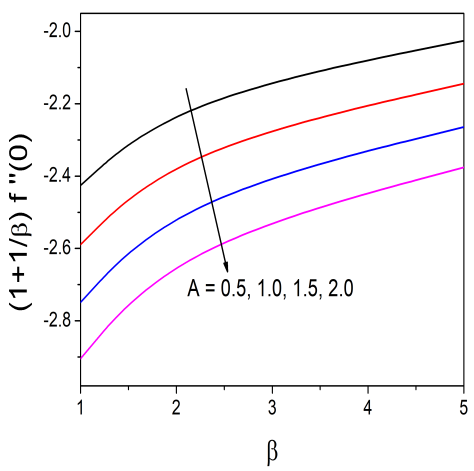

(a)

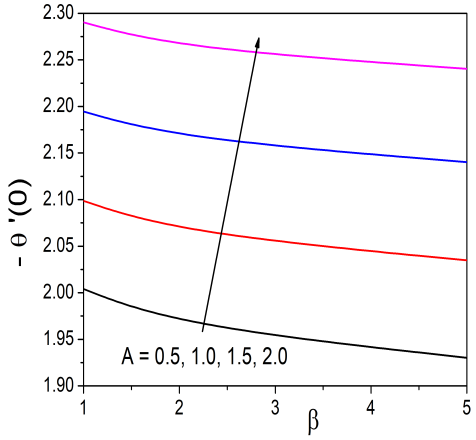

(b)

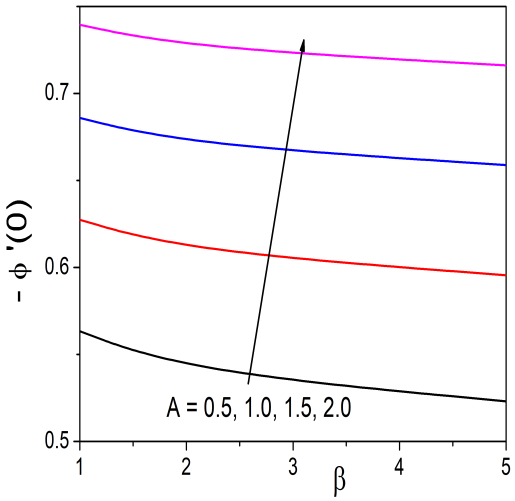

(c)

Figure 3.3: "Variation of $f''(0)$, $-\theta'(0)$ and $-\phi'(0)$ with unsteadiness parameter A".

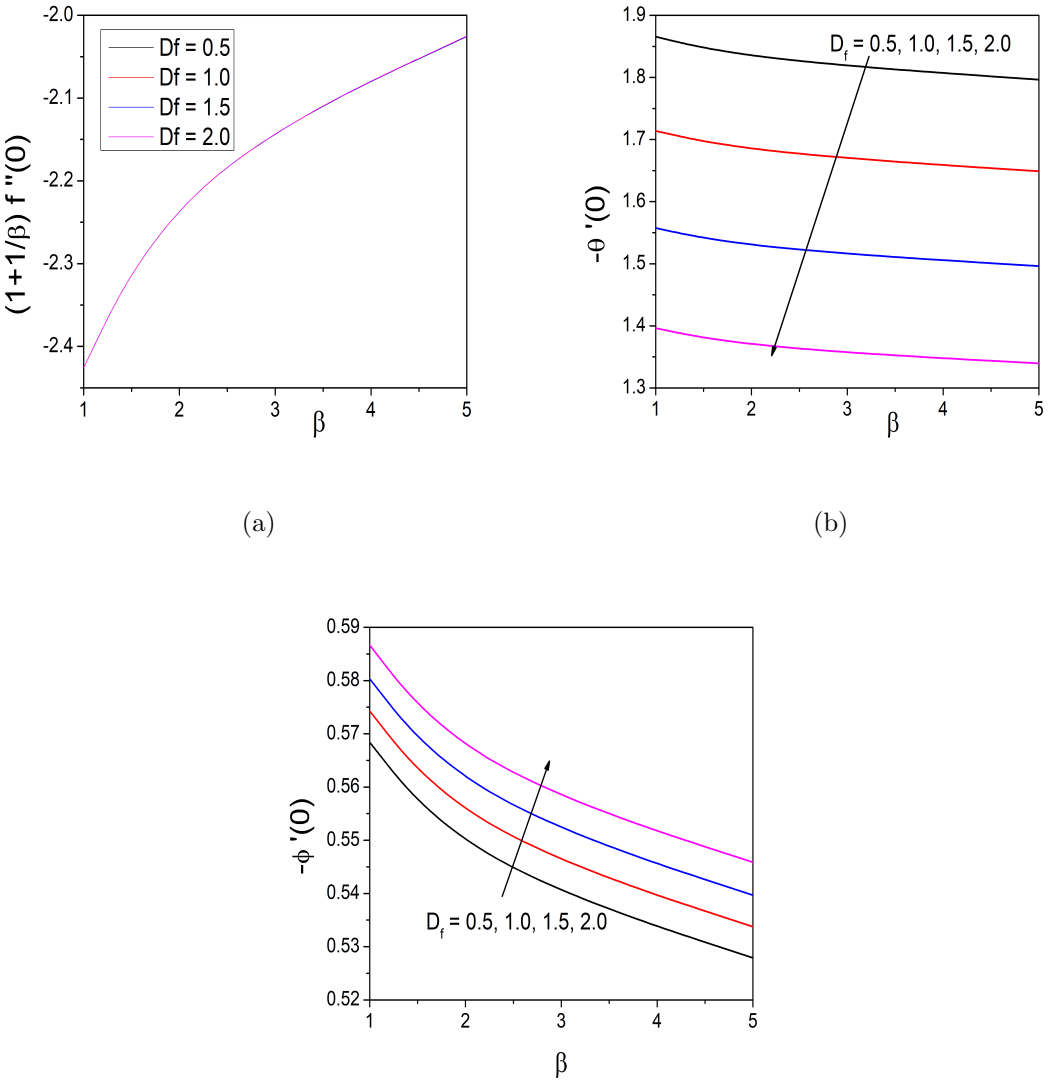

(a) (b)

(c)

Figure 3.4: "Plot of $f''(0)$, $-\theta'(0)$ and $-\phi'(0)$ for various values of the Dufour number D_f."

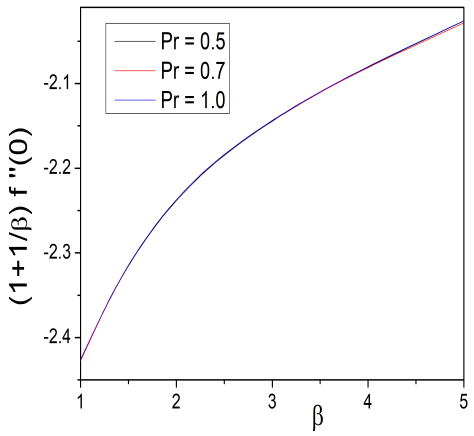

(a)

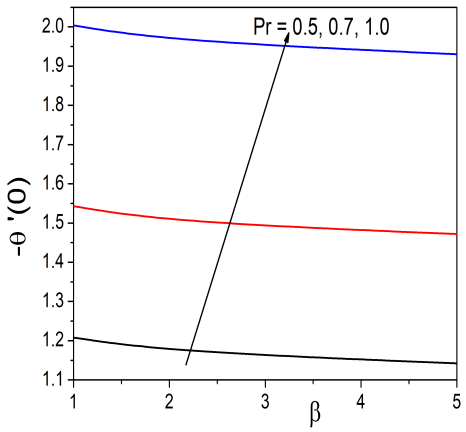

(b)

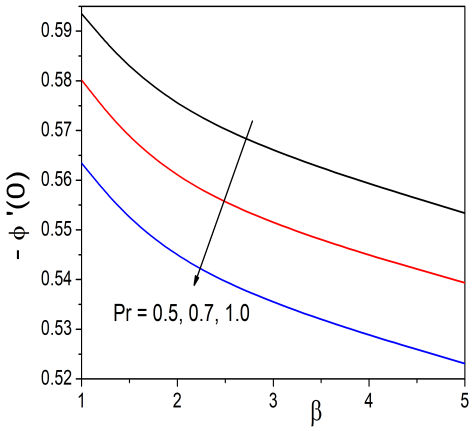

(c)

Figure 3.5: "Plot of $f''(0)$, $-\theta'(0)$ and $-\phi'(0)$ for various values of the Prandtl number Pr."

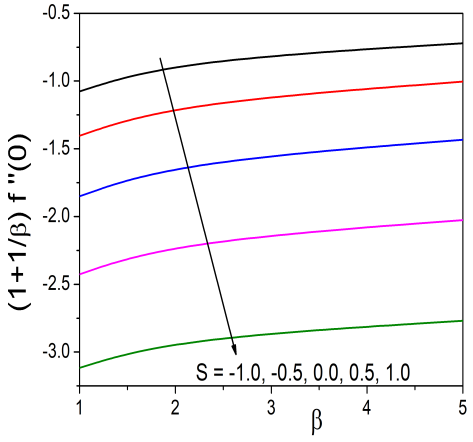

(a)

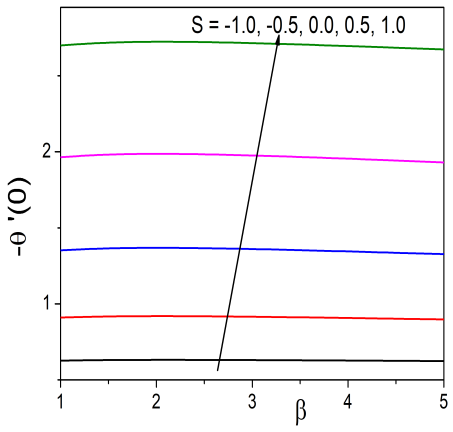

(b)

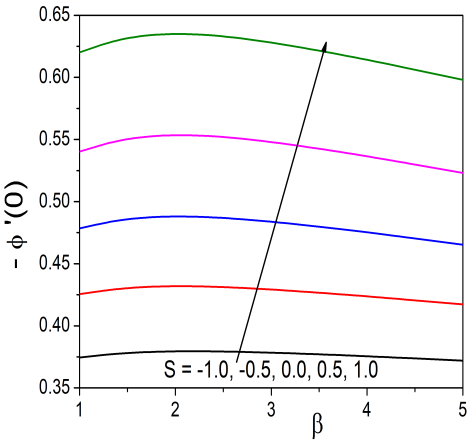

(c)

Figure 3.6: "Plot of $f''(0)$, $-\theta'(0)$ and $-\phi'(0)$ for various values of the Suction/Injection parameter S."

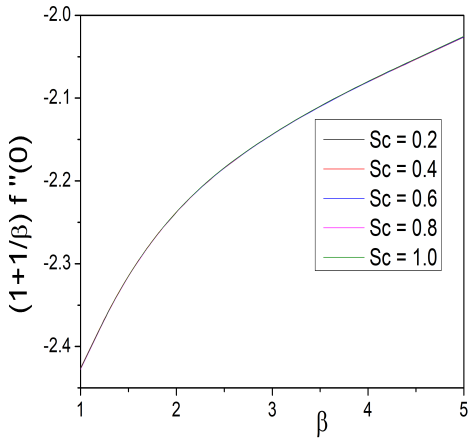

(a)

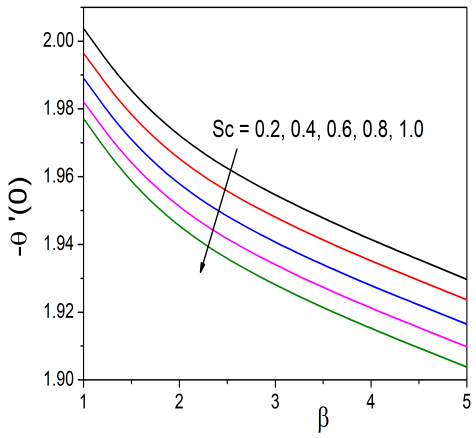

(b)

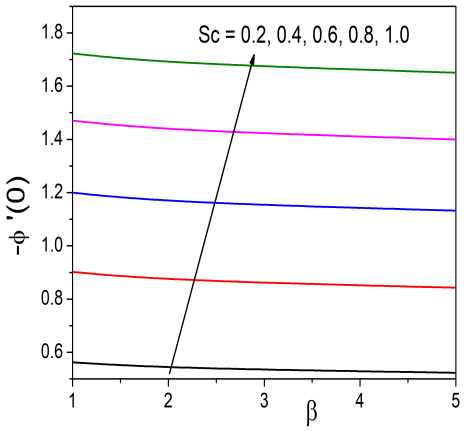

(c)

Figure 3.7: "Plot of $f''(0)$, $-\theta'(0)$ and $-\phi'(0)$ for various values of the Schmidth number Sc."

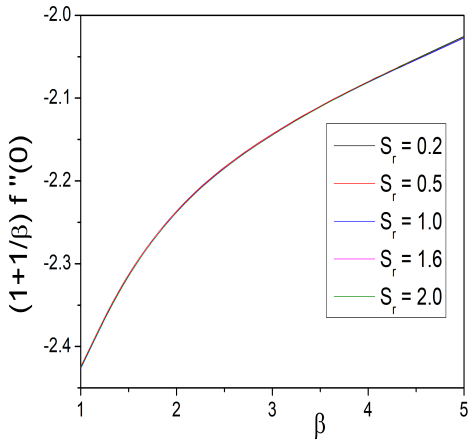

(a)

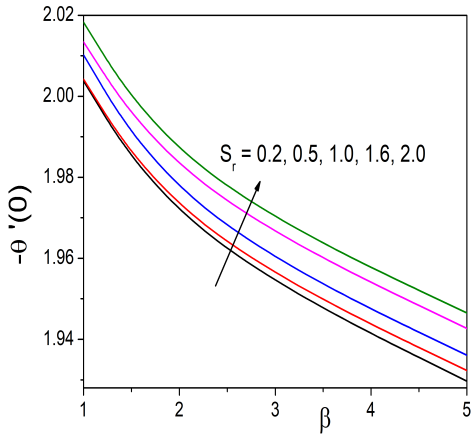

(b)

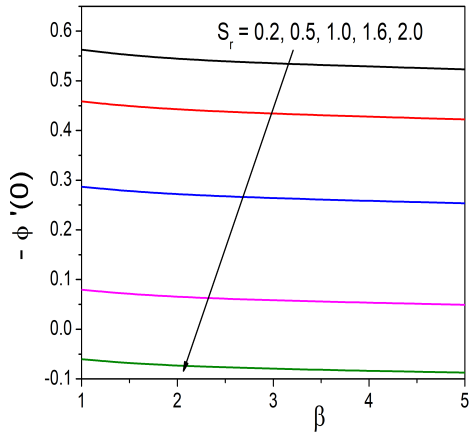

(c)

Figure 3.8: "Plot of $f''(0)$, $-\theta'(0)$ and $-\phi'(0)$ for various values of the Soret number S_r."

Chapter 4

Artificial Neural Networks Based Computational Method for Bioconvection in a Casson Fluid Flow Past an Unsteady Radially Stretching Sheet [1]

4.1 Introduction

Microorganisms, such as microalgae and bacteria, have a higher density than water and so move upwards against gravity. Microbe accumulation causes the top layer of suspension to be denser than the bottom layer, resulting in an unstable density distribution. Convective instability occurs as a result, which may result in convection patterns. The spontaneous and unpredictable movement patterns of microorganisms in suspension are referred to as bioconvection. Chemical processes have a critical role in bioconvection in the presence of motile bacteria due to their importance in food processing, material synthesis, polymer creation,

[1] Communicated to"**Heat Transfer**"

bioreactors, fuel cells, and biodiesel fuels. Pedley *et al.* [63] coined the term bioconvection to describe tiny convection caused by motile microorganisms. Babu *et al.* [9] demonstrated bioconvective non-aligned magnetohydrodynamic stagnation point flow across a stretching sheet. Pal *et al.* [62] explored the impact of thermal radiation on the water-based nanofluid flow over an exponentially stretching sheet in the presence of motile gyrotactic microorganisms . Ray *et al.* [69] numerically investigated the unsteady bioconvection in a Casson thin film with uniform thickness over a horizontal elastic sheet emerging from a slit in the presence of viscous dissipation and magnetic effect. Sabir *et al.* [75] explored the two-phase Casson nanofluid passing through a stretching sheet along a permeable surface with the effects of chemical reactions and gyrotactic microorganisms. Magagula *et al.* [46] studied the double dispersed bioconvection phenomena for a Casson nanofluid flow over a nonlinear stretching sheet. Sankad *et al.* [79] considered bioconvection of MHD flow, heat and mass exchange of Casson fluid containing gyrotactic microorganisms above a linearly stretching surface. Kumaraswamy *et al.* [53] focused on the impact of motile gyrotactic microorganisms and thermal heat flux on three-dimensional convective flow of a Casson nanoliquid over an elongated surface.

The bioconvection in a Casson fluid flow across a time radial sheet with time dependent stretching velocity is examined in this chapter. ANN is used to calculate the problem's solution. Graphs are used to show how important parameters affect the flow properties.

4.2 Mathematical Formulation

Consider a unsteady two dimensional and laminar flow of a Casson fluid over a stretching surface $z = 0$ as shown in Fig. (2.1). In addition to the assumptions made in Chapter 2, here we assume that the the concentration of the motile microorganisms at the surface is $\mathbb{N}_w = \mathbb{N}_\infty + \dfrac{br}{1-ct}$, where $\mathbb{N}_\infty$ is the concentration of the microbes at the ambient medium.

Hence, the equations describing the flow are given by

$$\frac{\partial u}{\partial r} + \frac{u}{r} + \frac{\partial w}{\partial z} = 0 \tag{4.1}$$

$$\frac{\partial u}{\partial t} + u\frac{\partial u}{\partial r} + w\frac{\partial u}{\partial z} = \nu(1 + \frac{1}{\beta})\frac{\partial^2 u}{\partial z^2} \tag{4.2}$$

$$\frac{\partial T}{\partial t} + u\frac{\partial T}{\partial r} + w\frac{\partial T}{\partial z} = \alpha\frac{\partial^2 T}{\partial z^2} \tag{4.3}$$

$$\frac{\partial C}{\partial t} + u\frac{\partial C}{\partial r} + w\frac{\partial C}{\partial z} = D_s\frac{\partial^2 C}{\partial z^2} \tag{4.4}$$

$$\frac{\partial \mathbb{N}}{\partial t} + u\frac{\partial \mathbb{N}}{\partial r} + w\frac{\partial \mathbb{N}}{\partial z} + \frac{bW_c}{C_w - C_\infty}(\frac{\partial}{\partial z}(\mathbb{N}\frac{\partial C}{\partial z})) = D_m\frac{\partial^2 \mathbb{N}}{\partial z^2} \tag{4.5}$$

where $\mathbb{N}(r, z, t)$ denotes the density of the motile microorganisms, the microorganism diffusivity is represented by D_m, c is the Chemotaxis constant and W_c is the maximum cell swimming speed.

The boundary conditions are:

$$\begin{aligned} &u = U_w, w = W_0, T = T_w = T_\infty + \frac{br}{1-ct}, C = C_w + \frac{br}{1-ct}, \mathbb{N} = \mathbb{N}_w + \frac{br}{1-ct} atz = 0 \\ &u \to 0, T \to T_\infty, C \to C_\infty, \mathbb{N} \to \mathbb{N}_\infty \quad as \quad z \to \infty \end{aligned} \tag{4.6}$$

where $W_0 = -2S\left(\frac{\nu U_w}{r}\right)^{1/2}$, U_w the stretching velocity. Here at the surface, $W_0 > 0$ ($S < 0$) represents injection and $W_0 < 0$ ($S > 0$) represents suction.

Introducing the stream function $\psi(r, z)$ through

$$u = -\frac{1}{r}\frac{\partial \psi}{\partial z} \qquad \text{and} \qquad w = \frac{1}{r}\frac{\partial \psi}{\partial r} \tag{4.7}$$

and the following similarity transformations

$$\left.\begin{aligned} &\psi(r, z) = -r^2 U_w \mathrm{Re}^{-1/2} f(\eta), \quad \eta = \frac{z}{r}\mathrm{Re}^{1/2}, \quad \theta = \frac{T - T_\infty}{T_w - T_\infty}, \\ &\phi(\eta) = \frac{C - C_\infty}{C_w - C_\infty} \quad \text{and} \quad \chi(\eta) = \frac{\mathbb{N} - \mathbb{N}_\infty}{\mathbb{N}_w - \mathbb{N}_\infty} \end{aligned}\right\} \tag{4.8}$$

into equations 4.1 - 4.5, we get

$$(1+\frac{1}{\beta})f'''+2ff''-(f')^2-A(f'+\frac{\eta}{2}f'')=0 \tag{4.9}$$

$$\frac{1}{Pr}\theta''+2f\theta'-f'\theta-A(\theta+\frac{\eta}{2}\theta')=0 \tag{4.10}$$

$$\frac{1}{Sc}\phi''+2f\phi'-f'\phi-A(\phi+\frac{\eta}{2}\phi')=0 \tag{4.11}$$

$$\chi''-Sb(A(\chi+\frac{\eta}{2}\chi')+f'\chi-2f\chi')-P_e(\phi'\chi'+\sigma_b\phi''+\chi\phi'')=0 \tag{4.12}$$

where $Sb=\frac{\nu}{D_m}$ is bioconvection Schmidth number, $\sigma_b=\frac{\mathbb{N}_\infty}{\mathbb{N}_w-\mathbb{N}_\infty}$ is dimensionless bioconvection constant and $P_e=\frac{bW_c}{D_m}$ is bioconvection Peclet number. The remaining parameters are defined in the previous chapters

The corresponding conditions on the surface are:

$$\left.\begin{aligned} &f(\eta)=S, f'(\eta)=1, \theta(\eta)=1, \phi(\eta)=1, \chi(\eta)=1 \quad \text{at} \quad \eta=0 \\ &f'(\eta)\to 0,\ \theta(\eta)\to 0,\ \phi(\eta)\to 0,\ \chi(\eta)\to 0 \quad \text{as} \quad \eta\to\infty \end{aligned}\right\} \tag{4.13}$$

The coefficient of skin friction C_f, the rate of heat transfer (Nusselt number) N_u, the rate of mass transfer (Sherwood number) Sh and local density number of the motile microorganism N_n in dimensionless form are given by

$$\frac{1}{2}\sqrt{Re}C_f=(1+\frac{1}{\beta})f''(0),\ \frac{N_u}{\sqrt{Re}}=-\theta'(0)\ \frac{Sh}{\sqrt{Re}}=-\phi'(0)\ \text{and}\ \frac{N_n}{\sqrt{Re}}=-\chi'(0) \tag{4.14}$$

4.3 Method of Solution

Consider a multilayered perceptron consisting of 3– layers namely input layer - consisting of 'n' inputs $\bar{\eta}$=$(\eta_1,\eta_2,...\eta_n)$, hidden layer - consisting of 'k' neurons and output layer consisting of 4 – neurons $N_1(\eta_i,P_1)$, $N_2(\eta_i,P_2)$, $N_3(\eta_i,P_3)$ and $N_4(\eta_i,P_4)$ to estimate the solutions of four coupled nonlinear ordinary differential equations as shown in the Fig.4.1.

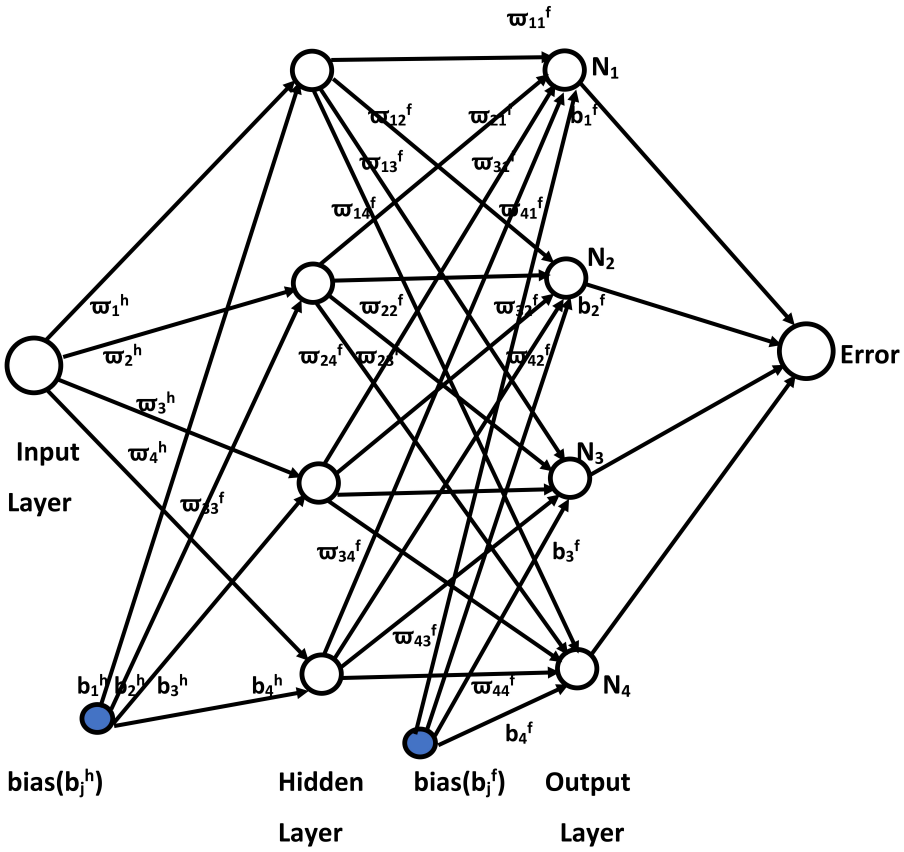

Figure 4.1: "Feed Forward Neural Network."

We take the Network outputs $N_1(\eta_i, P_1)$, $N_2(\eta_i, P_2)$, $N_3(\eta_i, P_3)$ and $N_4(\eta_i, P_4)$ as the trial solution for f, θ, ϕ and χ with the adjustable parameters P_1, P_2, P_3 and P_4 respectively, which are given by the expressions.

$$\left.\begin{aligned} N_1(\eta_i, P_1) &= \sum_{j=1}^{k} \varpi_{1j}^f \sigma\{\varpi_j^h \eta_i + b_j^h\} + b_1^f\,; \quad N_2(\eta_i, P_2) = \sum_{j=1}^{k} \varpi_{2j}^f \sigma\{\varpi_j^h \eta_i + b_j^h\} + b_2^f \\ N_3(\eta_i, P_3) &= \sum_{j=1}^{k} \varpi_{3j}^f \sigma\{\varpi_j^h \eta_i + b_j^h\} + b_3^f\,; \quad N_4(\eta_i, P_4) = \sum_{j=1}^{k} \varpi_{4j}^f \sigma\{\varpi_j^h \eta_i + b_j^h\} + b_4^f \end{aligned}\right\} \quad (4.15)$$

where, ϖ_j^h represents the weights from the input layer to the j^{th} hidden neuron, b_j^h is the bias term in the hidden layer, ϖ_{1j}^f is the weight from the j^{th} hidden neuron to the first output neuron, b_1^f is the bias term, ϖ_{2j}^f is the weight from the j^{th} hidden neuron to the

second output neuron, b_2^f is the bias term, ϖ_{3j}^f is the weight from the j^{th} hidden neuron to the third output neuron b_3^f is the bias term, ϖ_{4j}^f is the weight from the j^{th} hidden neuron to the fourth output neuron b_4^f is the bias term, P_1 corresponds to the parameters ϖ_j^h, b_j^h, ϖ_{1j}^f, b_1^f, P_2 corresponds to the parameters ϖ_j^h, b_j^h, ϖ_{2j}^f and b_2^f respectively, P_3 corresponds to the parameters ϖ_j^h, b_j^h, ϖ_{3j}^f, b_3^f and P_4 corresponds to the parameters ϖ_j^h, b_j^h, ϖ_{4j}^f, b_4^f.

Since there are no data available in order to learn from the differential equation, we have to substitute Eq. (4.15) in the differential equations Eq. (4.9) - Eq. (4.12). Hence, we get

$$\begin{aligned} E_f = (1+\frac{1}{\beta}){N_1}'''(\eta_i,P_1) + 2N_1(\eta_i,P_1){N_1}''(\eta_i,P_1) - N_1(\eta_i,P_1)^2 - A({N_1}'(\eta_i,P_1) \\ + \frac{\eta_i}{2}{N_1}''(\eta_i,P_1)) \end{aligned} \tag{4.16}$$

$$\begin{aligned} E_\theta = \frac{1}{Pr}{N_2}''(\eta_i,P_2) + 2N_1(\eta_i,P_1){N_2}'(\eta_i,P_2) - {N_1}'(\eta_i,P_1)N_2(\eta_i,P_2) - A(N_2(\eta_i,P_2) \\ + \frac{\eta_i}{2}{N_2}'(\eta_i,P_2)) \end{aligned} \tag{4.17}$$

$$\begin{aligned} E_\phi = \frac{1}{Sc}{N_3}''(\eta_i,P_3) + 2N_1(\eta_i,P_1){N_3}'(\eta_i,P_3) - {N_1}'(\eta_i,P_1)N_3(\eta_i,P_3) - A(N_3(\eta_i,P_3) \\ + \frac{\eta_i}{2}{N_3}'(\eta_i,P_3)) \end{aligned} \tag{4.18}$$

$$\begin{aligned} E_\chi = {N_4}''(\eta_i,P_4) - Sb(A((N_4(\eta_i,P_4) + \frac{\eta}{2}{N_4}'(\eta_i,P_4)) + {N_1}'(\eta_i,P_1)N_4(\eta_i,P_4) \\ - 2N_1(\eta_i,P_1){N_4}'(\eta_i,P_4)) - P_e({N_3}'(\eta_i,P_3){N_4}'(\eta_i,P_4) + \sigma_b{N_4}''(\eta_i,P_4) \\ + N_4(\eta_i,P_4){N_4}''(\eta_i,P_4)) \end{aligned} \tag{4.19}$$

where E_f, E_θ, E_ϕ and E_χ represents the errors or residuals with respect to the equations Eq. (4.9) - Eq. (4.12) respectively. If the trial/constructed solutions for f, θ, ϕ and χ given in Eq. (4.15) are close to exact solution then the errors E_f, E_θ E_ϕ and E_χ tend to zero.

Similarly, the errors in the boundary conditions are given by:

$$\left.\begin{aligned} &N_1(\eta_1,P_1) = S;\ {N_1}'(\eta_1,P_1) = 1;\ N_2(\eta_1,P_2) = 1;\ N_3(\eta_1,P_3) = 1;\ N_4(\eta_1,P_4) = 1 \\ &{N_1}'(\eta_n,P_1) = 0;\ N_2(\eta_n,P_2) = 0;\ N_3(\eta_n,P_3) = 0;\ \textit{and}\ N_4(\eta_n,P_4) = 0 \end{aligned}\right\} \tag{4.20}$$

The mean square of error (MSE) is calculated by taking $1/n$ times the sum of the squared errors of differential equations (Eqs. (4.16) - (4.19)) along with the error in the boundary conditions Eqs. (4.20) on the training set and then minimized. The solution produced by determining a set of biases and weights that minimizes the MSE (or loss function) after training is the final solution of the problem. Hence, the MSE or loss function $\mathfrak{E}(P_1, P_2, P_3, P_4)$ is given by

$$\begin{aligned}\mathfrak{E}(P_1, P_2, P_3, P_4) = \frac{1}{n}\sum_{i=1}^{n} (E_f)^2 + (E_\theta)^2 + (E_\phi) + (E_\chi)^2 + [N_1(\eta_1, P_1) - S]^2 \\ + [N_1'(\eta_1, P_1) - 1]^2 + [N_1'(\eta_n, P_1)]^2 + [N_2(\eta_1, P_2) - 1]^2 + [N_2(\eta_n, P_2)]^2 \\ + [N_3(\eta_1, P_3) - 1]^2 + [N_3(\eta_n, P_3)]^2 + [N_4(\eta_1, P_3) - 1]^2 + [N_4(\eta_n, P_3)]^2\end{aligned} \tag{4.21}$$

where 5^{th} - 13^{th} terms in the above expression represent the sum of squares of the boundary conditions.

The problem is to minimize $\mathfrak{E}(P_1, P_2, P_3, P_4)$ by optimizing the biases and weights in the network for a given network configuration. The derivatives of the network output with respect to its input must be calculated in order to compute the error function $\mathfrak{E}(P_1, P_2, P_3, P_4)$. The derivatives of networks output $N_1(\eta_i, P_1)$, $N_2(\eta_i, P_2)$, $N_3(\eta_i, P_3)$ and $N_4(\eta_i, P_3)$ with respect to input vector η_i are calculated using Python package called autograd. Backpropagation can then be used to pursue the optimization by evaluating the derivatives of the loss function with respect to the network parameters. Here in this paper, we used a single hidden layer, Sigmoid activation function, the Adam optimizer [38] with an initial learning rate of 0.01.

To apply this method the semi-infinite domain of the given problem i.e. $[0, \infty]$ is reduced to $[\eta_1, \eta_\infty]$ where $\eta_1 = 0$, η_∞ is the parameter used to recover the boundary conditions at infinity. We start with training points that are chosen from the domain of the given problem i.e. $[0, \eta_\infty = 10]$ and the weights and bias terms, which are generated randomly and we train the model to modify the parameters in the given domain of the problem.To ensure that the boundary conditions in the loss are integrated into each network parameter update, we use the entire set of training points. In general, we find that a single hidden layer with a small

number of units is enough to get very exact results.

To check the convergence of the solution of the method, the dimensionless coefficient of skin friction ($f''(0)$), rate of heat transfer ($\theta'(0)$), Sherwood number ($\phi'(0)$) and motile micro organism rate ($\chi'(0)$) at the surface for beta = 1.0, $A = 0.5$, $S = 0.5$, $Pr = 1.0$, $Sc = 0.2$, $Sb = 0.1$, $P_e = 0.1$ and $\sigma_b = 0.1$ are calculated by choosing different number of training points 50, 100 and 200 and different number of neurons 10, 20 and 30 in the hidden layer and the computed results are presented in the Tables 4.1 and 4.2. It is evident from the Tables 4.1 and 4.2 that the solution has convergence of 10^{-4} when the Data points are 50 and Hidden neurons are 10.

Number Of training points	$f''(0)$	$\theta'(0)$	$\phi'(0)$	$\chi'(0)$
50	-1.212728	-2.013013	-0.623263	-0.390674
100	-1.212658	-2.012435	-0.623001	-0.389668
200	-1.212571	-2.012150	-0.622169	-0.390758

Table 4.1: "Convergence analysis for the values of $f''(0)$, $\theta'(0)$ ($\phi'(0)$), ($\chi'(0)$) for $A = 0.5$, $S = 0.5$, $Pr = 1.0$, $Sc = 0.2$, $Sb = 0.1$, $P_e = 0.1$ and $\sigma_b = 0.1$ by the present method with different number of Data points and number of Neurons as 10."

Number Of Neurons	$f''(0)$	$\theta'(0)$	$\phi'(0)$	$\chi'(0)$
10	-1.212728	-2.013013	-0.623263	-0.390674
20	-1.215316	-2.012105	-0.622723	-0.390086
30	-1.212531	-2.012195	-0.622899	-0.383008

Table 4.2: "Convergence analysis for the values of $f''(0)$, $\theta'(0)$ ($\phi'(0)$), ($\chi'(0)$) for $A = 0.5$, $S = 0.5$, $Pr = 1.0$, $Sc = 0.2$, $Sb = 0.1$, $P_e = 0.1$ and $\sigma_b = 0.1$ by the present method with different number of Hidden neurons and number of Data points fixed as 50."

4.4 Computational Results and Discussion

The effectiveness of the method is also validated by relating the current numerical results of the dimensionless coefficient of skin friction ($f''(0)$), rate of heat transfer ($\theta'(0)$), Sharewood number ($\phi'(0)$) and motile micro organism rate ($\chi'(0)$) are calculated using the shooting

method in conjunction with the Runge-Kutta fourth order method. for $A = 0.5$, $S = 0.5$, $Pr = 1.0$, $Sc = 0.2$, $Sb = 0.1$, $P_e = 0.1$ and $\sigma_b = 0.1$. The computed results are presented in the Table 4.3. It is evident from the Table 4.3 that the present results are consistent with the results obtained by using shooting method.

	Present method	Shooting method	Relative error
$f''(0)$	-1.21272813	-1.21259476	1.25×10^{-4}
$\theta'(0)$	-2.01301378	-2.01221582	3.96×10^{-4}
$\phi'(0)$	-0.62326329	-0.62294825	5.05×10^{-4}
$\chi'(0)$	-0.39067426	-0.38890631	4.54×10^{-3}

Table 4.3: "Comparative analysis for the values of $f''(0)$, $\theta'(0)$, $(\phi'(0))$ and $(\chi'(0))$at the surface by the present method with the results of Shooting method for $A = 0.5$, $S = 0.5$, $Pr = 1.0$, $Sc = 0.2$, $Sb = 0.1$, $P_e = 0.1$ and $\sigma_b = 0.1$."

Fig.4.2 illustrates the plot of error (between ANN method and Shooting technique results) in the values of f', θ, ϕ and χ for 11 equispaced positions in $[0, 10]$. The findings acquired by the current approach are in excellent agreement with those obtained by the Shooting method, as shown in Fig.4.2.

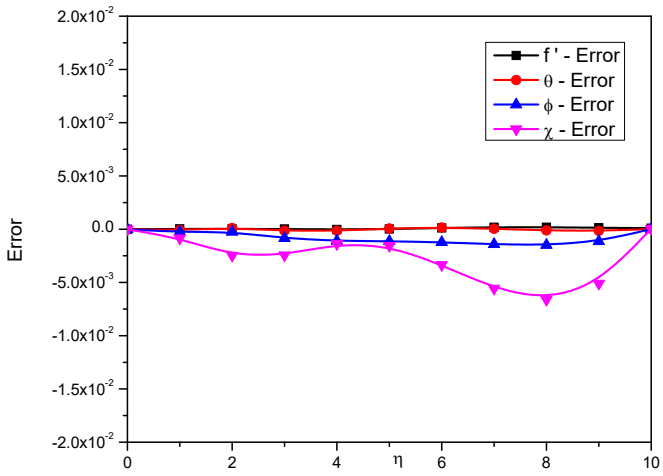

Figure 4.2: "Error plot between the results obtained by Artificial Neural Network method and Shooting method for the values of velocity, temperature, concentration and bioconvection profiles."

The impact of unsteadiness parameter A on the skin friction coefficient $(f''(0))$, Nusselt number $(-\theta'(0))$, Sherwood number $(-\phi'(0))$ and density number of motile microorganisms $(-\chi'(0))$ is presented in Figure 4.3. It is observed from Figure 4.3 that the skin friction is decreasing and Nusselt number, shear stress, density number of motile microorganisms are increasing with the increasing values of the unsteadiness parameter.

Figure 4.4 presents the influence of bioconvection Peclet Pe number on the skin friction coefficient $(f''(0))$, rate of heat transfer $(-\theta'(0))$, rate of mass transfer $(-\phi'(0))$ and density number of motile microorganisms $(-\chi'(0))$. It is evident from Figure 4.4 that the impact of Pe on skin friction coefficient is negligible, whereas the rate of heat transfer, the rate of mass transfer are decreasing slightly and the density number of motile microorganisms is increasing as Pe is increasing.

Figure illustrates how the suction/injection parameter S affects $f"(0)$, $-theta'(0)$, $-phi'(0)$, and $-chi'(0)$. When the values of the suction/injection parameter S increase, it can be seen from Figure 4.5 that skin friction is reducing, while the Nusselt number, Sherwood number,

and density number of motile microorganisms are growing.

The impact of bioconvection Schmidth number Sb, on skin friction coefficient ($f''(0)$), Nusselt number ($-\theta'(0)$), Sherwood number ($-\phi'(0)$) and density number of motile microorganisms ($-\chi'(0)$) is presented in Figure 4.6. It is noticed from Figure 4.6 that there is slight variation in the skin friction and heat transfer rate as the value of Sb is increasing. Also, it demonstrates that the mass transfer rate is rising close to the sheet and falling away from the sheet, and it also shows that the density of motile mocrobes is rising quickly along with rising values of the bioconvection Schmidth number Sb.

The changes in the skin friction coefficient ($f''(0)$), Nusselt number ($-\theta'(0)$), Sherwood number ($-\phi'(0)$) and density number of motile microorganisms ($-\chi'(0)$) with Schmidt number Sc is displayed in Figure 4.7. Figure 4.7 indicates that when the value of Sc rises, there is an improvement in skin friction, the rate of mass transfer, and the density number of motile microorganisms, although the influence of the Schmidth number Sc on the Nusselt number is negligible.

The effect of bioconvection constant σ_b on skin friction coefficient ($f''(0)$), Nusselt number ($-\theta'(0)$), Sherwood number ($-\phi'(0)$) and density number of motile microorganisms ($-\chi'(0)$) is depicted in Figure 4.8. The density of motile microbes is growing as the value of $sigma_b$ rises, as can be shown in Figure 4.8.

4.5 Conclusions

The primary intension of this research is to use the Artificial Neural Network approach to solve coupled nonlinear differential equations emerging from bioconvection in axisymmetric flow of Casson fluid over unsteady radially stretched sheet. Trial solutions were not constructed separately. Network outputs considered as the trial solutions of the non-linear ordinary differential equations involved in the problem. The Adams optimization method was used in minimizing the error function and to determine the optimal values for the trial function's adjustable parameters. The numerical results achieved show extremely good pre-

cision when compared to those acquired utilizing the shooting method. It was discovered that employing a small number of hidden neurons might produce adequate precision. The influence of parameters A, S, Pr, Sc, Sb, P_e and σ_b. The important findings are presented below.

- The skin friction coefficient diminishes with the rising values of unsteadiness factor, suction/injection factor and there is a slight increment in it for the increasing values of bioconvection Schmidth number and Schmidth number.
- Nusselt number increases when unsteadiness parameter, suction/injection parameter, bioconvection Schmidth number increases and it decreases as Peclet number increase.
- At higher values of the Schmidth number, suction/injection parameter, and unsteadiness parameter, the Sherwood number rises; for higher values of the Peclet number, it falls.
- Density number of the motile microorganism increases for all the parameters stated in the problem.

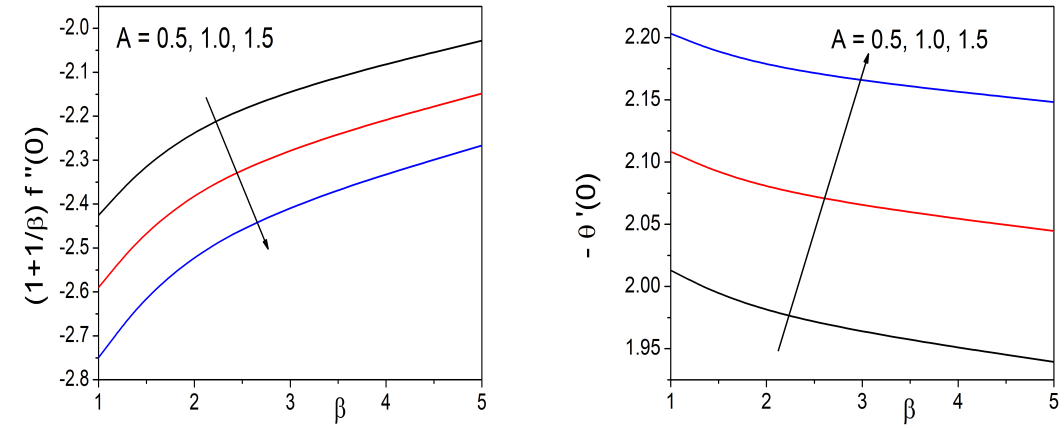

(a)

(b)

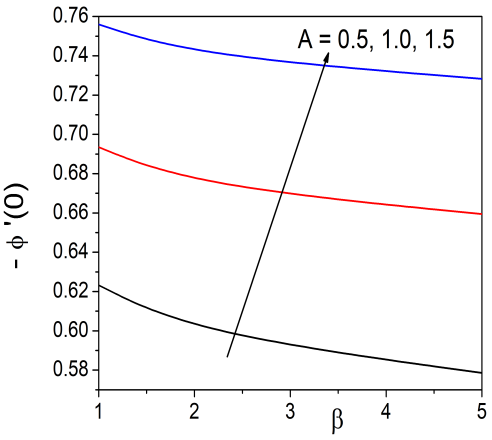

(c)

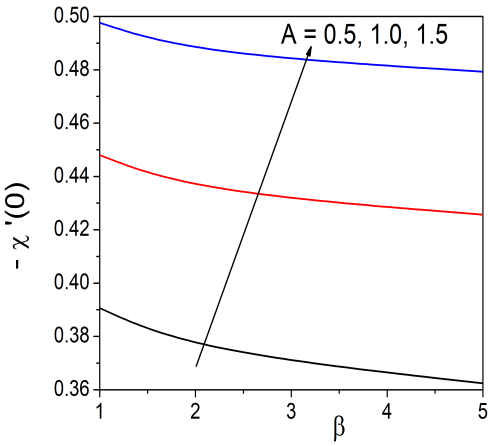

(d)

Figure 4.3: "Plot of $f''(0)$, $-\theta'(0)$, $-\phi'(0)$ and $-\chi'(0)$ for various values of the unsteadiness parameter A."

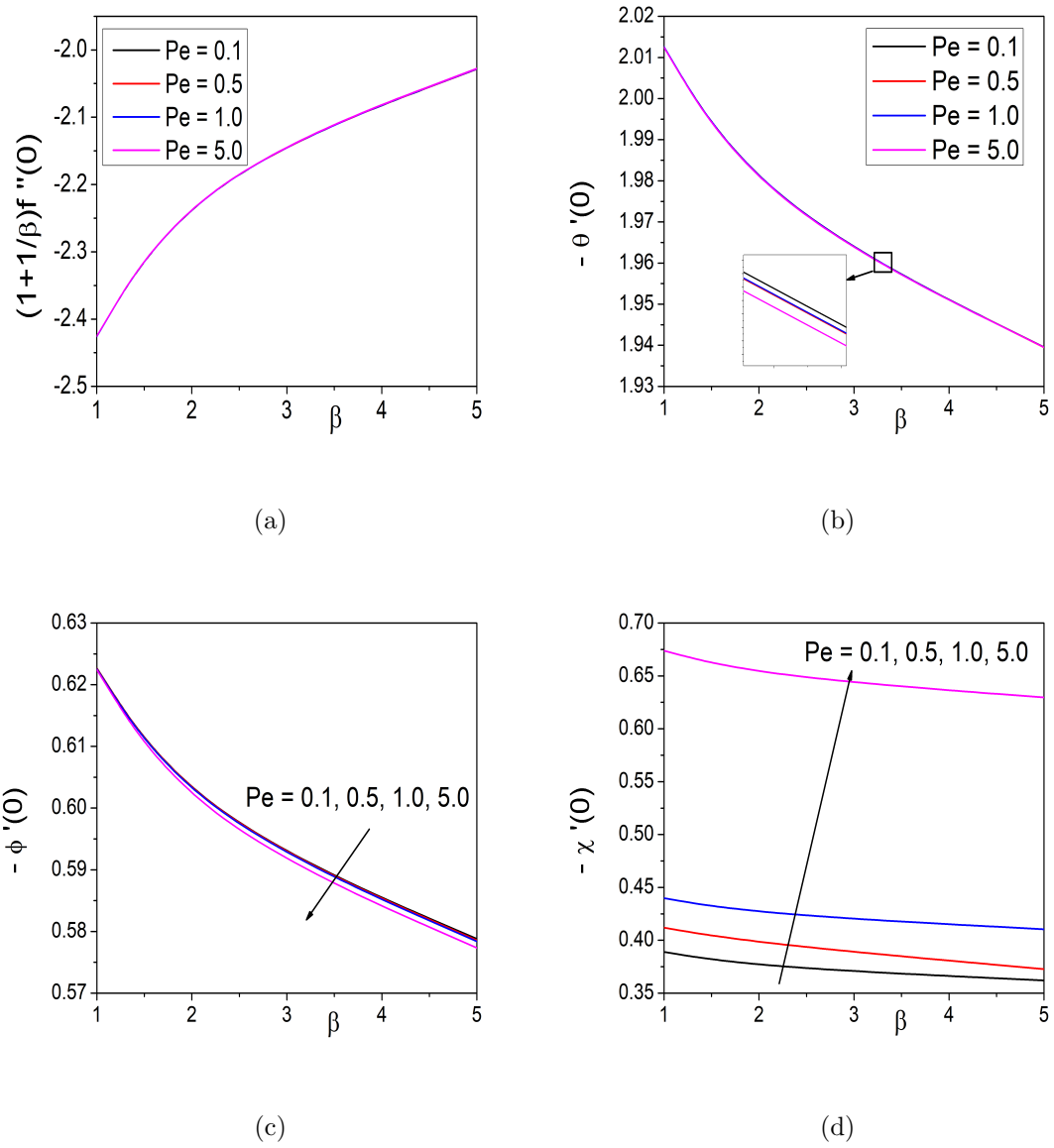

Figure 4.4: "Plot of $f''(0)$, $-\theta'(0)$, $-\phi'(0)$ and $-\chi'(0)$ for various values of the Peclet number P_e."

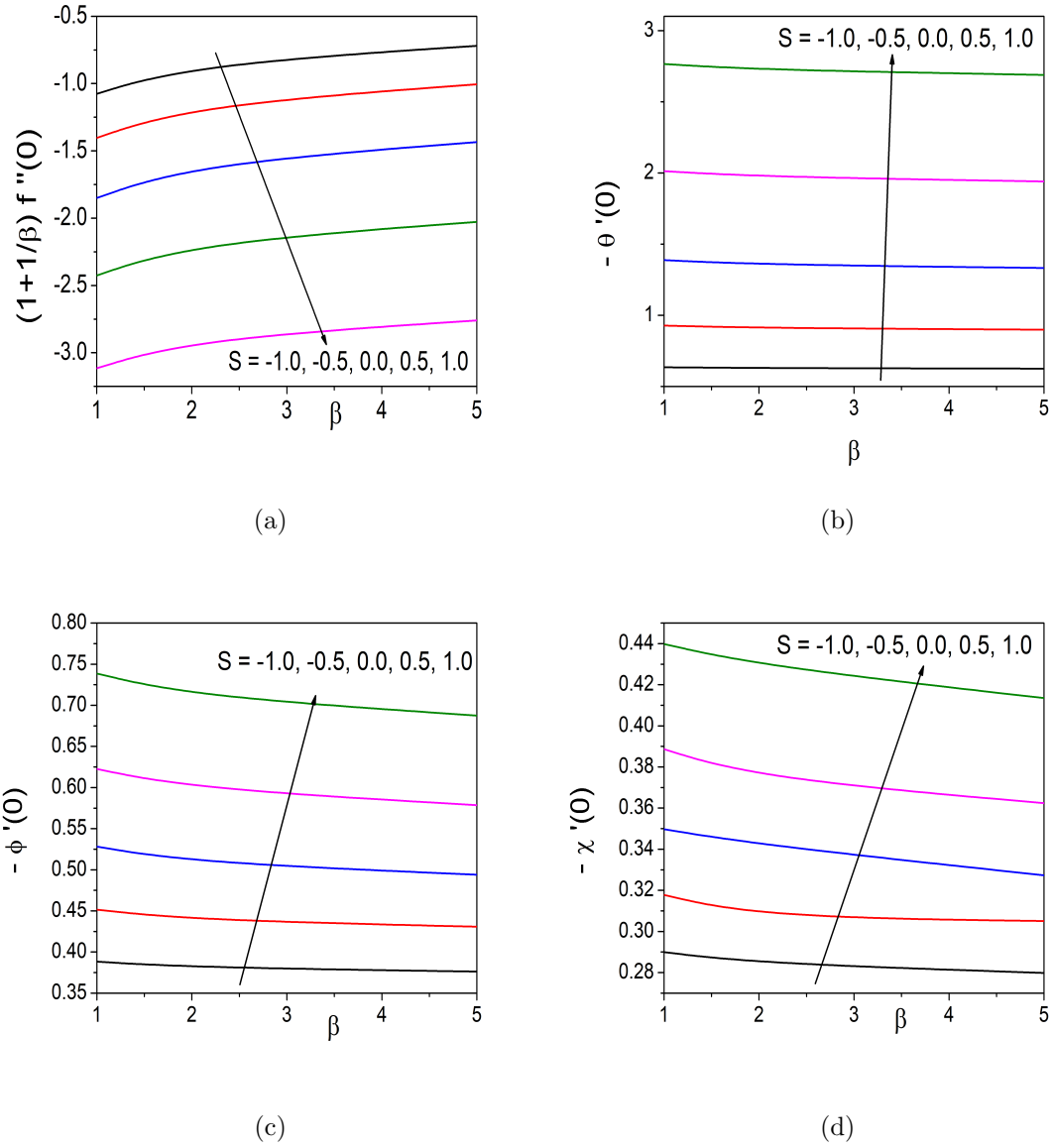

(a) (b)

(c) (d)

Figure 4.5: "Plot of $f''(0)$, $-\theta'(0)$, $-\phi'(0)$ and $-\chi'(0)$ for various values of the suction / injection parameter S."

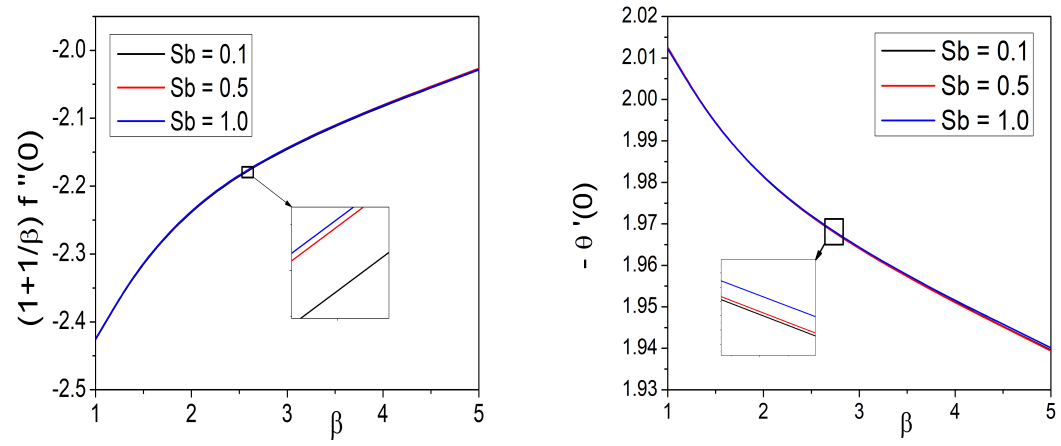

(a)

(b)

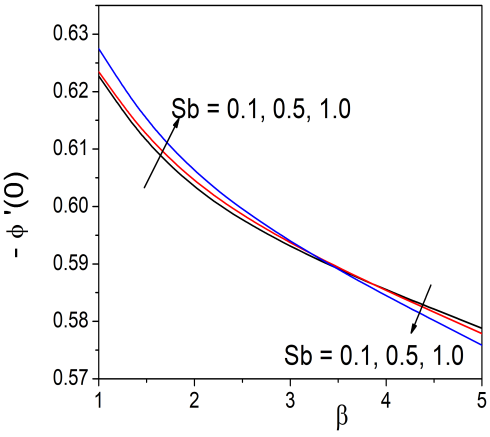

(c)

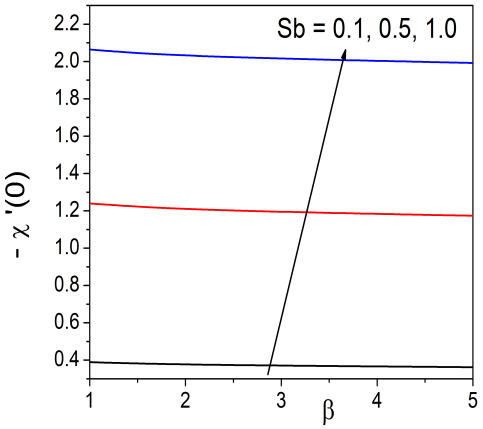

(d)

Figure 4.6: "Plot of $f''(0)$, $-\theta'(0)$, $-\phi'(0)$ and $-\chi'(0)$ for various values of the bioconvection Schmidth number Sb."

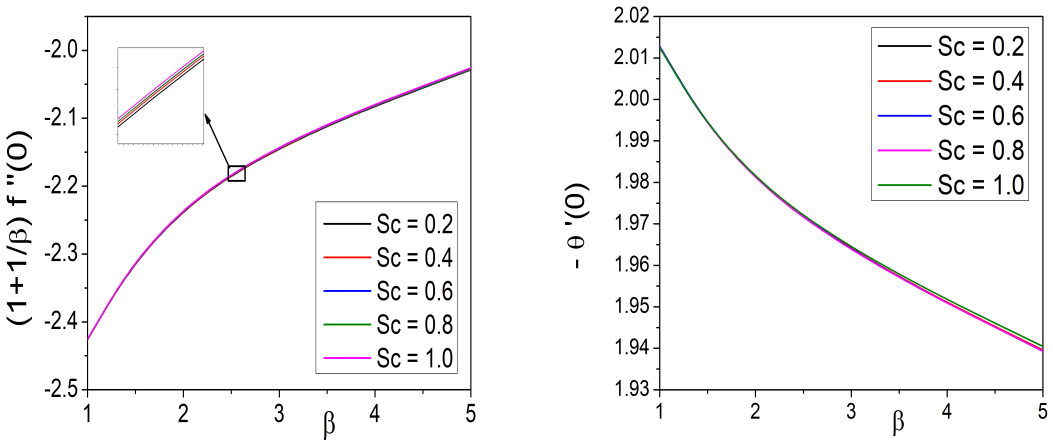

(a)

(b)

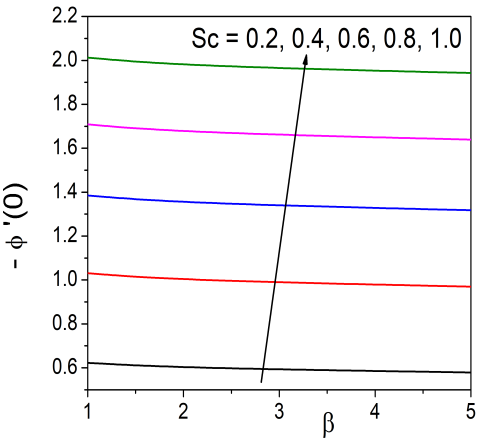

(c)

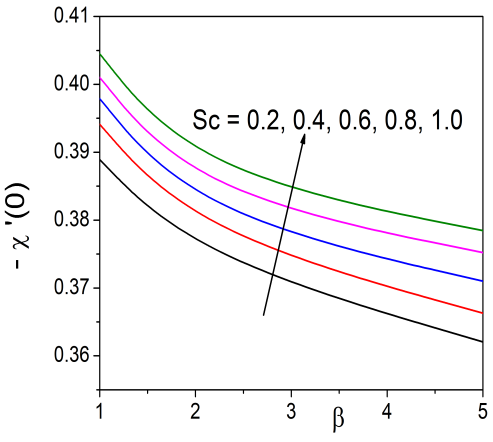

(d)

Figure 4.7: "Plot of $f''(0)$, $-\theta'(0)$, $-\phi'(0)$ and $-\chi'(0)$ for various values of the Schmidth number Sc."

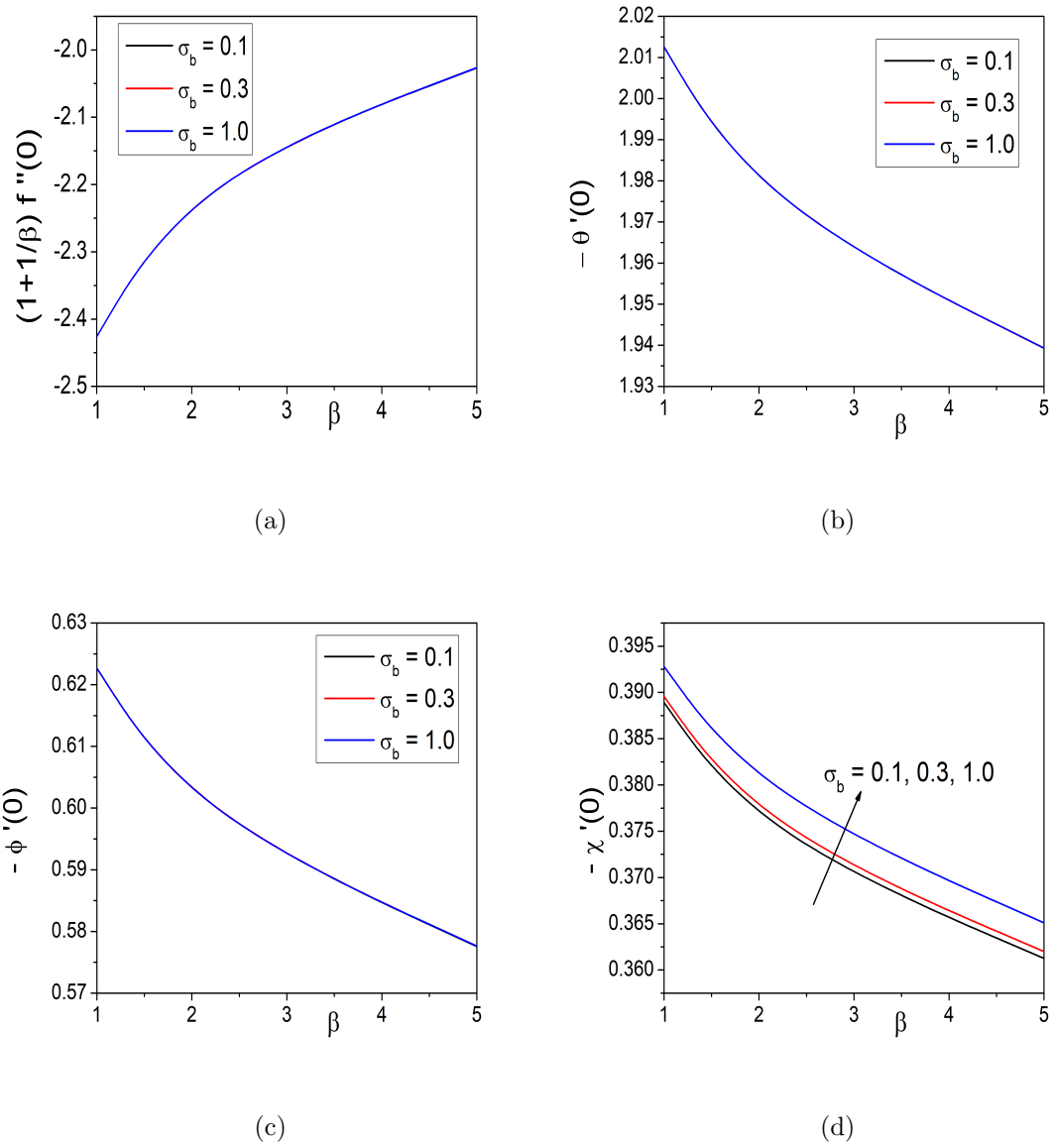

Figure 4.8: "Plot of $f''(0)$, $-\theta'(0)$, $-\phi'(0)$ and $-\chi'(0)$ for various values of the dimensionless bioconvection constant σ_b."

Chapter 5

Simultaneous Effects of Chemical Reaction and Magnetic Field on Entropy Generation in a Casson Fluid Flow Over a Radially Stretching Sheet: A Neural Network based Analysis [1]

5.1 Introduction

Second law of thermodynamics states that, all flow and heat transfer processes experience irreversible modifications. The energy losses during the processes are often responsible for these irreversible modifications. Although actions can be taken to mitigate these irreversible impacts, recovering all of the lost energy is difficult. The entropy of the system increases as a result of this process. As a result, the entropy production rate has become a common metric

[1] Communicated to "**Mathematical Methods in the Applied Sciences**"

for studying irreversibility impacts. The entropy generation in most industrial and technical phenomena results in the destruction of the available energy of the system. The entropy generation has a significant impact on the functioning of thermal equipment such as heat engines, power plants, heat pumps, refrigerators, and air conditioners.Hence, determining the rate of entropy generated for a system is critical in order to maximise the energy in the system for efficient operation. This aspect was proposed by Bejan[11, 12]. Many studies on the applicability of the second law of thermodynamics and entropy generation have been published in the literature. Sreenadh*et al.* [89] presented a numerical analysis treatment for entropy generation over MHD Jeffrey fluid flow across a non-linear radially expanded sheet. The influences of entropy production and Hall current on MHD Casson fluid across a stretched surface with velocity slip factor have been quantitatively investigated by El-Aziz *et al.* [1]. Narla*et al.* [56] analyzed the effect of magnetic filed on the entropy generation in an incompressible viscous fluid flow past a curved stretching surface.

In this chapter the impacts of magnetic field and chemical reaction on the entropy generation in an unsteady Casson fluid flow due to radially extending sheet are investigated.

5.2 Formulation of the Problem

Consider a two dimensional unsteady, laminar flow of a Casson fluid over a radially stretched surface at z = 0 as shown in Figure. 2.1. The stretching velocity of the surface in the radial direction is $U_w = \dfrac{ar}{1-ct}$, where $a > 0$.

The equations describing the flow are given by

$$\frac{\partial u}{\partial r} + \frac{u}{r} + \frac{\partial w}{\partial z} = 0 \tag{5.1}$$

$$\frac{\partial u}{\partial t} + u\frac{\partial u}{\partial r} + w\frac{\partial u}{\partial z} = \nu(1 + \frac{1}{\beta})\frac{\partial^2 u}{\partial z^2} - \frac{\sigma\, B_0^2}{\rho}u \tag{5.2}$$

$$\frac{\partial T}{\partial t} + u\frac{\partial T}{\partial r} + w\frac{\partial T}{\partial z} = \frac{k}{\rho c_p}\frac{\partial^2 T}{\partial z^2} \tag{5.3}$$

$$\frac{\partial C}{\partial t} + u\frac{\partial C}{\partial r} + w\frac{\partial C}{\partial z} = D_S\frac{\partial^2 C}{\partial z^2} + k_1(C - C_\infty) \tag{5.4}$$

The boundary conditions are as follows:

$$\left.\begin{aligned} &u = U_w,\, w = 0,\, T = T_w = T_\infty + \frac{br}{1-ct},\, C = C_w = C_\infty + \frac{br}{1-ct} \quad at \quad z = 0 \\ &u \to 0, \quad T \to T_\infty, \quad C \to C_\infty \qquad as \quad z \to \infty \end{aligned}\right\} \tag{5.5}$$

where B_0 is applied magnetic field, k_1 is the chemical reaction rate. The remaining quantities are defined in the previous chapters.

Introducing the stream function $\psi(r,z)$ through $u = -\frac{1}{r}\frac{\partial \psi}{\partial z}$ and $w = \frac{1}{r}\frac{\partial \psi}{\partial r}$ and the following similarity transformations

$$\begin{aligned} &\eta = \frac{z}{r}\mathrm{Re}^{1/2}, \quad \psi(r,z) = -r^2 U_w \mathrm{Re}^{-1/2} f(\eta) \\ &T - T_\infty = T_w - T_\infty\theta(\eta) \quad \text{and} \quad C - C_\infty = C_w - C_\infty\phi(\eta) \end{aligned} \tag{5.6}$$

Putting Eq, (5.6) in Eqs. (5.1) - (5.4), we obtain

$$(1 + \frac{1}{\beta})f''' + 2ff'' - (f')^2 - A(f' + \frac{\eta}{2}f'') - Mf' = 0 \tag{5.7}$$

$$\frac{1}{\mathrm{Pr}}\theta'' + 2f\theta' - f'\theta - A(\theta + \frac{\eta}{2}\theta') = 0 \tag{5.8}$$

$$\frac{1}{Sc}\phi'' + 2f\phi' - f'\phi - A(\phi + \frac{\eta}{2}\phi') - K_r\phi = 0 \tag{5.9}$$

The boundary conditions given in Eq. (5.5) are transformed into the following form:

$$\begin{aligned} &f(\eta) = 0, \quad f'(\eta) = 1, \quad \theta(\eta) = 1, \quad \phi(\eta) = 1 \quad \text{at} \quad \eta = 0 \\ &f'(\eta) \to 0, \quad \theta(\eta) \to 0 \quad , \phi(\eta) \to 0 \quad \text{as} \quad \eta \to \infty \end{aligned} \tag{5.10}$$

where $M = \frac{\sigma B_0^2}{\rho}\left(\frac{1-ct}{a}\right)$ is the magnetic parameter, $K_r = \frac{k_1(1-ct)}{a}$ is the chemical reaction parameter.

The non-diemaional form of the skin friction coefficient C_f, the Nusselt number N_u and the Sherwood number $Sh.$ hanged to the following form:

$$\frac{1}{2}\sqrt{Re}C_f = (1+\frac{1}{\beta})f''(0),\ \frac{N_u}{\sqrt{Re}} = -\theta'(0)\, and\, \frac{Sh}{\sqrt{Re}} = -\phi'(0) \tag{5.11}$$

5.3 Entropy generation

The investigation of entropy generation is essential for understanding the irreversibility of thermal energy in a certain system. As per the second law of thermodynamics the relation for the entropy generation of the scheme associated with unsteady Casson fluid flow across the radially stretched sheet in the presence of a magnetic field and chemical reaction is given by.

$$S_G = \frac{k}{T_\infty^2}\left(\frac{\partial T}{\partial z}\right)^2 + \frac{\mu}{T_\infty}\left(1+\frac{1}{\beta}\right)\left(\frac{\partial u}{\partial z}\right)^2 + \frac{\sigma\, B_0^2}{T_\infty}u^2 + \frac{\mu}{C_\infty}\left(\frac{\partial C}{\partial z}\right)^2 + \frac{\mu}{C_\infty}\left(\frac{\partial T}{\partial z}\right)\left(\frac{\partial C}{\partial z}\right) \tag{5.12}$$

The first term in the above expression reflects the entropy effect due to heat transfer, the second term denotes the entropy effect due to fluid friction, the third term symbolises the entropy impact caused by the magnetic field, the fourth term represents the entropy effect due to pure concentration gradient, and the fifth term represents the entropy effect due to the mixed product of concentration and thermal gradients.

In terms of dimensionless variables the entropy generation ha sthe form

$$Ns = \mathrm{Re}\left[(\theta')^2 + \frac{Br}{\Omega}\left(1+\frac{1}{\beta}\right)(f'')^2 + \frac{Br}{\Omega}M(f')^2 + \lambda\Big(\frac{\varsigma}{\Omega}\Big)^2(\phi')^2 + \lambda\Big(\frac{\varsigma}{\Omega}\Big)\theta'\phi'\right] \tag{5.13}$$

where $Ns = \frac{S_G r^2 T_\infty^2}{k(T_w - T_\infty)^2}$ is the dimensionless entropy generation number, $Br = \frac{\mu U_w^2}{k(T_w - T_\infty)}$ is the Brinkman number, $\Omega = \frac{T_w - T_\infty}{T_\infty}$ is the dimensionless temperature, $\varsigma = \frac{C_w - C_\infty}{C_\infty}$ is the dimensionless concentration and $\lambda = \frac{C_\infty}{k}$ is the diffusive constant parameter.

5.4 Method of Solution

Consider a multilayered perceptron consisting of 3 – layers namely input layer - consisting of 'n' inputs $\bar{\eta}$=$(\eta_1, \eta_2, ...\eta_n)$, hidden layer consisting of 'k' neurons and output layer consisting of 3 – neurons $N_1(\eta_i, P_1)$, $N_2(\eta_i, P_2)$ and $N_3(\eta_i, P_3)$ to estimate the solutions of three coupled ordinary differential equations as shown in the Fig.5.1.

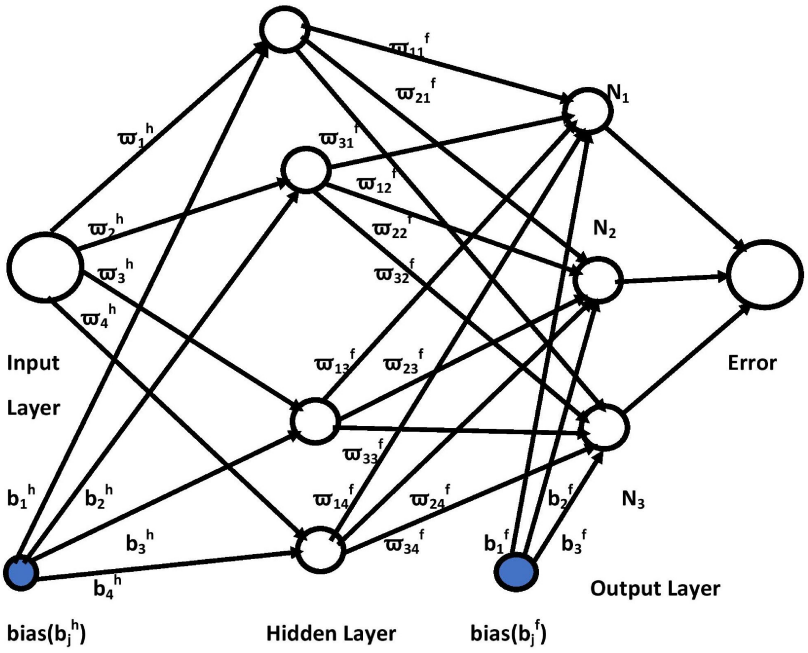

Figure 5.1: "Feed Forward Neural Network."

The trial solutions for f,θ and ϕ respectively with the adjustable parameters P_1, P_2 and P_3, which are given by the following expressions

$$\left.\begin{aligned} N_1(\eta_i, P_1) &= \sum_{j=1}^{k} \varpi_{1j}^f \sigma\{\varpi_j^h \eta_i + b_j^h\} + b_1^f \\ N_2(\eta_i, P_2) &= \sum_{j=1}^{k} \varpi_{2j}^f \sigma\{\varpi_j^h \eta_i + b_j^h\} + b_2^f \\ N_3(\eta_i, P_3) &= \sum_{j=1}^{k} \varpi_{3j}^f \sigma\{\varpi_j^h \eta_i + b_j^h\} + b_3^f \end{aligned}\right\} \tag{5.14}$$

where, σ is the sigmoid activation function, ϖ_j^h represents the weights from the input layer to the j^{th} hidden neuron, b_j^h is the bias term in the hidden layer, ϖ_{1j}^f, ϖ_{2j}^f, ϖ_{3j}^f are the weights from the j^{th} hidden neuron to the first, second and third output neurons respectively, b_1^f, b_2^f, b_3^f are the bias terms in the output layer, P_i corresponds to the parameters ϖ_j^h, b_j^h, ϖ_{ij}^f, b_i^f for $i = 1, 2, 3$. Since no data has been collected to learn from the differential equation, we have to insert Eq. (5.14) in the differential equations Eq. (5.7) - Eq. (5.9). Hence, we get

$$\begin{aligned} E_f = (1 + \frac{1}{\beta}){N_1}'''(\eta_i, P_1) + 2N_1(\eta_i, P_1){N_1}''(\eta_i, P_1) - \left({N_1}'(\eta_i, P_1)\right)^2 - A({N_1}'(\eta_i, P_1) \\ + \frac{\eta_i}{2}{N_1}''(\eta_i, P_1)) - M(({N_1}'(\eta_i, P_1))) \end{aligned} \tag{5.15}$$

$$\begin{aligned} E_\theta = \frac{1}{Pr}{N_2}''(\eta_i, P_2) + 2N_1(\eta_i, P_1){N_2}'(\eta_i, P_2) - {N_1}'(\eta_i, P_1)N_2(\eta_i, P_2) - A(N_2(\eta_i, P_2) \\ + \frac{\eta_i}{2}{N_2}'(\eta_i, P_2)) \end{aligned} \tag{5.16}$$

$$\begin{aligned} E_\phi = \frac{1}{Sc}{N_3}''(\eta_i, P_3) + 2N_1(\eta_i, P_1){N_3}'(\eta_i, P_3) - {N_1}'(\eta_i, P_1)N_3(\eta_i, P_3) - A(N_3(\eta_i, P_3) \\ + \frac{\eta_i}{2}{N_3}'(\eta_i, P_3)) - K_r((N_3(\eta_i, P_3))) \end{aligned} \tag{5.17}$$

where E_f, E_θ and E_ϕ represents the errors with repsect to the equations Eq. (5.7) - Eq. (5.9) respectively. If the trial/constructed solutions for f, θ and ϕ given in Eq. (5.14) are close to exact solution then the errors E_f, E_θ and E_ϕ tend to zero.

Similarly, the errors in the boundary conditions are given by:

$$\left.\begin{aligned} &N_1(\eta_1, P_1) = 0;\ N_1'(\eta_1, P_1) = 1; N_1'(\eta_n, P_1) = 0 \\ &N_2(\eta_1, P_2) = 1;\ N_2(\eta_n, P_2) = 0 \\ &N_3(\eta_1, P_3) = 1;\ N_3(\eta_n, P_3) = 0 \end{aligned}\right\} \tag{5.18}$$

The mean square of error (MSE) is calculated by taking $1/n$ times the sum of the squared errors of differential equations (Eqs. (5.15) - (5.17)) along with the error in the boundary conditions Eqs. (5.18) on the training set and then minimized. The solution produced by determining a set of biases and weights that minimizes the MSE (or loss function) after training is the final solution of the problem. Hence, the MSE or loss function $\mathfrak{E}(P_1, P_2, P_3)$

is given by

$$\mathfrak{E}(P_1, P_2, P_3) = \frac{1}{n}\sum_{i=1}^{n} (E_f)^2 + (E_\theta)^2 + (E_\phi)^2 + [N_1(\eta_1, P_1)]^2 + [N_1'(\eta_1, P_1) - 1]^2$$
$$+ [N_2(\eta_1, P_2) - 1]^2 + [N_3(\eta_1, P_3) - 1]^2 + [N_1'(\eta_n, P_1)]^2 + [N_2(\eta_n, P_2)]^2 + [N_3(\eta_n, P_3)]^2 \tag{5.19}$$

where 4^{th} - 10^{th} terms in the above expression represents the sum of squares of the boundary conditions.

The problem is to minimize $\mathfrak{E}(P_1, P_2, P_3)$ by optimizing the biases and weights in the network for a given network configuration. The derivatives of the network output with respect to its input must be calculated in order to compute the error function $\mathfrak{E}(P_1, P_2, P_3)$. The derivatives of networks output $N_1(\eta_i, P_1)$, $N_2(\eta_i, P_2)$ and $N_3(\eta_i, P_3)$ with respect to input vector η_i are calculated using Python package called autograd. Backpropagation can then be used to pursue the optimization by evaluating the derivatives of the loss function with respect to the network parameters. Here in this paper, we used a single hidden layer, Sigmoid activation function, the Adam optimizer [38] with an initial learning rate of 0.01.

To apply this method the semi-infinite domain of the given problem i.e. $[0, \infty]$ is reduced to $[\eta_1, \eta_\infty]$, where $\eta_1 = 0$ and η_∞ is the parameter used to recover the boundary conditions at infinity. We start with training points that are chosen from the domain of the given problem i.e. $[0, \eta_\infty = 10]$ and the weights and bias terms, which are generated randomly and we train the model to modify the parameters in the given domain of the problem.To ensure that the boundary conditions in the loss are integrated into each network parameter update, we use the entire set of training points. In general, we find that a single hidden layer with a small number of units is enough to get very exact results.

To check the convergence of the solution of the method, the dimensionless coefficient of skin friction ($f''(0)$), rate of heat transfer ($\theta'(0)$) and Sherwood number ($\phi'(0)$) at the surface for $\beta = 1.0$,$Kr = 0.2$,$A = 0.5$,$M = 1.0$,$Pr = 1.0$,$Sc = 1.0$,$Re = 1.0$,$\frac{Br}{\Omega} = 1.0$,$\frac{\varsigma}{\Omega} = 3.0$ and $\lambda = 1.0$ are calculated by choosing different number of training points 50, 100, 200 and 300 and different number of neurons 5, 8, 10 and 15 in the hidden layer and the computed results

are presented in the Tables 5.1 and 5.2. It is evident from the Tables 5.1 and 5.2 that the solution has convergence of 10^{-4} when the Data points are 50 and Hidden neurons are 8.

Number Of Data points	$f''(0)$	$\theta'(0)$	$\phi'(0)$
50	-1.164716	-1.339806	-1.421653
100	-1.164554	-1.339291	-1.421721
200	-1.164511	-1.339268	-1.421674
300	-1.164501	-1.339257	-1.421662

Table 5.1: "Convergence analysis for the values of skin friction coefficient, Nusselt number and Sherwood number at the surface for $\beta = 1.0, Kr = 0.2, A = 0.5, M = 1.0, Pr = 1.0, Sc = 1.0, Re = 1.0, \frac{Br}{\Omega} = 1.0, \frac{\varsigma}{\Omega} = 3.0$ and $\lambda = 1.0$ by the present method with different number of Data points."

Number Of Neurons	$f''(0)$	$\theta'(0)$	$\phi'(0)$
5	-1.165003	-1.339354	-1.421679
8	-1.164716	-1.339806	-1.421653
10	-1.165275	-1.339176	-1.421472
15	-1.165394	-1.338839	-1.421543

Table 5.2: "Convergence analysis for the values of skin friction coefficient, Nusselt number and Sherwood number at the surface for $\beta = 1.0, Kr = 0.2, A = 0.5, M = 1.0, Pr = 1.0, Sc = 1.0, Re = 1.0, \frac{Br}{\Omega} = 1.0, \frac{\varsigma}{\Omega} = 3.0$ and $\lambda = 1.0$ by the present method with different number of Hidden neurons."

5.5 Computational Results and Discussion

The ANN approach's efficacy is demonstrated by comparing the present numerical findings for skin friction coefficient, rate of heat transfer coefficient, and concentration gradient to the values obtained utilising shooting method in association with the Runge-Kutta fourth order method for $\beta = 1.0, Kr = 0.2, A = 0.5, M = 1.0, Pr = 1.0, Sc = 1.0, Re = 1.0$, $\frac{Br}{\Omega} = 1.0, \frac{\varsigma}{\Omega} = 3.0$ and $\lambda = 1.0$.

Fig.5.2 illustrates the plot of error (between ANN method and Shooting technique results) in the values of f', θ and ϕ for 11 equispaced positions in $[0, 10]$. The findings acquired by the

	Present method	Shooting method	Relative error
$f''(0)$	-1.164716	-1.16448329	1.99×10^{-4}
$\theta'(0)$	-1.339806	-1.33919406	4.56×10^{-4}
$\phi'(0)$	-1.421653	-1.42161008	3.02×10^{-5}

Table 5.3: "Comparative analysis for the values of $f''(0)$, $\theta'(0)$, $(\phi'(0))$ and $(\chi'(0))$at the surface by the present method with the results of Shooting method for $A = 0.5$, $S = 0.5$, $Pr = 1.0$, $Sc = 0.2$, $Sb = 0.1$, $P_e = 0.1$ and $\sigma_b = 0.1$."

current approach are in excellent agreement with those obtained by the Shooting method, as shown in Fig.5.2.

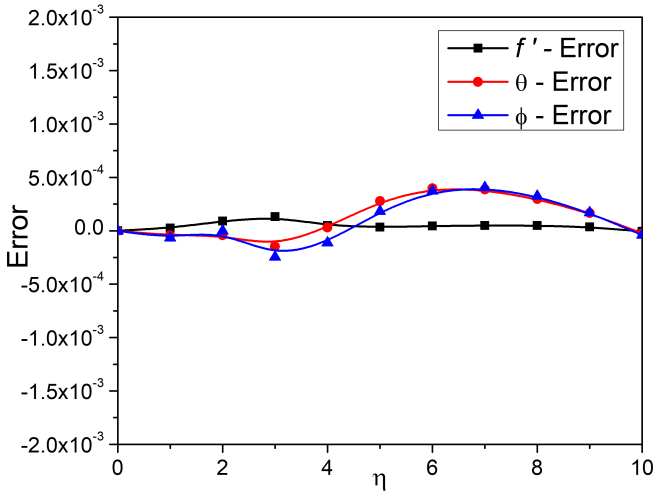

Figure 5.2: "Error plot between the results obtained by Artificial Neural Network method and Shooting method for the values of velocity, temperature and concentration profiles."

Fig. 5.3 displays the impact of the unsteadiness parameter A on the Entropy generation (Ns), skin friction coefficient $(f''(0))$, Nusselt number $(-\theta'(0))$ and Sherwood number $(-\phi'(0))$. Fig. 5.3(a) shows that Entropy generation is increasing initially and then there is a decrement in it for the increasing values of A. Fig. 5.3(b) demonstrates that skin friction is decreasing for increasing values of A. It is observed from Figures 5.3(c)–5.3(d) that both the Nusselt number and Sherwood number are increasing with the increasing values of A.

Fig. 5.4 displays the effect of magnetic parameter M on Ns, $f''(0)$,$-\theta'(0)$ and $-\phi'(0)$.

Fig. 5.4(a) reveals that Entropy Generation is increasing initially and then there is a decrement for increasing values of magnetic parameter. Fig. 5.4(b)-5.4(d) shows that skin friction, Nusselt number and Sherwood number are decreasing for increasing values of magnetic parameter.

Figure 5.5(a) reveals that Entropy Generation is increasing initially and then there is a decrement for enahancing values of chemical reaction parameter. Fig. 5.5(b) shows that skin friction coefficient is decreasing initially and increasing later for the rising values of chemical reaction parameter. Also from figures 5.5(c) and 5.5(d) it is observed that Nusselt number is decreasing and Sherwood number is increasing for the increasing values of chemical reaction parameter.

Fig. 5.6 reveals how the entropy generation has been effected by Casson fluid parameter β, Reynolds number Re, Brinkman number $\frac{Br}{\Omega}$ and dimensionless concentration $\frac{\varsigma}{\Omega}$. As the values of Brinkman number, dimensionless concentration, Reynolds number increase entropy generation is increasing, whereas entropy generation is decreasing for the increasing values if Casson fluid parameter.

5.6 Conclusions

The analysis of entropy generation in the flow of a Casson fluid across a radially stretched sheet in the presence of magnetic and chemical reaction effects using an Artificial Neural Network technique is presented. The influences of the parameters β, Kr, A, M, Pr, Sc, Re, $\frac{Br}{\Omega}$, $\frac{\varsigma}{\Omega}$ and λ on the relevant physical quantities are investigated. The important findings are presented below:

- For rising levels of the unsteadiness parameter, magnetic parameter, and chemical reaction parameter, entropy production increases first and eventually decreases.
- Skin friction decreases with rising values of the unsteadiness parameter as well as magnetic parameter, and it decreases firstly later increasing with increase in the values

of the chemical reaction parameter.

- With increasing values of the unsteadiness parameter, the Nusselt number rises, however for rising values of the magnetic and chemical reaction parameters, it diminishes.
- The concentration gradient improves as the unsteadiness and chemical reaction parameters increase, but somehow it decreases as the magnetic parameter increases.

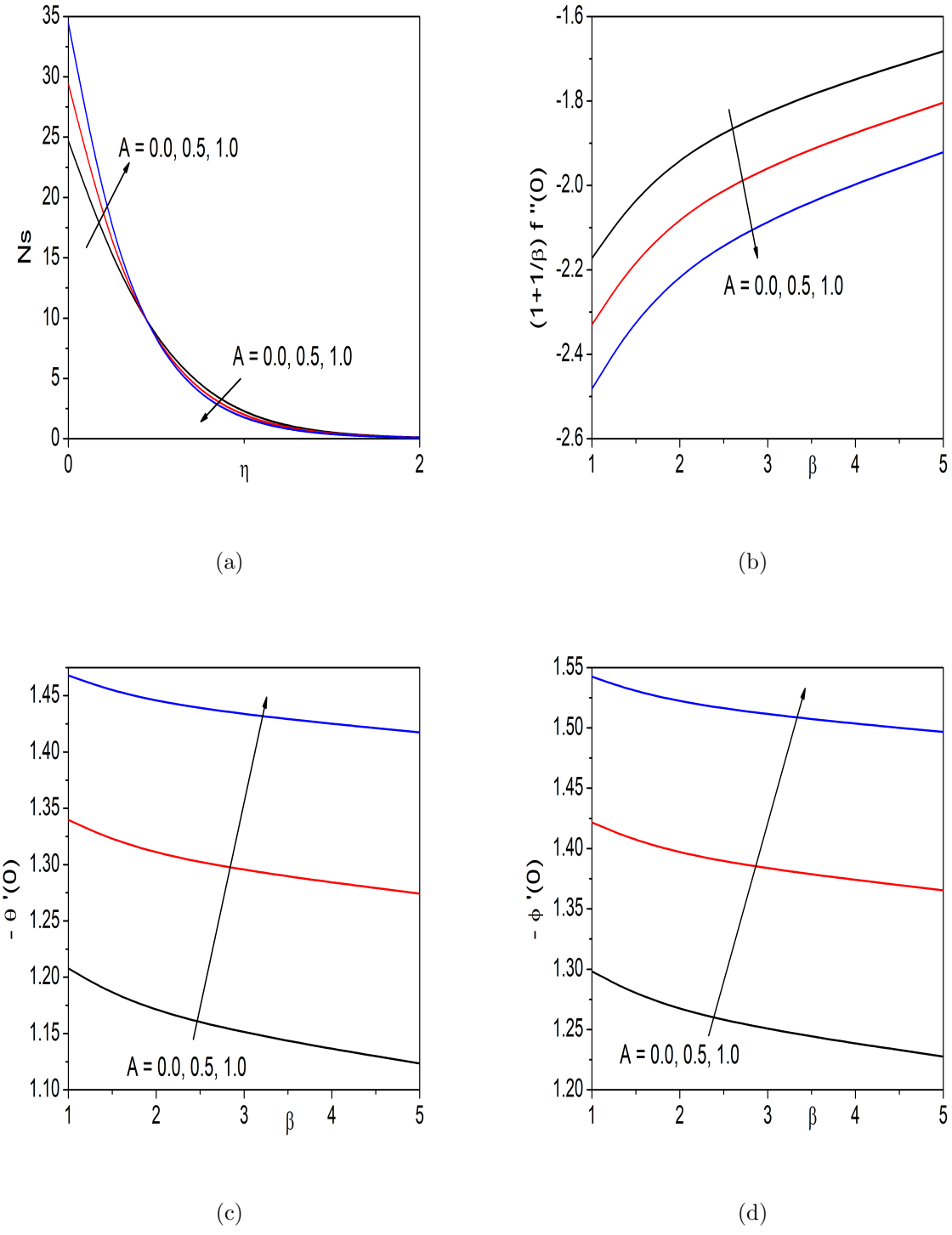

Figure 5.3: "The variation of skin friction coefficient, Nusselt number, Sherwood number and Entropy Generation with unsteadiness parameter A."

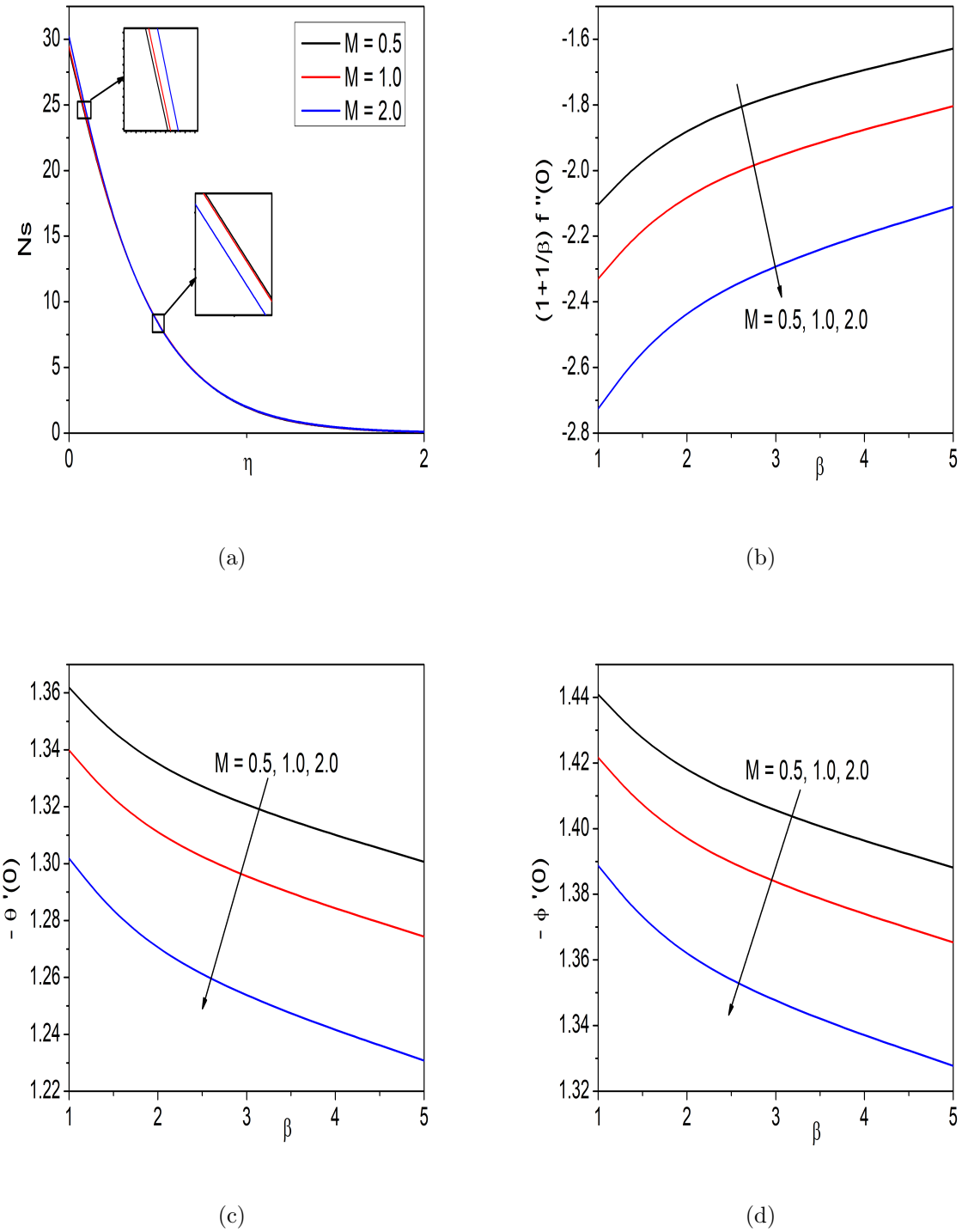

Figure 5.4: "The variation of skin friction coefficient, Nusselt number, Sherwood number and Entropy Generation with Magnetic parameter M."

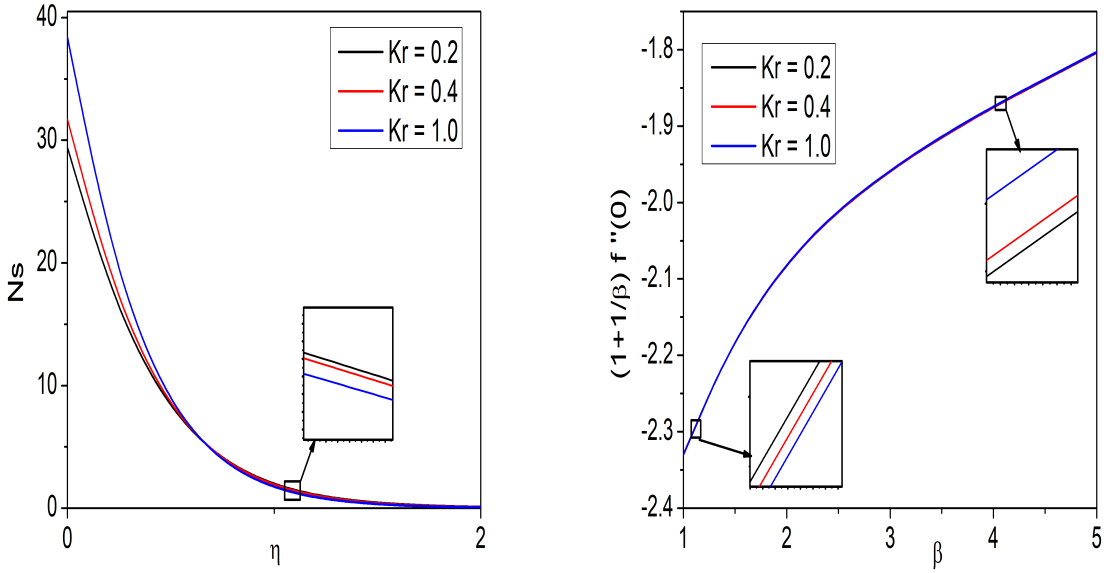

(a) (b)

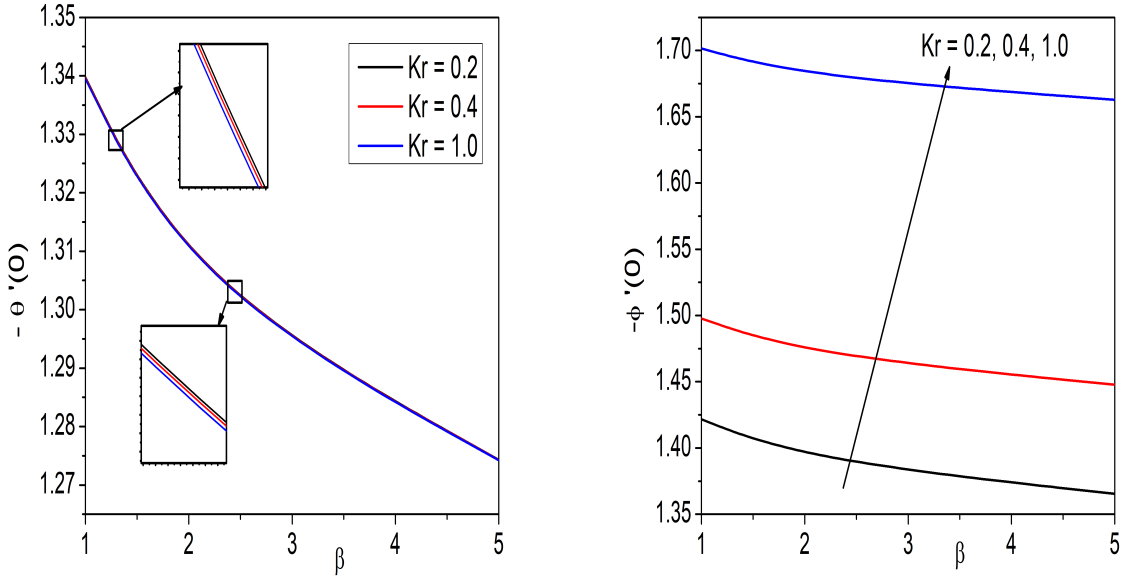

(c) (d)

Figure 5.5: "The variation of skin friction coefficient, Nusselt number, Sherwood number and Entropy Generation with chemical reaction parameter Kr."

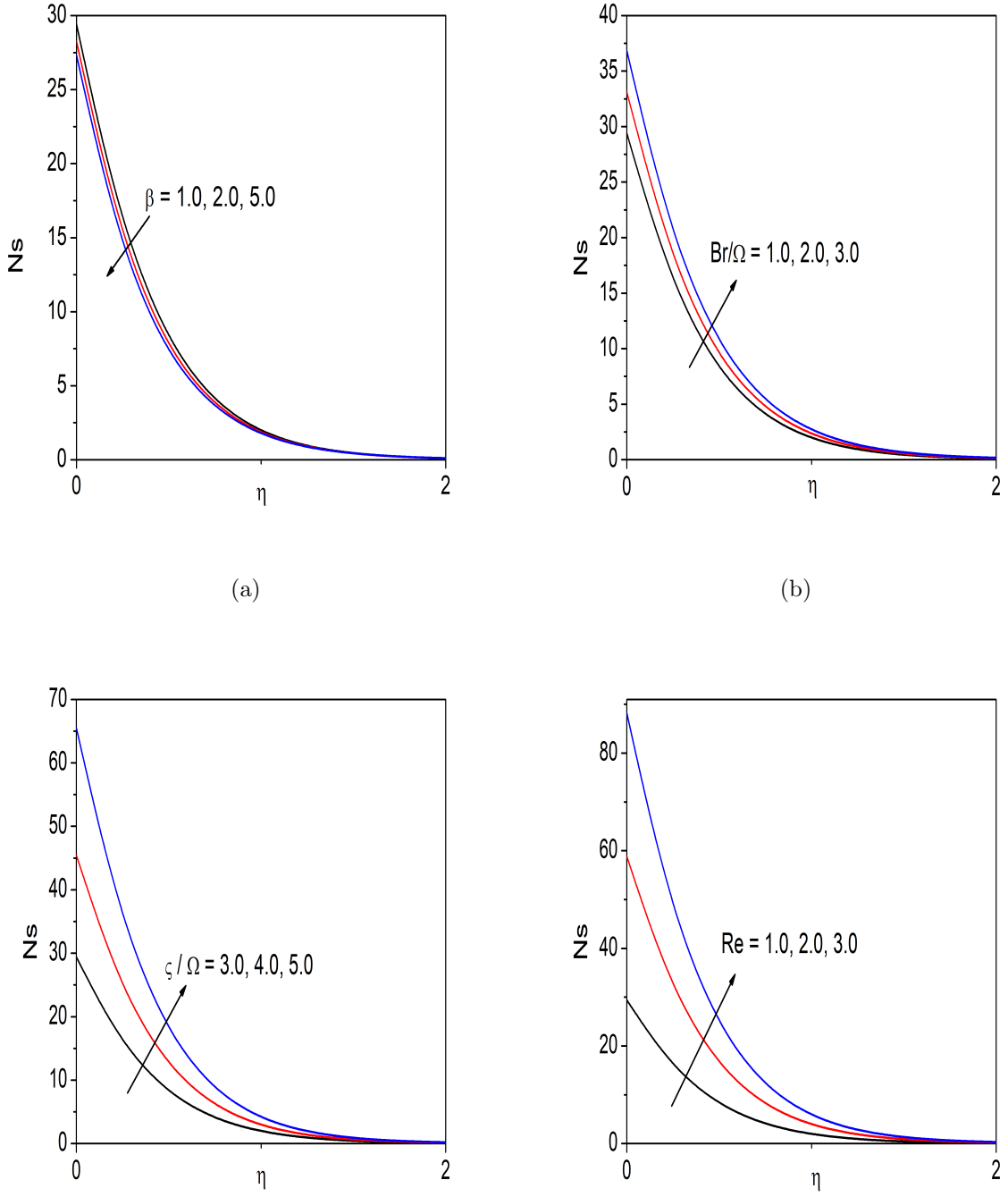

(a) (b)

(c) (d)

Figure 5.6: "The variation of Entropy Generation with β, $\frac{Br}{\Omega}$, $\frac{\varsigma}{\Omega}$ and Re."

Chapter 6

An Artificial Neural Network Solution For The Casson Fluid Flow Past a Radially Stretching Sheet with Magnetic and Radiation Effects [1]

6.1 Introduction

The effect of magnetic field on the heat transfer characteristics and fluid flow has attracted several researchers in view of its applications in many engineering problems. Several researchers, to mention a few, Ullah *et al.* [92], El-Aziz *et al.* [19], Hussanan *et al.* [32], Hamid *et al.* [24], Gireesha *et al.* [23], Renu *et al.* [17] have investigated the impacts of magnetic field on the Casson fluid flow across linear / nonlinear / radially stretching sheet.

The study of the influences of thermal radiation on convective heat and mass transport processes has grown in prominence due to its applications in nuclear power plants, steel rolling, gas turbines, design fins, aircraft, space vehicles, and satellites. Radiation within

[1] Communicated to "**Arabian Journal for Science and Engineering**"

these systems is typically caused by discharge from hot walls and operational fluid. Alkasasbeh *et al.* [6] studied the effect of thermal radiation on the stagnation-point flow of an upper-convected Maxwell Casson fluid over a stretching/shrinking sheet numerically. Mabood *et al.* [45] analyzed the impact of thermal radiation on the characteristics of melting heat transport based on MHD Casson fluid flow in a porous media. Zhou *et al.* [97] reported the impact of radiation and uniform heat source on the unsteady stagnation point flow of a Casson fluid past a permeable stretched surface.

The current chapter emphasizes the application of the ANN approach to the analysis of a steady Casson fluid flow and heat transfer across a vertical radially stretching sheet in the presence of magnetic and radiation effects.

6.2 Formulation of the problem

Consider a two-dimensional, steady Casson fluid flow over a radially stretching sheet as shown in Figure 6.1. In formulating the problem the following assumptions are made and are considered.

- A uniform magnetic field B_0 is applied normal to the flow.
- The induced magnetic field can be disregarded since the magnetic Reynolds number is so low.
- The flow phenomena generated as a result of radial stretching of sheet.
- The stretching velocity of the form $U_w = ar$, where a is stretching constant.
- Convection from the hot fluid at temperature T_w heats the sheet's surface, which is given by $T_w = T_\infty + br$. Here b is constant and T_∞ is the ambient temperature of the fluid.
- All these physiological quantities do not depend on θ because of rotational symmetry of the flow.

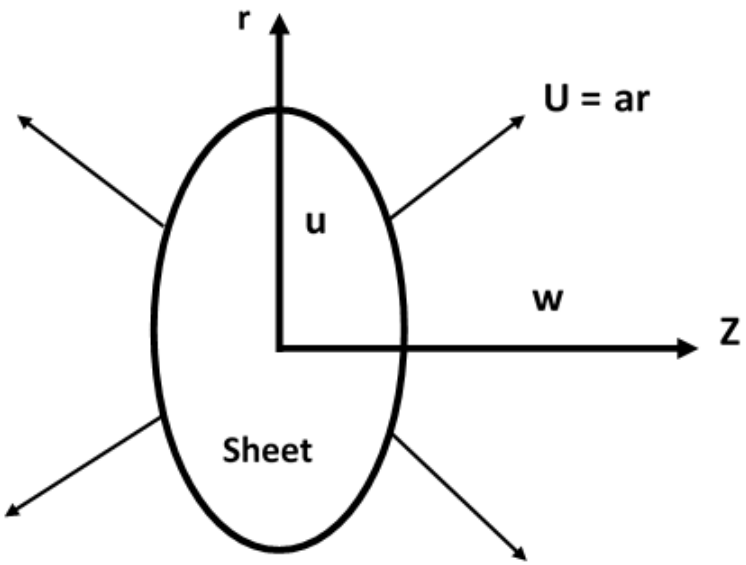

Figure 6.1: "Geometry of the problem."

With these assertions, the equations describing the flow are given by

$$\frac{\partial u}{\partial r} + \frac{u}{r} + \frac{\partial w}{\partial z} = 0 \tag{6.1}$$

$$u\frac{\partial u}{\partial r} + w\frac{\partial u}{\partial z} = \nu(1 + \frac{1}{\beta})\frac{\partial^2 u}{\partial z^2} + g\beta_T(T - T_\infty) - \frac{\sigma {B_0}^2}{\rho}u \tag{6.2}$$

$$u\frac{\partial T}{\partial r} + w\frac{\partial T}{\partial z} = \frac{k}{\rho c_p}\frac{\partial^2 T}{\partial z^2} - \frac{1}{\rho c_p}\frac{\partial q_r}{\partial z} \tag{6.3}$$

The corresponding boundary conditions are

$$\left.\begin{aligned} &u = U_w = ar; \quad w = W_0; \quad T = T_w = T_\infty + br \quad at \quad z = 0 \\ &u \to 0, \quad T \to T_\infty \quad as \quad z \to \infty \end{aligned}\right\} \tag{6.4}$$

where the radiative heat flux is represented by the quantity q_r on the right side of the temperature equation (6.3), which is given by the relation $q_r = \dfrac{-4\sigma^*}{3k^*}\dfrac{\partial T^4}{\partial z}$, where $T^4 = 4{T_\infty}^3\, T - 3{T_\infty}^4$.

In order to get dimensionless form of Eqs. (6.1) - (6.3), we introduce the ensuing trans-

formations

$$\eta = \sqrt{\frac{a}{\nu}} z \; u(r,z) = arf'(\eta), \; w(r,z) = -2\sqrt{a\nu} f(\eta), \text{ and } \theta(\eta) = \frac{T - T_\infty}{T_w - T_\infty} \tag{6.5}$$

Putting Eq (6.5),in Eqs. (6.1)-(6.3), we obtain

$$(1 + \frac{1}{\beta}) f''' + 2ff'' - (f')^2 + \lambda_T \theta - Mf' = 0 \tag{6.6}$$

$$(1 + R_d)\theta'' + Pr(2f\theta' - f'\theta) = 0 \tag{6.7}$$

The dimensionless form of boundary conditions Eq. (6.4) are

$$f(0) = S, \quad f'(0) = 1, \quad \theta(0) = 1 \quad ; f'(\infty) \to 0, \quad \theta(\infty) \to 0 \tag{6.8}$$

where $\lambda_T = \dfrac{G_r}{{R_e}^2}$ is buoyancy parameter, $G_r = g\beta_T(T_f - T_\infty)\dfrac{r^3}{\nu^2}$ is local Grashoff number, $M = \dfrac{\sigma {B_0}^2}{\rho a}$ is magnetic parameter (Hartman number) and $R_d = \dfrac{16\sigma^* {T_\infty}^3}{3kk^*}$ is radiation parameter.

In terms of dimensionless variables defined in Eq.(6.5), the skin friction coefficient C_f and the Nusselt number N_u are :

$${R_e}^{1/2} C_f = (1 + \frac{1}{\beta}) f''(0) \quad and \quad {R_e}^{-1/2} N_u = -\theta'(0) \tag{6.9}$$

6.3 Method of Solution

Consider a multilayered perceptron consisting of 3 – layers namely input layer - consisting of 'n' inputs $\bar{\eta}$=$(\eta_1, \eta_2, ...\eta_n)$, hidden layer - consisting of 'k' neurons and output layer consisting of two neurons $N_1(\eta_i, P_1)$ and $N_2(\eta_i, P_2)$ to estimate the solutions to two coupled ordinary differential equations as shown in the Fig. 6.2.

We take the network outputs $N_1(\eta_i, P_1)$ and $N_2(\eta_i, P_2)$ as the trial solution for f and θ

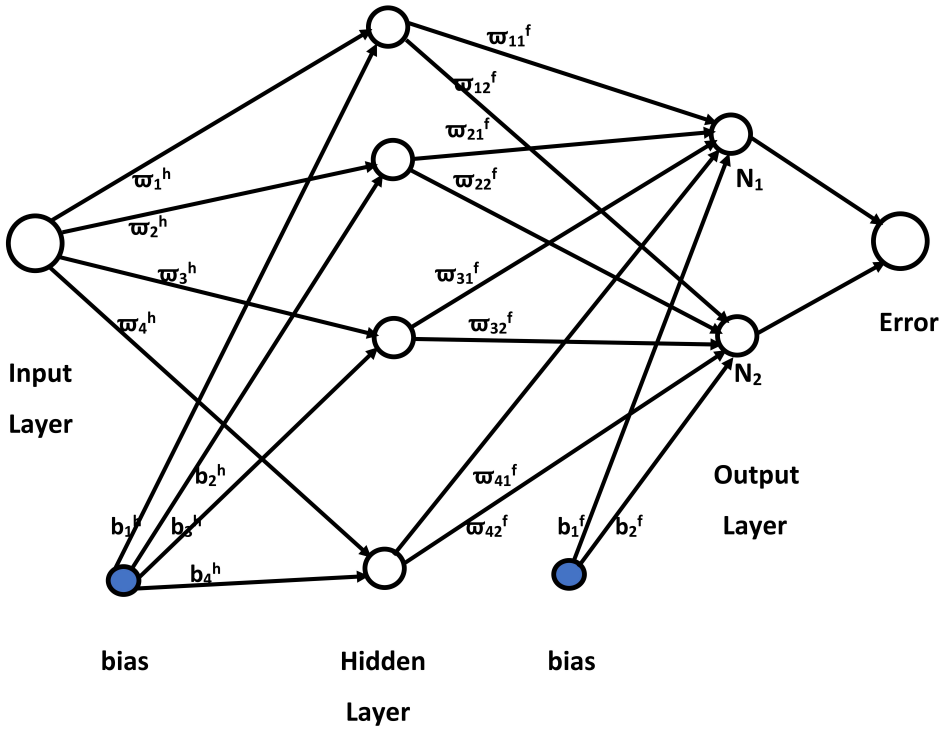

Figure 6.2: "Feed Forward Neural Network."

respectively with the adjustable parameters P_1 and P_2 respectively, which are given by the expressions

$$\left.\begin{aligned} N_1(\eta_i, P_1) &= \sum_{j=1}^{k} \varpi_{1j}^f \sigma\{\varpi_j^h \eta_i + b_j^h\} + b_1^f \\ N_2(\eta_i, P_2) &= \sum_{j=1}^{k} \varpi_{2j}^f \sigma\{\varpi_j^h \eta_i + b_j^h\} + b_2^f \end{aligned}\right\} \tag{6.10}$$

where, ϖ_j^h represents the weights from the input layer to the j^{th} hidden neuron, b_j^h is the bias term in the hidden layer, ϖ_{1j}^f is the weight from the j^{th} hidden neuron to the first output neuron, b_1^f is the bias term and ϖ_{2j}^f is the weight from the j^{th} hidden neuron to the second output neuron, b_2^f is the bias term. P_1 corresponds to the parameters ϖ_j^h, b_j^h, ϖ_{1j}^f, b_1^f and P_2 corresponds to the parameters ϖ_j^h, b_j^h, ϖ_{2j}^f and b_2^f respectively.

Since no data has been collected to learn from the differential equation, we have to insert

Eq. (6.10) in the differential equations Eq.(6.6) and Eq. (6.7). Hence, we get

$$E_f = (1+\frac{1}{\beta})N_1'''(\eta_i,P_1) + 2N_1(\eta_i,P_1)N_1''(\eta_i,P_1) - \left(N_1'(\eta_i,P_1)\right)^2 + \lambda_T N_2(\eta_i,P_2) - MN_1'(\eta_i,P_1) \tag{6.11}$$

$$E_\theta = (1+R_d)N_2''(\eta_i,P_2) + \Pr(2N_1(\eta_i,P_1)N_2'(\eta_i,P_2) - N_1'(\eta_i,P_1)N_2(\eta_i,P_2)) \tag{6.12}$$

where E_f and E_θ represents the errors or residuals with respect to the equations Eq. (6.6) and Eq. (6.7) respectively. If the trial/constructed solutions for f and θ given in Eq. (6.10) are close to exact solution then the errors E_f and E_θ tend to zero. Similarly, the errors in the boundary conditions are given by:

$$N_1(\eta_1,P_1) = S;\ N_1'(\eta_1,P_1) = 1;\ N_2(\eta_1,P_2) = 1;\ N_1'(\eta_n,P_1) = 0;\ N_2(\eta_n,P_2) = 0 \tag{6.13}$$

The mean square of error (MSE) is calculated by taking $1/n$ times the sum of the squared errors of differential equations (Eqs.(6.11) - (6.12)) along with the error in the boundary conditions Eq.(6.13) on the training set and then minimized. The solution produced by determining a set of biases and weights that minimizes the MSE (or loss function) after training is the final solution of the problem. Hence, the MSE or loss function $\mathfrak{E}(P_1,P_2)$ is given by

$$\mathfrak{E}(P_1,P_2) = \frac{1}{n}\sum_{i=1}^{n}(E_f)^2 + (E_\theta)^2 + \left[N_1(\eta_1,P_1) - S\right]^2 + \left[N_1'(\eta_1,P_1) - 1\right]^2 + \left[N_1'(\eta_n,P_1)\right]^2 + \left[N_2(\eta_1,P_2) - 1\right]^2 + \left[N_2(\eta_n,P_2)\right]^2 \tag{6.14}$$

where 3^{rd} – 7^{th} terms represent error terms corresponding to the boundary conditions.

The problem is to minimize $\mathfrak{E}(P_1,P_2)$ by optimizing the biases and weights in the network for a given network configuration. The derivatives of the network output with respect to its input must be computed in order to compute the error $\mathfrak{E}(P_1,P_2)$. The derivative of networks output $N_1(\eta_i,P_1)$ and $N_2(\eta_i,P_2)$ with respect to input vector η_i are calculated using Python package called autograd. Backpropagation can then be used to pursue the optimization by

evaluating the derivatives of the loss function with respect to the network parameters. Here in this paper, we used a single hidden layer, Sigmoid activation function, the Adam optimizer [38] with an initial learning rate of 0.01.

To apply this method the semi-infinite domain of the given problem i.e. $[0, \infty]$ is reduced to $[0, \eta_\infty]$ where η_∞ is a constant used to recover the conditions at infinity. We start with training points that are chosen from the domain of the given problem i.e. $[0, \eta_\infty]$ and the bias terms and weights, which are generated arbitrarily and train the model to modify the parameters in the given domain of the problem. An ADAM optimizer [38] with an initial learning rate of 0.01 and one hidden layer is employed here along with the a Sigmoid activation function. The entire set of training points is used to ensure that the boundary conditions in the loss function are accounted for in the updating of each network parameter. It is found that one hidden layer with a minimal number of units is adequate for getting very exact results.

To check the convergence of the solution of the method, the dimensionless coefficient of skin friction $f''(0)$ and rate of heat transfer $\theta'(0)$ at the surface for $M = 1.0$, $R_d = 0.5$, $Pr = 1.0$, $S = 0.5$, $\lambda_T = 1.0$ and $\beta = 1.0$ are calculated by choosing a different number of training points 50, 100, and 150 and a different number of neurons 5, 10, 20 and 30 in the hidden layer and the computed results are presented in the Tables 6.1 and 6.2. Tables 6.1 and 6.2 demonstrates that the solution has the convergence of 10^{-4} when the Data points are 50 and Hidden neurons are 10.

Number Of training points	$f''(0)$	$\theta'(0)$
50	-1.163898	-1.399067
100	-1.163375	-1.398469
150	-1.163726	-1.398835

Table 6.1: "Convergence table for the values of $f''(0)$ and $\theta'(0)$ for $M = 1.0$, $R_d = 0.1$, $S = 0.5$, $\lambda = 1.2$ and $\beta = 1.0$ by the present method with different number of Hidden neurons and number of Data points fixed as 50."

Number Of Neurons	$f''(0)$	$\theta'(0)$
5	-1.163186	-1.397693
10	-1.163898	-1.399067
20	-1.165101	-1.398619
30	-1.164058	-1.398811

Table 6.2: "Convergence table for the values of $f''(0)$ and $\theta'(0)$ for $M = 1.0$, $R_d = 0.1$, $S = 0.5$, $\lambda = 1.2$ and $\beta = 1.0$ by the present method with different number of Data points and number of Neurons as 10."

6.4 Computational Results and Discussion

The present study computes the Nusselt Number N_u, and the coefficient of skin friction C_f, for different parameters and depicted graphically. The Artificial Neural Network method (ANN) along with ADAM optimization is used to solve the equations 6.6 and 6.7 along with the boundary conditions 6.8. The code written is executed for different parameters in Python.

Additionally, the efficiency of the approach is confirmed by comparing the present findings of the skin friction coefficient and rate of heat transfer coefficient computed using the shooting method in conjunction with the Runge-Kutta fourth order method for $M = 1.0$, $R_d = 0.1$, $S = 0.5$, $\lambda = 1.2$ and $\beta = 1.0$. The computed results are presented in the Table 6.3. Table 6.3 demonstrate that the present results are consistent with the results obtained by using shooting method.

$f''(0)$		$\theta'(0)$	
Present method	Shooting method	Present method	Shooting method
-1.163898	-1.16399608	-1.399067	-1.39904492

Table 6.3: "Comparison of the present method with the results of Shooting method."

Fig. 6.3 illustrates the plot of error (between ANN method and Shooting technique results) in the values of $f'(\eta)$ and $\theta(\eta)$ for 11 equispaced positions in $[0, 10]$. The present method's (ANN method) conclusions are in perfect accord with those produced by Shooting method. as shown in Figure 6.3.

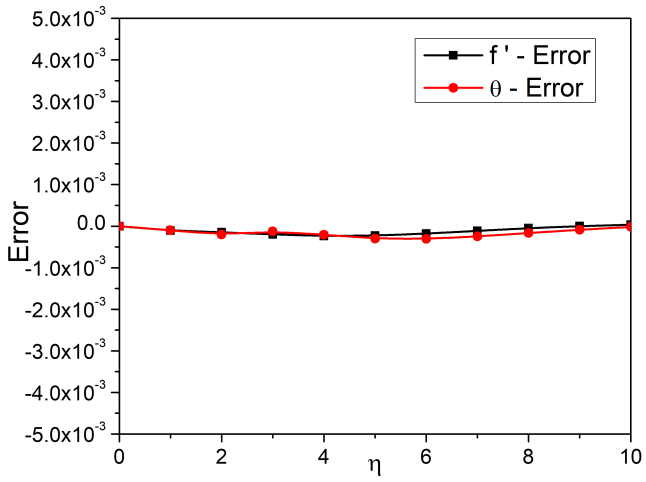

Figure 6.3: "Error plot between the results obtained by Artificial Neural Network method and Shooting method for the values of velocity and temperature profiles."

The impact of suction/injection parameter S on the velocity, temperature profile, coefficient of skin friction and rate of heat transfer for fixed values of other parameters is presented in Fig.6.4. It is observed from Figs.6.4(a) and 6.4(b) that, both the velocity and temperature are diminishing for growth in the suction/injection parameter S. It is perceived from Figs.6.4(c) and 6.4(d) that skin friction is decreasing and Nusselt number is increasing for the enhancing values of suction/injection parameter S.

The significance of the magnetic parameter M on the velocity, temperature, coefficient of skin friction and rate of heat transfer is depicted in Fig.6.5. It is clear from figures 6.5(a) and 6.5(b) that velocity is reducing and temperature is enhancing for the enhancing values of M. Figures 6.5(c) and 6.5(d) show that as M increases, skin friction and the Nusselt number decrease. This is because the Lorentz force, a drag force that tends to resist flow, is induced when there is a transverse magnetic field that is normal to the direction of the flow. This type of resistive force increases friction between the fluid's layers, which tends to delay the flow and causes the fluid to encounter resistance. The skin friction coefficient at the wall will be lessened as a result.

The variation of velocity profile, temperature profile, coefficient of skin friction and rate

of heat transfer with radiation parameter R_d is depicted in Fig.6.6. It is observed from Figs. 6.6(a) and 6.6(b) that both the velocity and temperature are increasing for the increasing values of the radiation parameter R_d. This may occur as a result of Rosseland radiation dominance, which causes the thickness of momentum and thermal boundary layers to rise. It is found from the Figs. 6.6(c) and 6.6(d) that the coefficient of skin friction and heat transfer rate are increasing as R_d is increasing. The radiative energy is proportional to the fourth power of absolute temperature and inversely proportional to emissivity on the surface. Hence, modifies the temperature even for quite small values of emissivity.

6.5 Conclusions

The primary objective of this chapter was to employ the Artificial Neural Network approach to solve coupled nonlinear differential equations emerging from the boundary layer flow of a Casson fluid over a vertical stretching sheet in the presence of magnetic and radiation effects. The influences of the parameters β, λ_T, M, Pr, R_d and S on the relevant physical quantities are investigated. The important findings are presented below.

- As the Radiation parameter rises, the skin friction enhances, but as the suction/injection parameter, magnetic parameter, buoyancy parameter, and Prandtl number increases, the skin friction declines.
- The temperature is increasing with the intensifying values of buoyancy parameter, Prandtl number, Radiation parameter and suction / injection parameter, whereas there is a decrement in temperature gradient for the increased values of magnetic parameter.

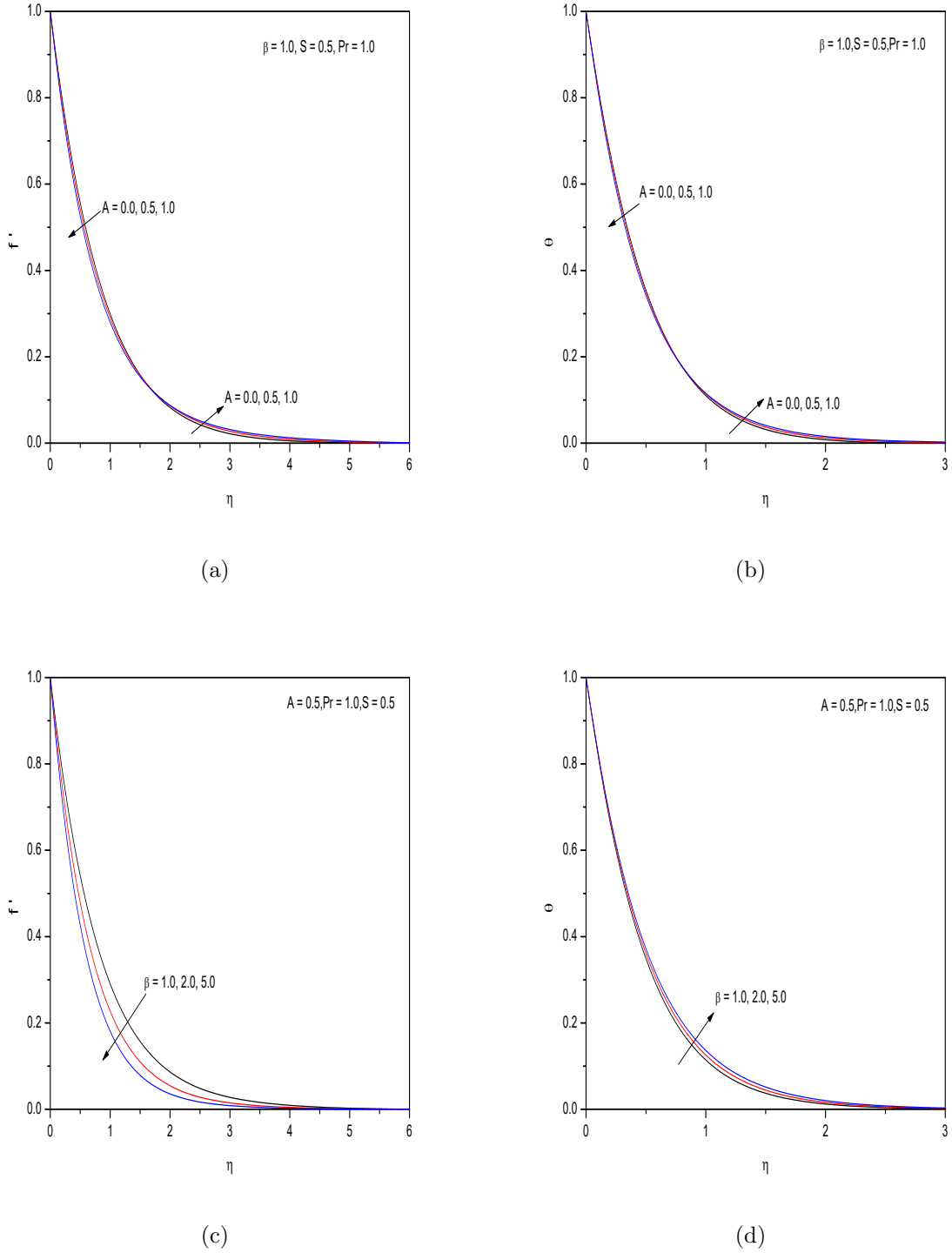

Figure 6.4: "Effect of the suction/injection parameter S on the profiles of $f'(\eta)$, $\theta(\eta)$, $f''(0)$ and $-\theta'(0)$.

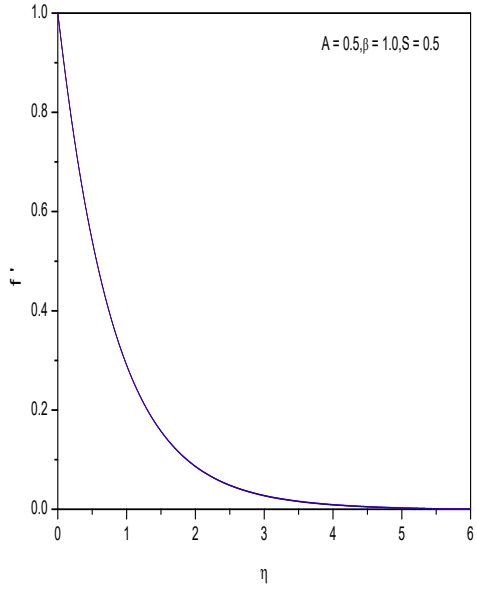

(a)

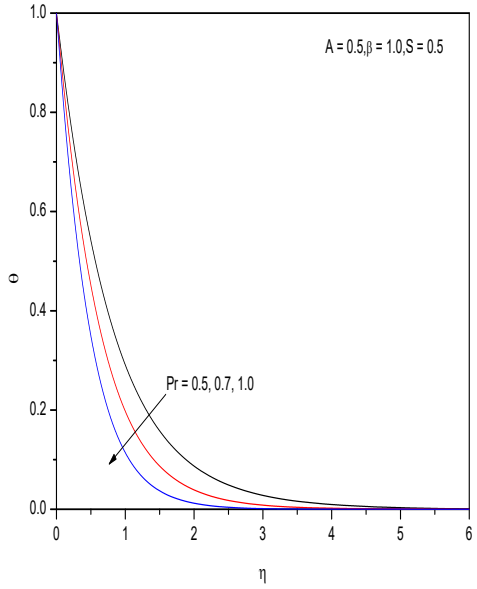

(b)

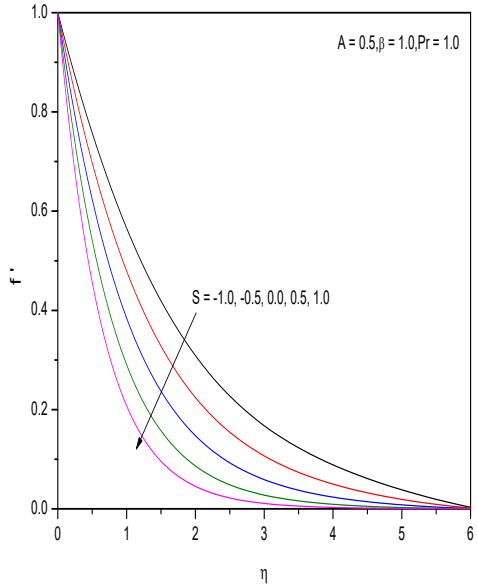

(c)

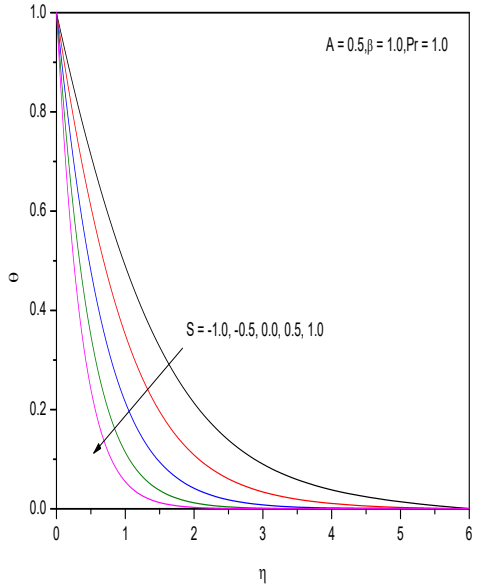

(d)

Figure 6.5: "Effect of the Magnetic parameter M on the profiles of $f'(\eta)$, $\theta(\eta)$, $f''(0)$ and $-\theta'(0)$."

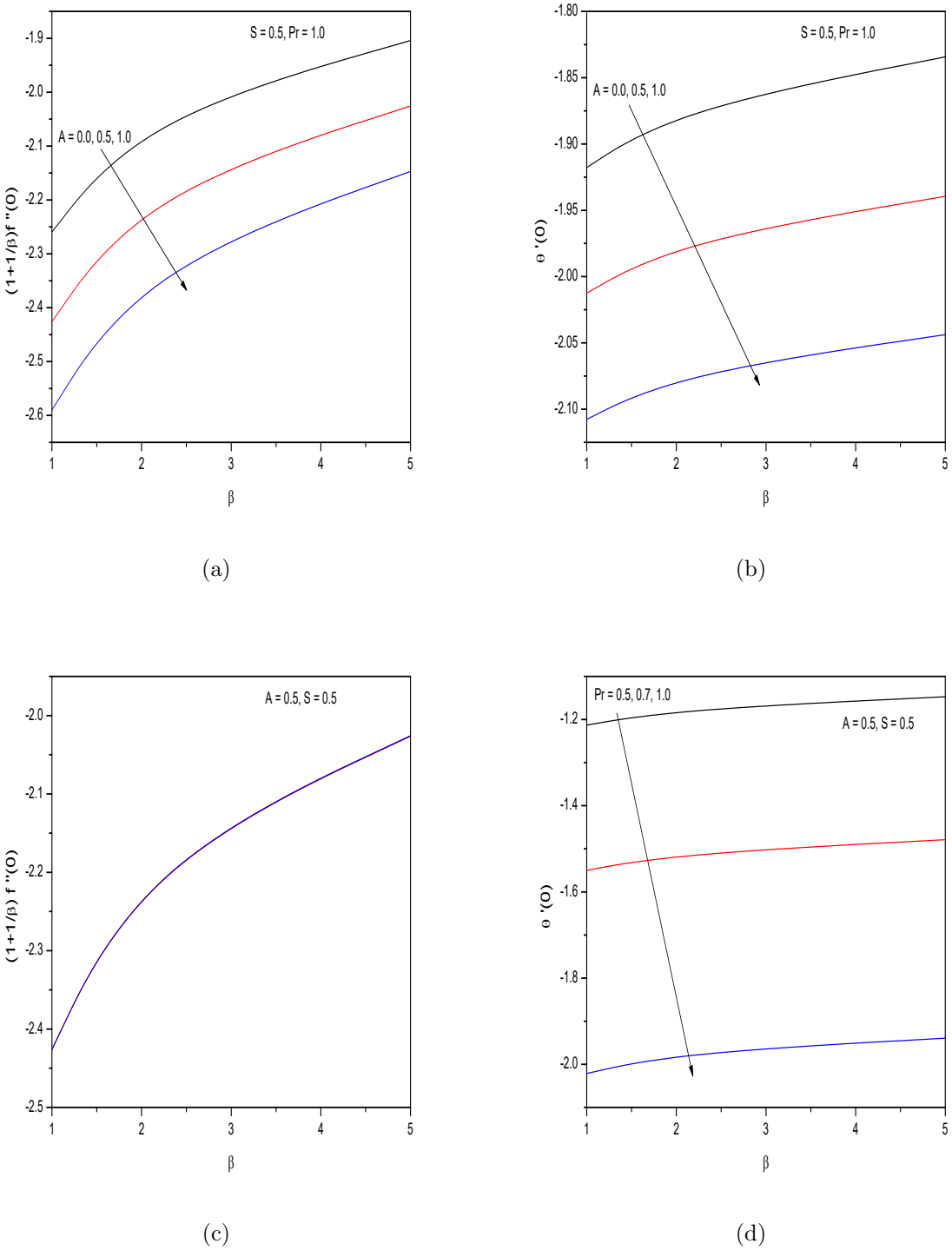

Figure 6.6: "Effect of the Radiation parameter R_d on the profiles of $f'(\eta)$, $\theta(\eta)$, $f''(0)$ and $-\theta'(0)$."

Chapter 7

Artificial Neural Network Treatment for Natural Convective Casson Fluid Flow and Heat Transfer Over a Radially Stretching Sheet with Chemical Reaction and Viscous dissipation Effect [1]

7.1 Introduction

The temperature of the fluid rises as a result of flow-induced friction at the surface. This phenomenon, known as viscous dissipation, is essential in viscous fluids such as oils and polymers. It has numerous applications in industry and technology. Viscous dissipation is commonly used in electrical equipment like light bulbs, electric stoves, electric heaters, and electric fuses. Furthermore, the influence of chemical reactions on heat and mass transfer is a

[1]Communicated to "**Journal of Applied Mathematics and Computing**"

crucial aspect in many disciplines of science and engineering. Shateyi et al. [84] explored the free convection towards a time dependent permeable stretched surface immersed in the Casson fluid flow featuring thermal radiation, viscous dissipation, and chemical reaction. Afify *et al.* [3] quantitatively explored the consequences of multiple slips with viscous dissipation on the flow and heat transfer of a Casson nanofluid over a stretching surface. Ibrahim *et al.* [33] reported the study of MHD flow of Casson naofluid over a nonlinearly stretched sheet in the presence of viscous dissipation and chemical reaction. Kumar *et al.* [39] conducted a thorough investigation of the coupled joule and viscous dissipation impacts on MHD stagnation point flow of viscous incompressible Casson fluid a p over a ermeable stretched surface with multiple slips, thermal radiation, and first order chemical reaction. Reddy *et al.* [71] reported that the Eckert number substantially affects the rate of heat transmission for Casson fluid when compared to Maxwell fluid. Nagaraja *et al.* [52] analyzed the impact of chemical reaction along with magnetic effect on Casson fluid flow over a curved stretched sheet under convective heat and mass flux circumstances.

The current chapter focuses on the application of the ANN approach to the analysis of an steady Casson fluid flow and heat transfer over vertical stretching sheet. The trial solutions for the coupled nonlinear differential equations are taken from the neural network output, which consists of weights and bias terms as parameters. Using the optimization technique, these parameters are changed to reduce the error term.

7.2 Formulation of the problem

Consider a steasdy two-dimensional flow of Casson fluid over a radially stretching sheet as shown in Figure 6.1. In addition to the assumptions made in Chapter 6, here we assume that the concentration at the surface is given by $C_w = C_\infty + br$, where C_w is the uniform concentration at the wall.

Hence, the equations describing the flow are given by

$$\frac{\partial u}{\partial r}+\frac{u}{r}+\frac{\partial w}{\partial z}=0 \tag{7.1}$$

$$u\frac{\partial u}{\partial r}+w\frac{\partial u}{\partial z}=\nu(1+\frac{1}{\beta})\frac{\partial^2 u}{\partial z^2}+g((T-T_\infty\beta_T)+(C-C_\infty)\beta_C) \tag{7.2}$$

$$u\frac{\partial T}{\partial r}+w\frac{\partial T}{\partial z}=\frac{k}{\rho c_p}\frac{\partial^2 T}{\partial z^2}+\frac{\mu}{c_p}(1+\frac{1}{\beta})(\frac{\partial u}{\partial z})^2 \tag{7.3}$$

$$u\frac{\partial C}{\partial r}+w\frac{\partial C}{\partial z}=D_s\frac{\partial^2 C}{\partial z^2}-k_1(C-C_\infty) \tag{7.4}$$

following are the associated boundary conditions:

$$\left.\begin{aligned} &u=U_w,\, w=W_0,\, T=T_w=T_\infty+br, C=C_w=C_\infty+br \quad \text{at} \quad z=0\\ &u\to 0,\, T\to T_\infty,\, C\to C_\infty \quad \text{as} \quad z\to\infty \end{aligned}\right\} \tag{7.5}$$

All the symbols in the above equations are defined in previous chapters.

In order to get dimensionless form of equations (7.1) - (7.4), we use the transformations given below.

$$\left.\begin{aligned} &\eta=z(\frac{a}{\nu})^{\frac{1}{2}},\quad u=arf'(\eta),\quad w=-2f(\eta)(\nu a)^{\frac{1}{2}},\\ &T=T_\infty+\theta(T_w-T_\infty)\quad \text{and}\quad C=C_\infty+\phi(C_w-C_\infty) \end{aligned}\right\} \tag{7.6}$$

Putting Eq (7.6),in Eqs. (7.1) - (7.4), we obtain

$$(1+\frac{1}{\beta})f'''+2ff''-(f')^2+\lambda_T\theta+\lambda_C\phi=0 \tag{7.7}$$

$$\frac{1}{\mathrm{Pr}}\theta''+2f\theta'-f'\theta+(1+\frac{1}{\beta})Ec(f'')^2=0 \tag{7.8}$$

$$\frac{1}{Sc}\phi''+2f\phi'-f'\phi-Kr\phi=0 \tag{7.9}$$

The non-dimensional form of the boundary conditions. (7.5) are

$$f(0)=S, f'(0)=1, f'(\infty)=0; \theta(0)=1, \theta(\infty)=0;\ \phi(0)=1, \phi(\infty)=0 \tag{7.10}$$

where $\lambda_T = \frac{g\beta_T b}{a^2}$ is the thermal buoyancy parameter, $\lambda_C = \frac{g\beta_C b}{a^2}$ is the concentration buoyancy parameter, $Ec = \frac{{U_w}^2}{c_p(T_w - T_\infty)}$ is the Eckert number, $Kr = \frac{k_1}{a}$ is the chemical reaction parameter.

The non-dimensional form of the physical quantities, the skin friction coefficient C_f, Nusselt number N_u and Sherwood number Sh are given by:

$$Re^{1/2}C_f = (1 + \frac{1}{\beta})f''(0),\ \frac{Nu}{\sqrt{Re}} = -\theta'(0)\ and\ \frac{Sh}{\sqrt{Re}} = -\phi'(0) \tag{7.11}$$

7.3 Method of Solution

As explained in the previous chapters, we consider a multilayered perceptron consisting of 3 – layers namely input layer - consisting of 'n' inputs $\bar{\eta}$=$(\eta_1, \eta_2, ...\eta_n)$, hidden layer - consisting of 'k' neurons and output layer consisting of 3 – neurons $N_1(\eta_i, P_1)$, $N_2(\eta_i, P_2)$ and $N_3(\eta_i, P_3)$ to estimate the solutions of three coupled ordinary differential equations as demonstrated in the Figure 7.1.

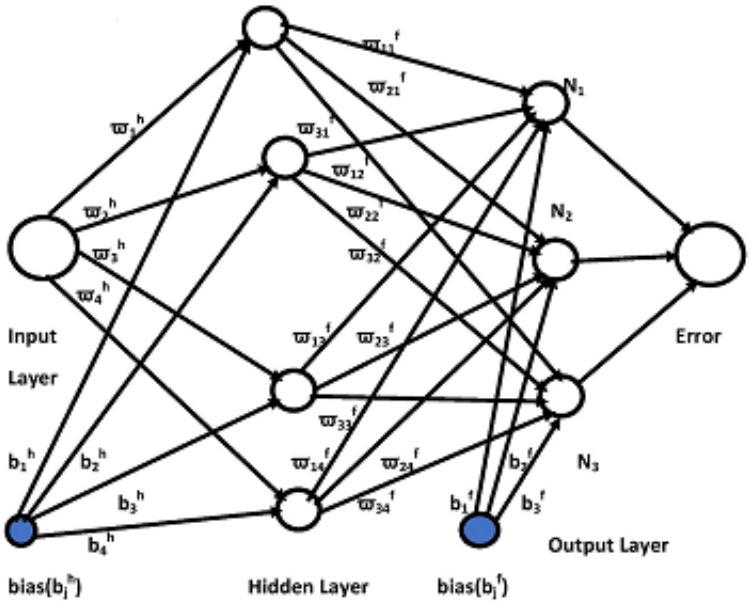

Figure 7.1: "A Simple Neural Network."

Here, we take the these Network outputs $N_1(\eta_i, P_1)$, $N_2(\eta_i, P_2)$ and $N_3(\eta_i, P_3)$ as the trial solution for f, θ and ϕ with the adjustable parameters P_1, P_2 and P_3 respectively, which are given by the expressions

$$\left.\begin{aligned} N_1(\eta_i, P_1) &= \sum_{j=1}^{k} \varpi_{1j}^f \sigma\{\varpi_j^h \eta_i + b_j^h\} + b_1^f \\ N_2(\eta_i, P_2) &= \sum_{j=1}^{k} \varpi_{2j}^f \sigma\{\varpi_j^h \eta_i + b_j^h\} + b_2^f \\ N_3(\eta_i, P_3) &= \sum_{j=1}^{k} \varpi_{3j}^f \sigma\{\varpi_j^h \eta_i + b_j^h\} + b_3^f \end{aligned}\right\} \tag{7.12}$$

where, ϖ_j^h represents the weights from the input layer to the j^{th} hidden neuron, b_j^h is the bias term in the hidden layer, ϖ_{1j}^f, ϖ_{2j}^f, ϖ_{3j}^f are the weights from the j^{th} hidden neuron to the first, second and third output neurons respectively, b_1^f, b_2^f, b_3^f are the bias terms in the output layer, P_1 corresponds to the parameters ϖ_j^h, b_j^h, ϖ_{1j}^f, b_1^f, P_2 corresponds to the parameters ϖ_j^h, b_j^h, ϖ_{2j}^f and b_2^f respectively and P_3 corresponds to the parameters ϖ_j^h, b_j^h, ϖ_{3j}^f, b_3^f.

Since there are no data available in order to learn from the differential equation, we have to substitute Eq. (7.12) in the differential equations Eq. (7.7) - Eq. (7.9). Hence, we get

$$\begin{aligned} E_f = &(1 + \frac{1}{\beta}) N_1'''(\eta_i, P_1) + 2N_1(\eta_i, P_1) N_1''(\eta_i, P_1) - \left(N_1'(\eta_i, P_1)\right)^2 \\ &+ \lambda_T N_2(\eta_i, P_2) + \lambda_C N_3(\eta_i, P_3) \end{aligned} \tag{7.13}$$

$$\begin{aligned} E_\theta = &\frac{1}{Pr} N_2''(\eta_i, P_2) + 2N_1(\eta_i, P_1) N_2'(\eta_i, P_2) - N_1'(\eta_i, P_1) N_2(\eta_i, P_2) \\ &+ (1 + \frac{1}{\beta}) Ec \left(N_1''(\eta_i, P_1)\right)^2 \end{aligned} \tag{7.14}$$

$$\begin{aligned} E_\phi = &\frac{1}{Sc} N_3''(\eta_i, P_3) + 2N_1(\eta_i, P_1) N_3'(\eta_i, P_3) - N_1'(\eta_i, P_1) N_3(\eta_i, P_3) \\ &- Kr N_3(\eta_i, P_3) \end{aligned} \tag{7.15}$$

where E_f, E_θ and E_ϕ represents the errors or residuals with respect to the equations Eq. (7.7) - Eq. (7.9) respectively. If the trial/constructed solutions for f, θ and ϕ given in Eq.

(7.12) are close to exact solution then the errors E_f, E_θ and E_ϕ tend to zero.

Similarly, the errors in the boundary conditions are given by:

$$\left.\begin{aligned} &N_1(\eta_1, P_1) = S;\ N_1'(\eta_1, P_1) = 1;\ N_2(\eta_1, P_2) = 1;\ N_3(\eta_1, P_3) = 1 \\ &N_1'(\eta_n, P_1) = 0;\ N_2(\eta_n, P_2) = 0;\ N_3(\eta_n, P_3) = 0 \end{aligned}\right\} \tag{7.16}$$

The mean square of error (MSE) is calculated by taking $1/n$ times the sum of the squared errors of differential equations (Eqs. (7.13) - (7.15)) along with the error in the boundary conditions Eqs. (7.16) on the training set and then minimized. The solution produced by determining a set of biases and weights that minimizes the MSE (or loss function) after training is the final solution of the problem. Hence, the MSE or loss function $\mathfrak{E}(P_1, P_2, P_3)$ is given by

$$\begin{aligned} \mathfrak{E}(P_1, P_2, P_3) = &\frac{1}{n}\sum_{i=1}^{n} (E_f)^2 + (E_\theta)^2 + (E_\phi)^2 \\ &+ [N_1(\eta_1, P_1) - S]^2 + [N_1'(\eta_1, P_1) - 1]^2 + [N_2(\eta_1, P_2) - 1]^2 \\ &+ [N_3(\eta_1, P_3) - 1]^2 + [N_1'(\eta_n, P_1)]^2 + [N_2(\eta_n, P_2)]^2 + [N_3(\eta_n, P_3)]^2 \end{aligned} \tag{7.17}$$

The problem is to minimize $\mathfrak{E}(P_1, P_2, P_3)$ by optimizing the biases and weights in the network for a given network configuration. The derivatives of the network output with respect to its input must be evaluated in order to determine the error function $\mathfrak{E}(P_1, P_2, P_3)$. The derivatives of networks output $N_1(\eta_i, P_1)$, $N_2(\eta_i, P_2)$ and $N_3(\eta_i, P_3)$ with respect to input vector η_i are calculated using Python package called autograd. Backpropagation may then be utilised to further optimise the loss function by assessing its derivatives with respect to the network parameters. We employed a single hidden layer, Sigmoid activation function, and the Adam optimizer [38] with an initial learning rate of 0.01 in this study.

To apply this method the semi-infinite domain of the given problem i.e. $[0, \infty]$ is reduced to $[\eta_1, \eta_\infty]$ where $\eta_1 = 0$, η_∞ is the parameter used to recover the boundary conditions at infinity. We start with training points that are chosen from the domain of the given problem i.e. $[0, \eta_\infty = 8]$ and the weights and bias terms, which are generated randomly and we train

the model to modify the parameters in the given domain of the problem.To ensure that the boundary conditions in the loss are integrated into each network parameter update, we use the entire set of training points. In general, we find that a single hidden layer with a small number of units is enough to get very exact results.

To check the convergence of the solution of the method, the dimensionless coefficient of skin friction ($f''(0)$), rate of heat transfer ($\theta'(0)$) and Sherwood number ($\phi'(0)$) at the surface for $\beta = 1.0$, $Ec = 0.2$, $Kr = 0.2$, $\lambda_C = 1.0$, $\lambda_T = 1.0$, $S = 0.5$, $Pr = 1.0$, $Sc = 0.2$ and are calculated by choosing different number of training points 50, 100, 200 and 300 and different number of neurons 5, 10 and 20 in the hidden layer and the computed results are presented in the Tables 7.1 and 7.2. It is evident from the Tables 7.1 and 7.2 that the solution has convergence of 10^{-4} when the Data points are 50 and Hidden neurons are 10.

Number of training points	$f''(0)$	$\theta'(0)$	$\phi'(0)$
50	-0.575529	-1.90737	-0.669203
100	-0.575645	-1.907452	-0.669127
200	-0.575564	-1.907352	-0.669126
300	-0.575609	-1.907315	-0.669117

Table 7.1: "Convergence table for the values of $f''(0)$,$\theta'(0)$ and $\phi'(0)$ for β=1.0, Ec=0.2, Kr=0.2, λ_C=1.0, λ_T=1.0, S=0.5, Pr=1.0, Sc=0.2 by the present method with different number of Data points and number of Neurons as 10."

Number of Hidden Neurons	$f''(0)$	$\theta'(0)$	$\phi'(0)$
5	-0.577569	-1.909601	-0.66961
10	-0.575529	-1.90737	-0.669203
20	-0.575955	-1.90618	-0.669158

Table 7.2: "Convergence table for the values of $f''(0)$,$\theta'(0)$ and $\phi'(0)$ for β=1.0, Ec=0.2, Kr=0.2, λ_C=1.0, λ_T=1.0, S=0.5, Pr=1.0, Sc=0.2 by the present method with different number of Hidden neurons and number of Data points fixed as 50."

7.4 Computational Results and Discussion

The efficiency of the approach is confirmed by comparing the present findings of the skin friction coefficient and rate of heat transfer coefficient computed using the shooting method in conjunction with the Runge-Kutta fourth order method for $\beta = 1.0$, $Ec = 0.2$, $Kr = 0.2$, $\lambda_C = 1.0$, $\lambda_T = 1.0$, $S = 0.5$, $Pr = 1.0$, $Sc = 0.2$. The computed results are presented in the Table 7.3. Table 7.3 demonstrate that the present results are consistent with the results obtained by using shooting method.

	Present method	Shooting method	Relative error
$f''(0)$	-0.575529	-0.5754464	1.44×10^{-4}
$\theta'(0)$	-1.90737	-1.90636356	5.28×10^{-4}
$\phi'(0)$	-0.669203	0.6691361	9.99×10^{-5}

Table 7.3: "Comparison of the present method with Shooting method."

A comparison of acquired results is established for Skin friction coefficient and Nusselt number with existing works for β=∞, $\lambda_C = 0.0$, $\lambda_T = 0.0$, $Kr = 0.0$, $A = 0.0$ and $Sc = 0.0$. Table 7.4 provides a well-justified comparison of our results with Shahzad et al. [81] for $f''(0)$ and $\theta'(0)$.

	Present method	Shahzad et al. [81]	Relative error
$f''(0)$	-1.798938	-1.798999	3.39×10^{-5}
$\theta'(0)$	-1.799092	-1.798999	5.17×10^{-5}

Table 7.4: "Comparison of the present method with the results of Shahzad et al. [81]."

Fig. 7.2 illustrates the plot of error (between ANN method and Shooting technique results) in the values of $f'(\eta)$, $\theta(\eta)$, and $\phi(\eta)$ for 9 equispaced positions in $[0, 8]$. The present method's (ANN method) conclusions are in perfect accord with those produced by Shooting method. as shown in Figure 7.2.

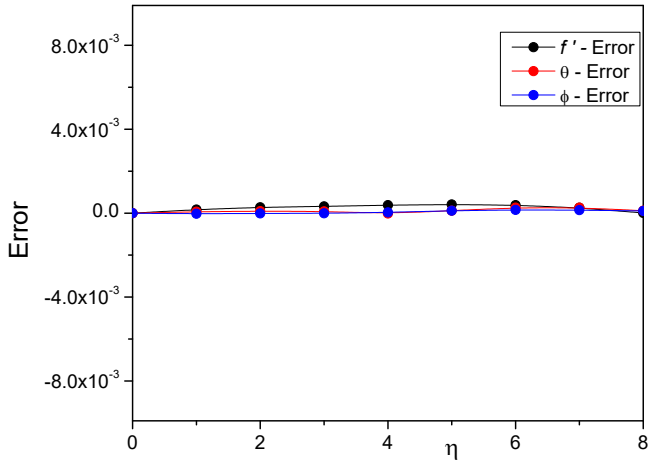

Figure 7.2: "Error plot between the results obtained by Artificial Neural Network method and Shooting method for the values of velocity, temperature and concentration profiles."

The effect of Eckert number Ec on $f''(0))$, $-\theta'(0))$ and $-\phi'(0)))$ was discussed in figures 7.3. Figures 7.3(a), 7.3(b) and 7.3(c) show that at increased values of the Eckert number Ec, skin friction, the Sherwood number, and the Nusselt number all decrease.

The consequence of chemical reaction parameter Kr on skin friction $(f''(0))$, Nusselt number $(-\theta'(0))$ and Sherwood number $(-\phi'(0)))$ was discussed in figures 7.4. It is observed from figures 7.4(a), 7.4(b) and 7.4(c) that skin friction, Nusselt number are decreasing and Sherwood number is increasing for an increase in chemical reaction parameter Kr.

The effect of concentration buoyancy parameter λ_C was discussed in figures 7.5. It is observed from figures 7.5(a)–7.5(c) that skin friction, Nusselt number and Sherwood number are increasing with the increased values of concentration buoyancy parameter λ_C.

The effect of thermal buoyancy parameter λ_T was discussed in figures 7.6. It is observed from figures 7.6(a), 7.6(b) and 7.6(c) that skin friction, Nusselt number and Sherwood number are increasing with the increased values of thermal buoyancy parameter λ_T.

The effect of suction/injection parameter S was discussed in figures 7.7. It is observed from figures 7.7(a)–7.7(c) that skin friction is decreasing and Nusselt number, Sherwood

number are increasing with the increasing values of suction / injection parameter S.

The effect of Schmidth number Sc was discussed in figures 7.8. It is observed from figures 7.8(a), 7.8(b) and 7.8(c) that skin friction, Nusselt number are decreasing and Sherwood number is increasing with the increasing values of Schmidth number Sc.

7.5 Conclusions

The boundary layer flow of a Casson fluid over a vertical stretched sheet in the presence of chemical reaction and viscous dissipation is analysed using Artificial Neural Network approach . The influences of the parameters α, β, Ec, λ, N_c, P_r, S and Sc on the relevant physical quantities are investigated. The important findings are presented below:

- TSkin friction rises as we raise Eckert number, thermal buoyancy parameter, and concentration buoyancy parameter, but decreases with increasing Prandtl number, suction/injection parameter, Schmidth number, and chemical reaction parameter.
- Nusselt number is increasing for the increased values of concentration buoyancy parameter, thermal buoyancy parameter, Prandtl number and suction / injection parameter, whereas it is decreased when the values of Eckert number, chemical reaction parameter and Schmidth number Sc were increased.
- Sherwood number decreases when Prandtl number increases, but it increases for all other factors stated in the problem.

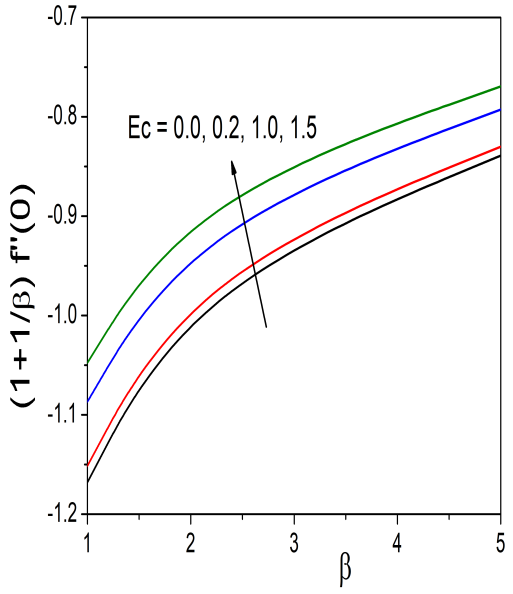

(a)

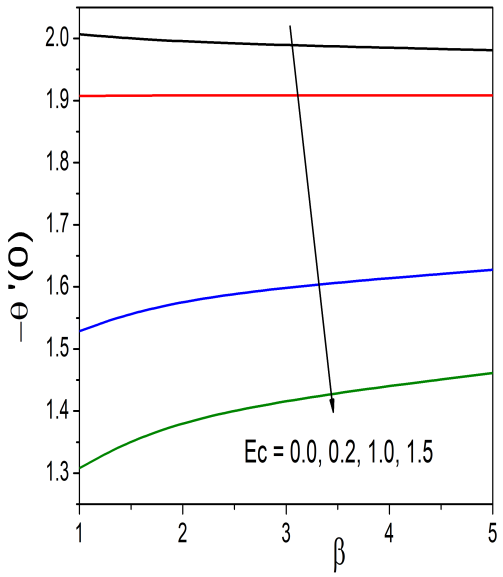

(b)

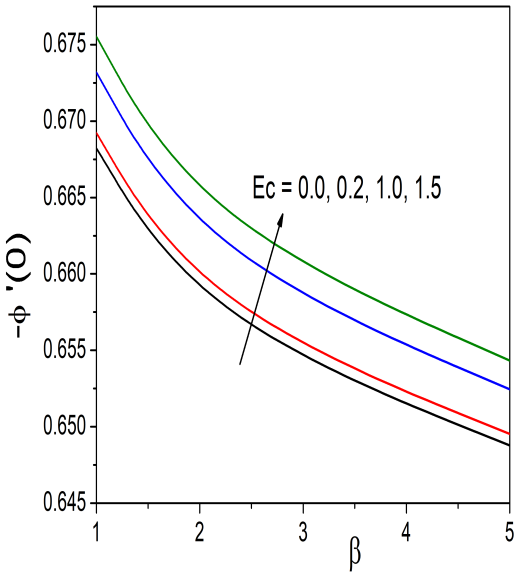

(c)

Figure 7.3: "Plot of $f''(0)$, $-\theta'(0)$ and $-\phi'(0)$ for distinct values of Eckert number Ec."

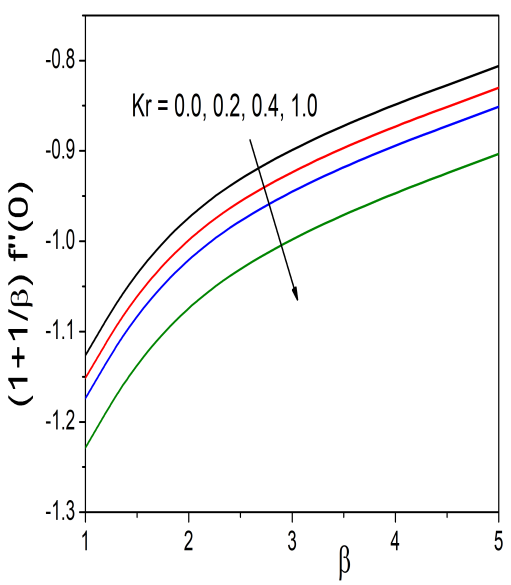

(a)

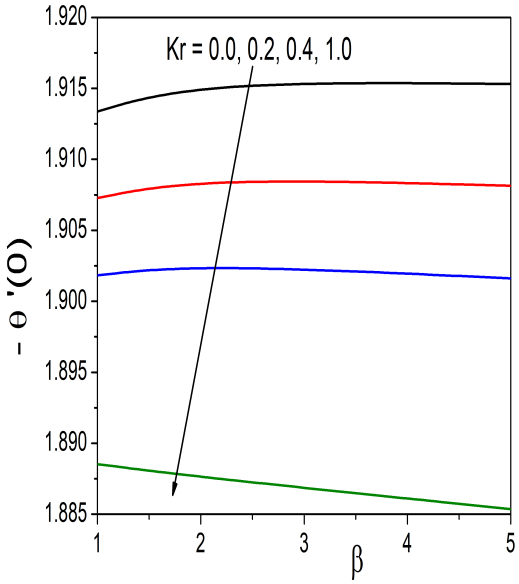

(b)

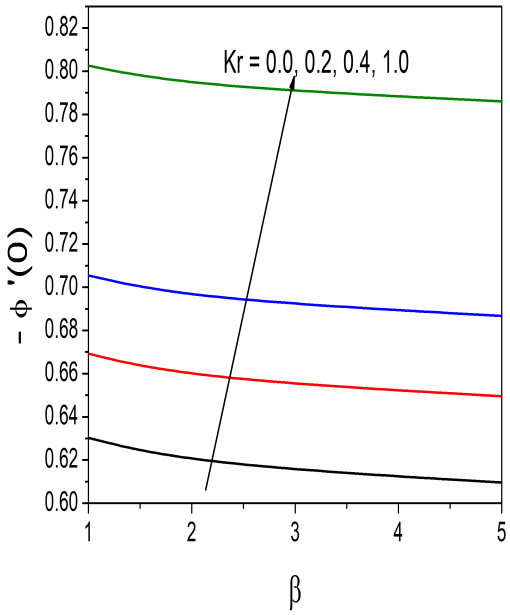

(c)

Figure 7.4: "Plot of $f''(0)$, $-\theta'(0)$ and $-\phi'(0)$ for distinct values of chemical reaction parameter Kr."

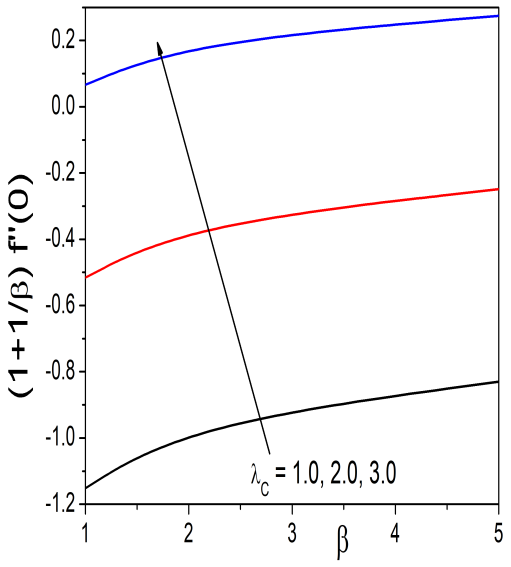

(a)

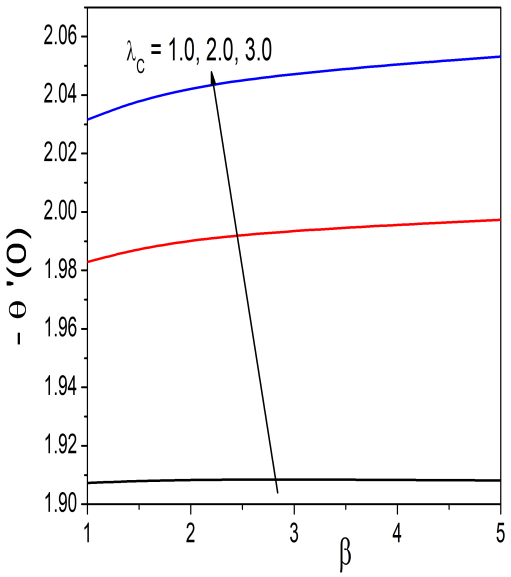

(b)

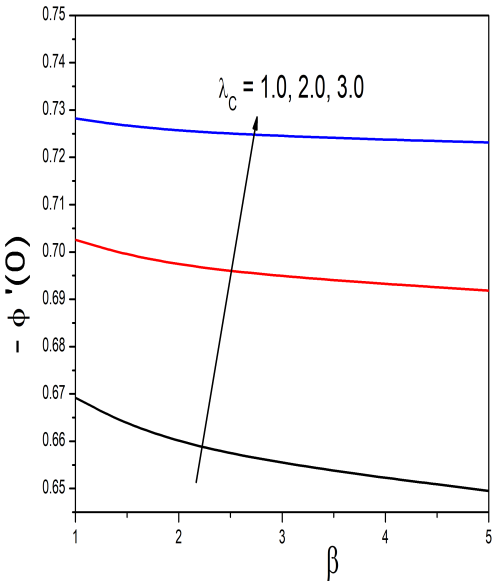

(c)

Figure 7.5: "Plot of $f''(0)$, $-\theta'(0)$ and $-\phi'(0)$ for distinct values of concentration buoyancy parameter λ_C."

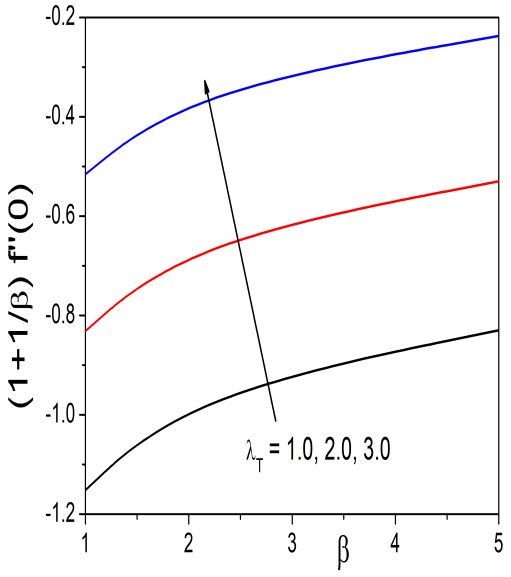

(a)

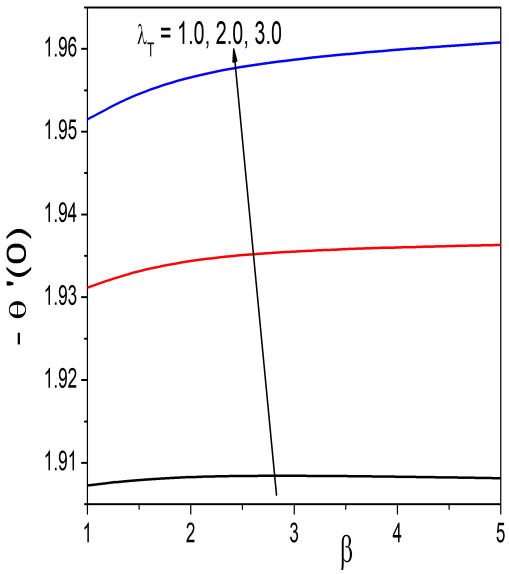

(b)

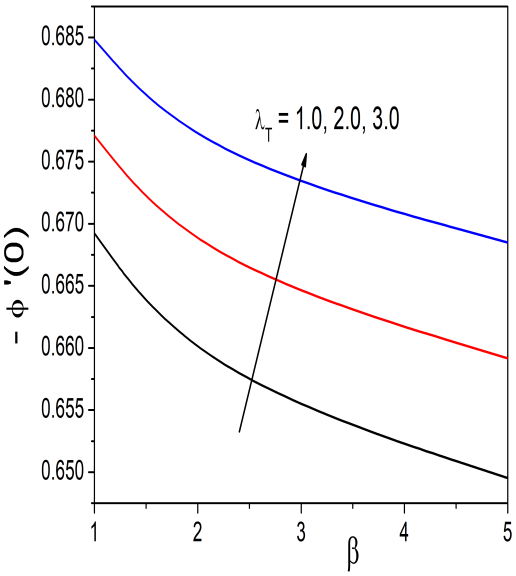

(c)

Figure 7.6: "Plot of $f''(0)$, $-\theta'(0)$ and $-\phi'(0)$ for distinct values of thermal buoyancy parameter λ_T."

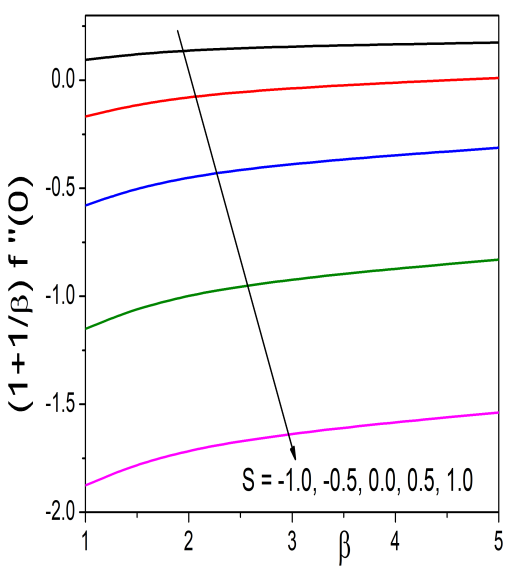

(a)

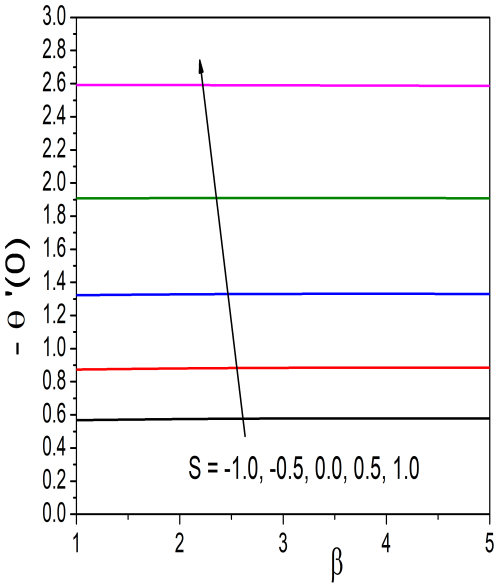

(b)

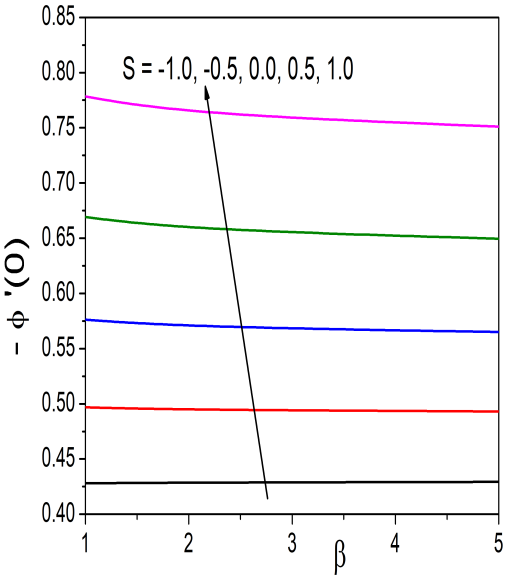

(c)

Figure 7.7: "Plot of $f''(0)$, $-\theta'(0)$ and $-\phi'(0)$ for distinct values of the suction/injection parameter S."

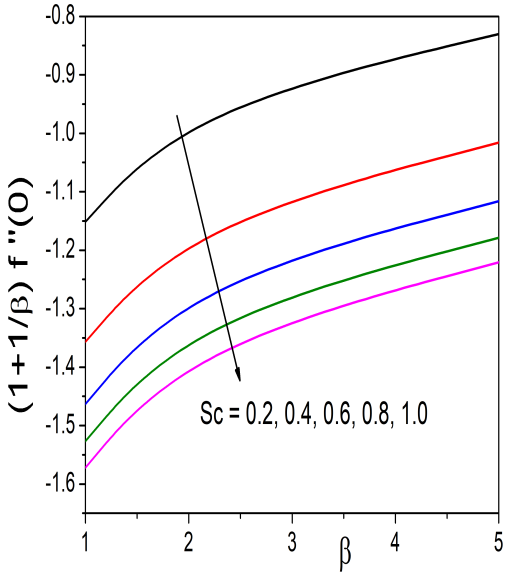

(a)

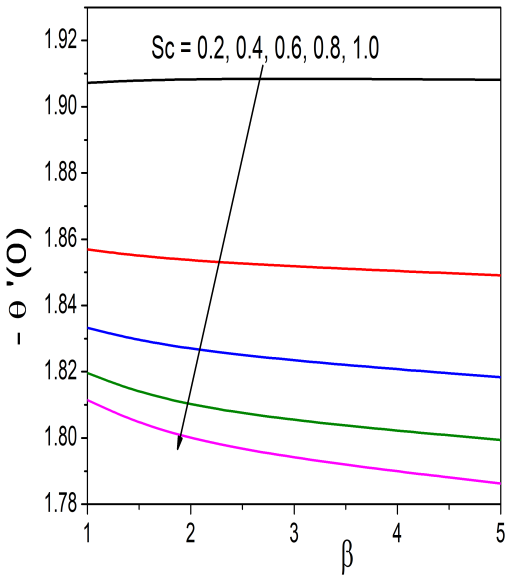

(b)

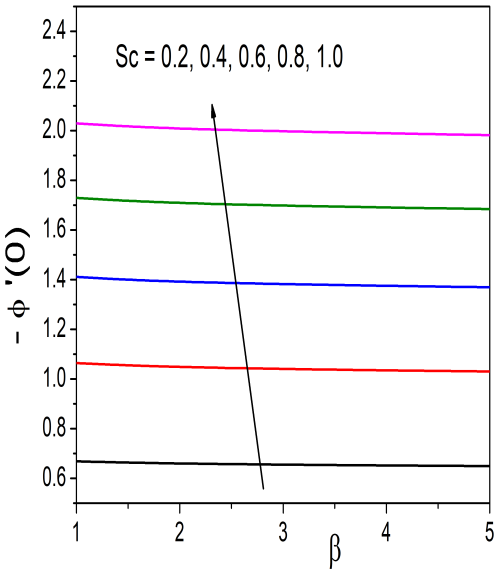

(c)

Figure 7.8: "Plot of $f''(0)$, $-\theta'(0)$ and $-\phi'(0)$ for distinct values of Schmidth number Sc."

Chapter 8

A Neural Network Analysis for Bioconvection in a Casson Fluid Over a Vertical Radially extending sheet [1]

8.1 Introduction

Microorganisms, such as microalgae and bacteria, have a higher density than water and so move upwards against gravity. Microbe accumulation causes the top layer of suspension to be denser than the bottom layer, resulting in an unstable density distribution. Convective instability occurs as a result, which may result in convection patterns. The spontaneous and unpredictable movement patterns of microorganisms in suspension are referred to as bioconvection. Chemical processes have a critical role in bioconvection in the presence of motile bacteria due to their importance in food processing, material synthesis, polymer creation, bioreactors, fuel cells, and biodiesel fuels. Pedley *et al.* [63] coined the term bioconvection to describe tiny convection caused by motile microorganisms. Several researchers, to mention a few, Pal *et al.* [62], Ray *et al.* [69], Sabir *et al.* [75], Magagula *et al.* [46], Sankad *et al.* [79], Kumaraswamy *et al.* [53] etc have analyzed the impact of thermal radiation on the bio-

[1] Communicated to "**International journal of Applied and Computational Mathematics**"

convection of Casson fluid containing motile gyrotactic microrganisms over an exponential / linear / nonlinear / radially stretching sheet.

The current chapter focuses on the application of the ANN approach to the analysis of a bioconvection flow over steady radially stretched sheet. The trial solutions for the coupled nonlinear differential equations are taken from the neural network output, which consists of weights and bias terms as parameters. Using the optimization technique, these parameters are changed to reduce the error term.

8.2 Formulation of the problem

Consider the two-dimensional, steady Casson fluid flow over a radially stretching sheet as shown in Figure 6.1. In addition to the assumptions made in Chapter 6, here we assume that the concentration of microorganisms at the surface is given by $\mathbb{N}_w = \mathbb{N}_\infty + br$, where $\mathbb{N}_\infty$ is the concentration of the micoorganisms in the ambient medium.

The equations describing the flow are given by

$$\frac{\partial u}{\partial r} + \frac{u}{r} + \frac{\partial w}{\partial z} = 0 \tag{8.1}$$

$$u\frac{\partial u}{\partial r} + w\frac{\partial u}{\partial z} = \nu(1 + \frac{1}{\beta})\frac{\partial^2 u}{\partial z^2} + g\beta_T(T - T_\infty) + g\beta_C(C - C_\infty) + g\beta_N(N - N_\infty)) \tag{8.2}$$

$$u\frac{\partial T}{\partial r} + w\frac{\partial T}{\partial z} = \frac{k}{\rho c_p}\frac{\partial^2 T}{\partial z^2} \tag{8.3}$$

$$u\frac{\partial C}{\partial r} + w\frac{\partial C}{\partial z} = D_s\frac{\partial^2 C}{\partial z^2} \tag{8.4}$$

$$u\frac{\partial \mathbb{N}}{\partial r} + w\frac{\partial \mathbb{N}}{\partial z} + \frac{b^* W_c}{C_w - C_\infty}\left[\frac{\partial}{\partial z}(\mathbb{N}\frac{\partial C}{\partial z})\right] = D_m\frac{\partial^2 \mathbb{N}}{\partial z^2} \tag{8.5}$$

The corresponding boundary conditions are as follows:

$$\left.\begin{aligned} &u = U_w = ar, \quad w = W_0, T = T_w = T_\infty + br, \\ &C = C_w = C_\infty + br, \mathbb{N} = \mathbb{N}_w = \mathbb{N}_\infty + br \quad at \quad z = 0 \\ &u \to 0, \quad T \to T_\infty, \quad C \to C_\infty \; and \; \mathbb{N} \to \mathbb{N}_\infty \; as \; z \to \infty \end{aligned}\right\} \tag{8.6}$$

where β_N is bioconvection expansion coefficient, and D_m is the motile microorganism diffusion coefficient. The remaining variables are already defined in the previous chapters.

In order to get dimensionless form of Equations (8.1) - (8.5), we introduce the following transformations

$$\left.\begin{aligned} &u(r,z) = arf'(\eta),\, w(r,z) = -2\sqrt{a\nu} f(\eta),\, \eta = \sqrt{\frac{a}{\nu}} z, T = T_\infty + (T_w - T_\infty)\,\theta(\eta) \\ &C = T_\infty + (C_w - C_\infty)\,\phi(\eta), \quad \mathbb{N} = \mathbb{N}_\infty + (\mathbb{N}_w - \mathbb{N}_\infty)\chi(\eta) \end{aligned}\right\} \tag{8.7}$$

After using similarity transformation defined in (8.7), the momentum, energy, concentration and bioconvection equations (8.2) – (8.5) in their dimensionless from are

$$(1 + \frac{1}{\beta}) f''' + 2ff'' - (f')^2 + \lambda_T \theta + \lambda_C \phi + \lambda_N \chi = 0 \tag{8.8}$$

$$\frac{1}{\mathrm{Pr}} \theta'' + 2f\theta' - f'\theta = 0 \tag{8.9}$$

$$\frac{1}{Sc} \phi'' + 2f\phi' - f'\phi = 0 \tag{8.10}$$

$$\frac{1}{Sb} \chi'' + 2f\chi' - f'\chi - Pe(\phi'\chi' + \sigma_b \phi'' + \chi\phi'') = 0 \tag{8.11}$$

the boundary conditions given in Eq. (8.6) are transformed into the following form:

$$\left.\begin{aligned} f(0) = S,\, f'(0) = 1,\, \theta(0) = \phi(0) = \chi(0) = 1 \\ f'(\infty) \to 0,\, \theta(\infty) \to 0,\, \phi(\infty) \to 0 \, and \, \chi(\infty) \to 0 \end{aligned}\right\} \tag{8.12}$$

where $\lambda_C = \frac{g\beta_C b}{a^2}$ is the concentration buoyancy parameter, $\lambda_N = \frac{g\beta_N b}{a^2}$ is the bioconvection buoyancy parameter, $\lambda_T = \frac{g\beta_T b}{a^2}$ is the temperature buoyancy parameter, and $\sigma_b = \frac{\mathbb{N}_\infty}{\mathbb{N}_w - \mathbb{N}_\infty}$ is

dimensionless bioconvection constant.

The dimensionless form of the physical quantities of the interest i.e. the skin friction coefficient C_f, the Nusselt number N_u, the Sherwood number Sh and density number of the motile microorganisms N_n are:

$$\frac{1}{2}{R_e}^{1/2}C_f = (1+\frac{1}{\beta})f''(0),\ {R_e}^{-1/2}N_u = -\theta'(0),\ {R_e}^{-1/2}S_h = -\phi'(0) \text{ and } {R_e}^{-1/2}N_n = -\chi'(0) \tag{8.13}$$

8.3 Method of Solution

Consider a multilayered perceptron consisting of 3-layers namely input layer - consisting of 'n' inputs $\bar{\eta}$=$(\eta_1, \eta_2, ...\eta_n)$, hidden layer - consisting of 'k' neurons and output layer consisting of 4 – neurons $N_1(\eta_i, P_1)$, $N_2(\eta_i, P_2)$, $N_3(\eta_i, P_3)$ and $N_4(\eta_i, P_4)$ to estimate the solutions of four coupled nonlinear ordinary differential equations as shown in the Fig.8.1.

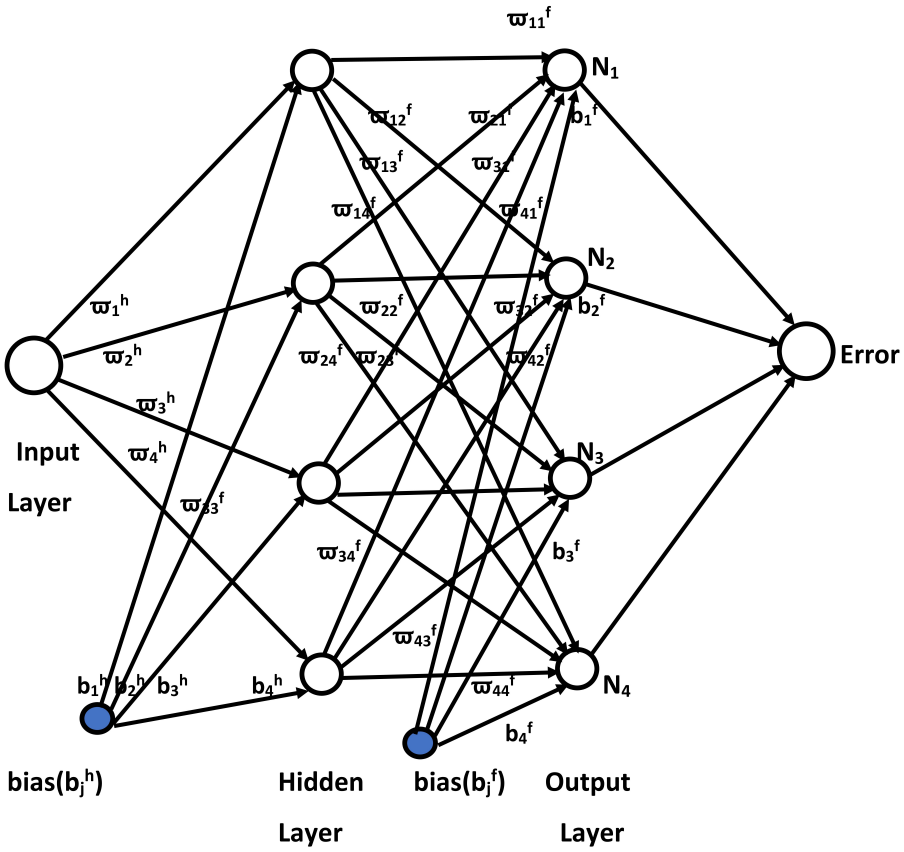

Figure 8.1: "Feed Forward Neural Network."

We take the Network outputs $N_1(\eta_i, P_1)$, $N_2(\eta_i, P_2)$, $N_3(\eta_i, P_3)$ and $N_4(\eta_i, P_4)$ as the trial solution for f, θ, ϕ and χ with the adjustable parameters P_1, P_2, P_3 and P_4 respectively, which are given by the expressions.

$$\left.\begin{aligned} N_1(\eta_i, P_1) &= \sum_{j=1}^{k} \varpi_{1j}^f \sigma\{\varpi_j^h \eta_i + b_j^h\} + b_1^f; \quad N_2(\eta_i, P_2) = \sum_{j=1}^{k} \varpi_{2j}^f \sigma\{\varpi_j^h \eta_i + b_j^h\} + b_2^f \\ N_3(\eta_i, P_3) &= \sum_{j=1}^{k} \varpi_{3j}^f \sigma\{\varpi_j^h \eta_i + b_j^h\} + b_3^f; \quad N_4(\eta_i, P_4) = \sum_{j=1}^{k} \varpi_{4j}^f \sigma\{\varpi_j^h \eta_i + b_j^h\} + b_4^f \end{aligned}\right\} \tag{8.14}$$

where, ϖ_j^h represents the weights from the input layer to the j^{th} hidden neuron, b_j^h is the bias term in the hidden layer, ϖ_{1j}^f, ϖ_{2j}^f, ϖ_{3j}^f and ϖ_{4j}^f are the weights from the j^{th} hidden neuron to the first, second, third and fourth output neurons respectively, b_1^f, b_2^f, b_3^f and b_4^f are the bias terms in the output layer, P_1 corresponds to the parameters ϖ_j^h, b_j^h, ϖ_{1j}^f, b_1^f,

P_2 corresponds to the parameters ϖ_j^h, b_j^h, ϖ_{2j}^f and b_2^f respectively, P_3 corresponds to the parameters ϖ_j^h, b_j^h, ϖ_{3j}^f, b_3^f and P_4 corresponds to the parameters ϖ_j^h, b_j^h, ϖ_{4j}^f, b_4^f.

$$\begin{aligned} E_f &= (1+\frac{1}{\beta})N_1'''(\eta_i,P_1) + 2N_1(\eta_i,P_1)N_1''(\eta_i,P_1) - (N_1'(\eta_i,P_1))^2 \\ &+ \lambda_T N_2(\eta_i,P_2) + \lambda_C N_3(\eta_i,P_3) + \lambda_N N_4(\eta_i,P_3) \end{aligned} \tag{8.15}$$

$$E_\theta = \frac{1}{Pr}N_2''(\eta_i,P_2) + 2N_1(\eta_i,P_1)N_2'(\eta_i,P_2) - N_1'(\eta_i,P_1)N_2(\eta_i,P_2) \tag{8.16}$$

$$E_\phi = \frac{1}{Sc}N_3''(\eta_i,P_3) + 2N_1(\eta_i,P_1)N_3'(\eta_i,P_3) - N_1'(\eta_i,P_1)N_3(\eta_i,P_3) \tag{8.17}$$

$$\begin{aligned} E_\chi &= \frac{1}{Sb}N_4''(\eta_i,P_4) + 2N_1(\eta_i,P_1)N_4'(\eta_i,P_4)) - N_1'(\eta_i,P_1)N_4(\eta_i,P_4) \\ &- P_e(N_3'(\eta_i,P_3)N_4'(\eta_i,P_4) + \sigma_b N_3''(\eta_i,P_4) + N_4(\eta_i,P_4)N_3''(\eta_i,P_4)) \end{aligned} \tag{8.18}$$

where E_f, E_θ, E_ϕ and E_χ represents the errors or residuals with respect to the equations Eq. (8.8) - Eq. (8.11) respectively. If the trial/constructed solutions for f, θ, ϕ and χ given in Eq. (8.14) are close to exact solution then the errors E_f, E_θ E_ϕ and E_χ tend to zero.

Similarly, the errors in the boundary conditions are given by:

$$\left.\begin{aligned} &N_1(\eta_1,P_1) = S;\ N_1'(\eta_1,P_1) = 1;\ N_2(\eta_1,P_2) = 1;\ N_3(\eta_1,P_3) = 1;\ N_4(\eta_1,P_4) = 1 \\ &N_1'(\eta_n,P_1) = 0; \quad N_2(\eta_n,P_2) = 0; \qquad N_3(\eta_n,P_3) = 0; \quad and \quad N_4(\eta_n,P_4) = 0 \end{aligned}\right\} \tag{8.19}$$

The mean square of error (MSE) is calculated by taking $1/n$ times the sum of the squared errors of differential equations (Eqs. (8.15) - (8.17)) along with the error in the boundary conditions Eqs. (8.18) on the training set and then minimized. The solution produced by determining a set of biases and weights that minimizes the MSE (or loss function) after training is the final solution of the problem. Hence, the MSE or loss function $\mathfrak{E}(P_1,P_2,P_3,P_4)$ is given by

$$\begin{aligned}\mathfrak{E}(P_1,P_2,P_3,P_4) &= \frac{1}{n}\sum_{i=1}^{n}(E_f)^2+(E_\theta)^2+(E_\phi)+(E_\chi)^2+\left[N_1(\eta_1,P_1)-S\right]^2 \\ &+\left[N_1'(\eta_1,P_1)-1\right]^2+\left[N_1'(\eta_n,P_1)\right]^2+\left[N_2(\eta_1,P_2)-1\right]^2+\left[N_2(\eta_n,P_2)\right]^2 \\ &+\left[N_3(\eta_1,P_3)-1\right]^2+\left[N_3(\eta_n,P_3)\right]^2+\left[N_4(\eta_1,P_3)-1\right]^2+\left[N_4(\eta_n,P_3)\right]^2\end{aligned} \tag{8.20}$$

where 5^{th} - 13^{th} terms in the above expression represent the sum of squares of the boundary conditions.

The problem is to minimize $\mathfrak{E}(P_1,P_2,P_3,P_4)$ by optimizing the biases and weights in the network for a given network configuration. The derivatives of the network output with respect to its input must be calculated in order to compute the error function $\mathfrak{E}(P_1,P_2,P_3,P_4)$. The derivatives of networks output $N_1(\eta_i,P_1)$, $N_2(\eta_i,P_2)$, $N_3(\eta_i,P_3)$ and $N_4(\eta_i,P_3)$ with respect to input vector η_i are calculated using Python package called autograd. Backpropagation can then be used to pursue the optimization by evaluating the derivatives of the loss function with respect to the network parameters. Here in this paper, we used a single hidden layer, Sigmoid activation function, the Adam optimizer [38] with an initial learning rate of 0.01.

To apply this method the semi-infinite domain of the given problem i.e. $[0,\infty]$ is reduced to $[\eta_1,\eta_\infty]$ where $\eta_1=0$, η_∞ is the parameter used to recover the boundary conditions at infinity. We start with training points that are chosen from the domain of the given problem i.e. $[0,\eta_\infty=10]$ and the weights and bias terms, which are generated randomly and we train the model to modify the parameters in the given domain of the problem.To ensure that the boundary conditions in the loss are integrated into each network parameter update, we use the entire set of training points. In general, we find that a single hidden layer with a small number of units is enough to get very exact results.

To check the convergence of the solution of the method, the dimensionless coefficient of skin friction ($f''(0)$), rate of heat transfer ($\theta'(0)$), Sherwood number ($\phi'(0)$) and density number of motile microorganisms ($\chi'(0)$) at the surface for $\beta=1.0$, $\lambda_C=1.0$, $\lambda_N=1.0$, $\lambda_T=1.0$, $Pr=1.0$, $Sc=0.2$, $Sb=0.1$, $Pe=0.1$, $\sigma_b=0.1$ and $S=0.5$ are calculated by

choosing different number of training points 50, 100 and 200 and different number of neurons 5, 8, 15 and 30 in the hidden layer and the computed results are presented in the Tables 8.1 and 8.2. It is evident from the Tables 8.1 and 8.2 that the solution has convergence of 10^{-4} when the Data points are 50 and Hidden neurons are 10.

Number Of Data Points	$f''(0)$	$\theta'(0)$	$\phi'(0)$	$\chi'(0)$
50	-0.15715565	-2.07466087	-0.69044626	-0.43214642
100	-0.15771369	-2.07352940	-0.69020583	-0.43241304
200	-0.16166460	-2.07419755	-0.69210441	-0.43234071

Table 8.1: "Convergence table for the values of $f''(0)$, $\theta'(0)$, $\phi'(0)$ and $\chi'(0)$ for $\beta = 1.0$, $\lambda_C = 1.0$, $\lambda_N = 1.0$, $\lambda_T = 1.0$, $Pr = 1.0$, $Sc = 0.2$, $Sb = 0.1$, $Pe = 0.1$, $\sigma_b = 0.1$ and $S = 0.5$ by the present method with different number of Hidden neurons and number of Data points fixed as 50."

Number Of Hidden Neurons	$f''(0)$	$\theta'(0)$	$\phi'(0)$	$\chi'(0)$
5	-0.22805518	-2.07872635	-0.70821418	-0.47023342
10	-0.15715565	-2.07466088	-0.69044626	-0.43214642
30	-0.15521094	-2.07464603	-0.69096449	-0.43062852

Table 8.2: "Convergence table for the values of $f''(0)$, $\theta'(0)$, $\phi'(0)$ and $\chi'(0)$ for $\beta = 1.0$, $\lambda_C = 1.0$, $\lambda_N = 1.0$, $\lambda_T = 1.0$, $Pr = 1.0$, $Sc = 0.2$, $Sb = 0.1$, $Pe = 0.1$, $\sigma_b = 0.1$ and $S = 0.5$ by the present method with different number of Data points and number of Neurons as 10."

8.4 Computational Results and Discussion

The effectiveness of the method is also validated by relating the current numerical results of the dimensionless coefficient of skin friction ($f''(0)$), rate of heat transfer ($\theta'(0)$), Sherwood number ($\phi'(0)$) and motile micro organism rate ($\chi'(0)$) are calculated using the shooting method in conjunction with the Runge-Kutta fourth order method. for $A = 0.5$, $S = 0.5$, $Pr = 1.0$, $Sc = 0.2$, $Sb = 0.1$, $P_e = 0.1$ and $\sigma_b = 0.1$. The computed results are presented in the Table 8.3. It is evident from the Table 8.3 that the present results are consistent with the results obtained by using shooting method.

	Present method	Shooting method
$f''(0)$	-0.15715565	-0.15333449
$\theta'(0)$	-2.07466087	-2.07500180
$\phi'(0)$	-0.69044625	-0.69021368
$\chi'(0)$	-0.43214642	-0.43037037

Table 8.3: "Comparison of the present method with the results of Shooting method."

Fig.8.2 illustrates the plot of error (between ANN method and Shooting technique results) in the values of f', θ, ϕ and χ for 11 equispaced positions in $[0, 10]$. The findings acquired by the current approach are in good agreement with the results obtained by the Shooting method, as shown in Fig.8.2.

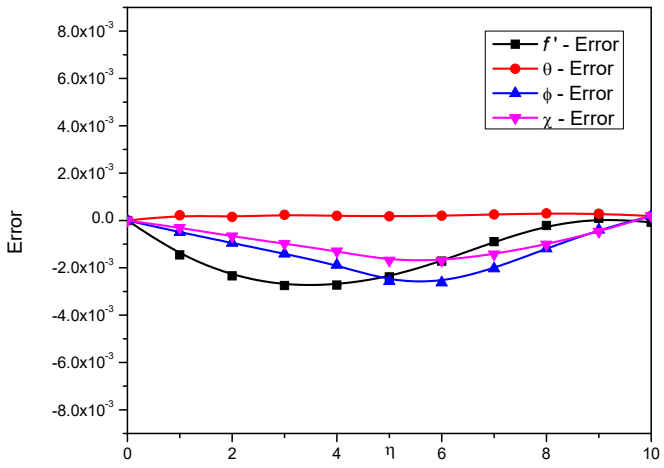

Figure 8.2: "Error plot between the results obtained by Artificial Neural Network method and Shooting method for the values of velocity, temperature, concentration and bioconvection profiles."

Figure 8.3 presents the effects of the concentration buoyancy parameter λ_C on the skin friction coefficient $(f''(0))$, Nusselt number $(-\theta'(0))$, Sherwood number $(-\phi'(0))$, and density number of motile microorganisms $(-\chi'(0))$ at fixed values of the other parameters discussed

above. Figures 8.3(a), 8.3(b), 8.3(c) and 8.3(d) show that as the concentration buoyancy parameter λ_C increases, skin friction, Nusselt number, Sherwood number, and density number of motile microorganisms increases.

Figure 8.4 illustrates the effects of the bioconvection buoyancy parameter λ_N on $f''(0)$, $-\theta'(0)$, $-\phi'(0)$ and $(-\chi'(0))$ with fixed values of the other factors discussed above. Figures 8.4(a), 8.4(b), 8.4(c) and 8.4(d) show that with rising values of the bioconvection buoyancy parameter λ_N, skin friction, Nusselt number, Sherwood number, and density number of motile microorganisms increases.

Figure 8.5 refers the influence of thermal buoyancy parameter λ_T on the coefficient of skin friction, Nusselt number, Sherwood number, and density number of motile microorganisms for fixed values of other parameters in the discussion as mentioned above. It is observed from figures 8.5(a), 8.5(b), 8.5(c) and 8.5(d) that skin friction, Nusselt number, Sherwood number, and density number of motile microorganisms are increasing for the increasing values of thermal buoyancy parameter λ_T.

The impacts of the bioconvection Peclet number P_e on $f''(0)$, $-\theta'(0)$, $-\phi'(0)$, and $-\chi'(0))$ for fixed values of the other parameters in the analysis are shown in Figure reffig6. Figures 8.6(a), 8.6(b), 8.6(c) and 8.6(d) reveal that for increasing values of bioconvection Peclet number P_e, skin friction, Nusselt number, Sherwood number are dropping, while density number of motile microorganisms is growing.

The effect of the parameter S on the skin friction coefficient, Nusselt number, Sherwood number, and density number of motile microorganisms under fixed values of the other constants in the conversation as indicated above are shown in Figure 8.7. Figures 8.7(a), 8.7(b), 8.7(c) and 8.7(d) show that for rising values of the suction / injection parameter S, skin friction is decreasing and Nusselt number, Sherwood number, density number of motile microorganisms are increasing.

Figure 8.8 depicts the impact of the bioconvection Schmith number Sb on $f''(0)$, $-\theta'(0)$, $-\phi'(0)$, and $-\chi'(0)$ at fixed values of the other parameters discussed above. Figures 8.8(a), 8.8(b), 8.8(c) and 8.8(d) show that with rising values of bioconvection Schmidth number

Sb skin friction, Nusselt number, Sherwood number reduce, while density number of motile microorganisms increase.

The consequences of the Schmith number Sc on skin friction ($f''(0)$), Nusselt number ($-\theta'(0)$), and Sherwood number ($-\phi'(0)$) given fixed values of the other parameters in the discussion as indicated above are shown in Figure 8.9. Figures 8.9(a), 8.9(b), and 8.9(c) show that for increasing values of Schmidth number Sc skin friction, Nusselt number decrease, while Sherwood number increase.

The influence of the non - dimensional bioconvection constant σ_b on skin friction ($f''(0)$), Nusselt number ($-\theta'(0)$), Sherwood number ($-\phi'(0)$), and density number of motile microorganisms ($-\chi'(0)$) with fixed values of all the other components in the study as indicated prior are shown in Figure 8.10. Figures 8.10(a), 8.10(b), 8.10(c) and 8.10(d) exhibit that for rising values of the dimensionless bioconvection constant σ_b, skin friction, Sherwood number, Nusselt number are reducing, while density number of motile microorganisms is growing.

8.5 Conclusions

The main goal of this study was to solve coupled nonlinear differential equations arising from the boundary layer flow of a Casson fluid across a vertically stretched sheet in the presence of bioconvection using an Artificial Neural Network technique. The influences of the parameters β, λ_C, λ_N, λ_T, Sc, Sb, Pe, σ_b and S on the relevant physical quantities are investigated. The important findings are presented below:

- With higher values of bioconvection Peclet number, suction / injection parameter, bioconvection Schmidth number, Schmidth number, and dimensionless bioconvection constant, skin friction coefficient decreases. It rises as the concentration buoyancy parameter, thermal buoyancy parameter, and bioconvection buoyancy parameter all rise in value.

- Nusselt number grows as concentration buoyancy parameter, thermal buoyancy pa-

rameter, bioconvection buoyancy parameter, and suction / injection parameter rise. It is reduced with increased values of the bioconvection Peclet number, bioconvection Schmidth number, Schmidth number, and dimensionless bioconvection constant.

- Sherwood number grows as concentration buoyancy parameter, thermal buoyancy parameter, bioconvection buoyancy parameter, Schmidth number and suction / injection parameter rise. It is reduced with increased values of the bioconvection Peclet number, bioconvection Schmidth number and dimensionless bioconvection constant.

- For all of the parameters specified in the study, the density number of motile microorganisms increases.

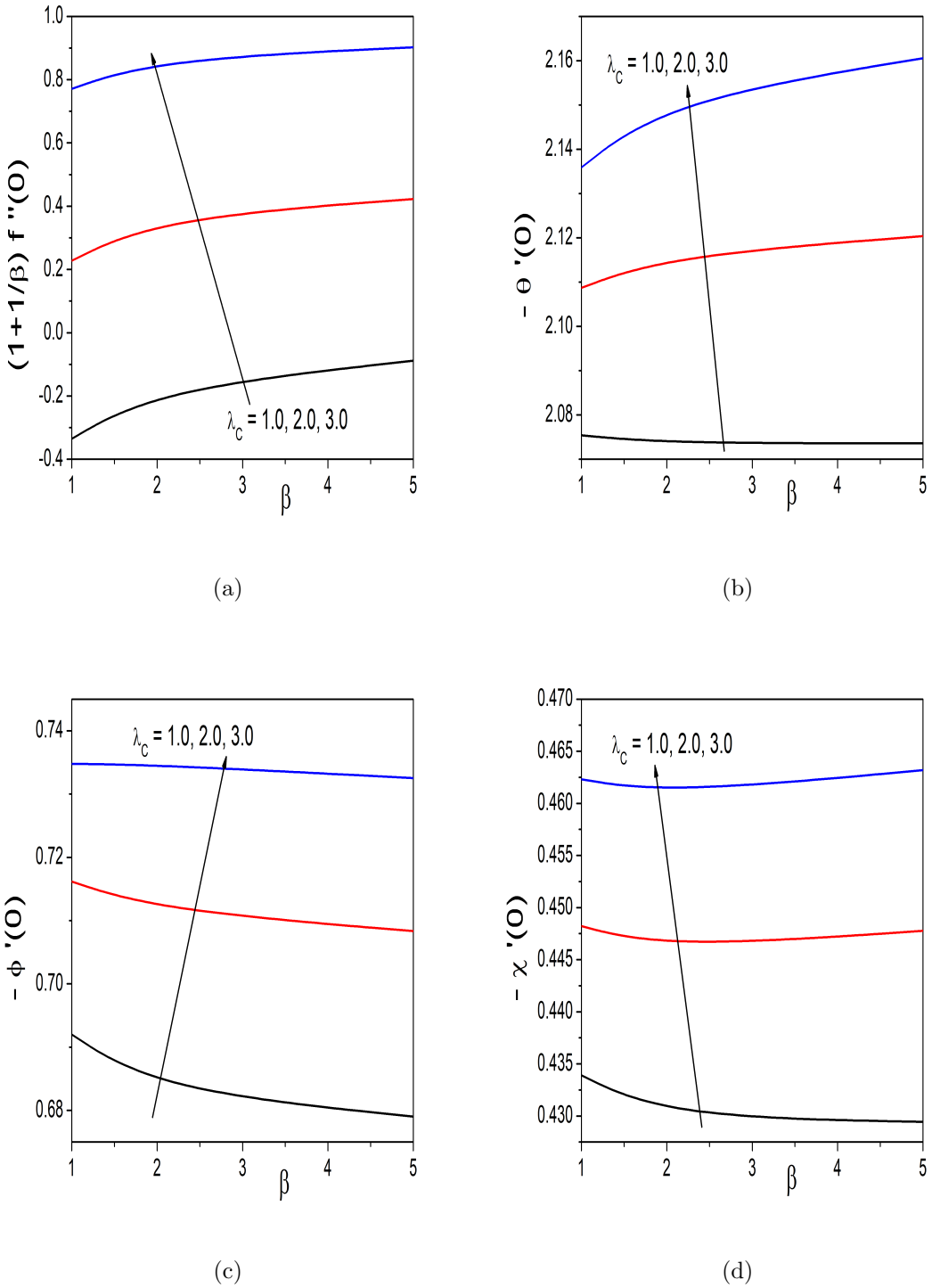

Figure 8.3: "Plots of $f''(0)$, $-\theta'(0)$, $-\phi'(0)$ and $-\chi'(0)$ for distinct values of concentration buoyancy parameter λ_C."

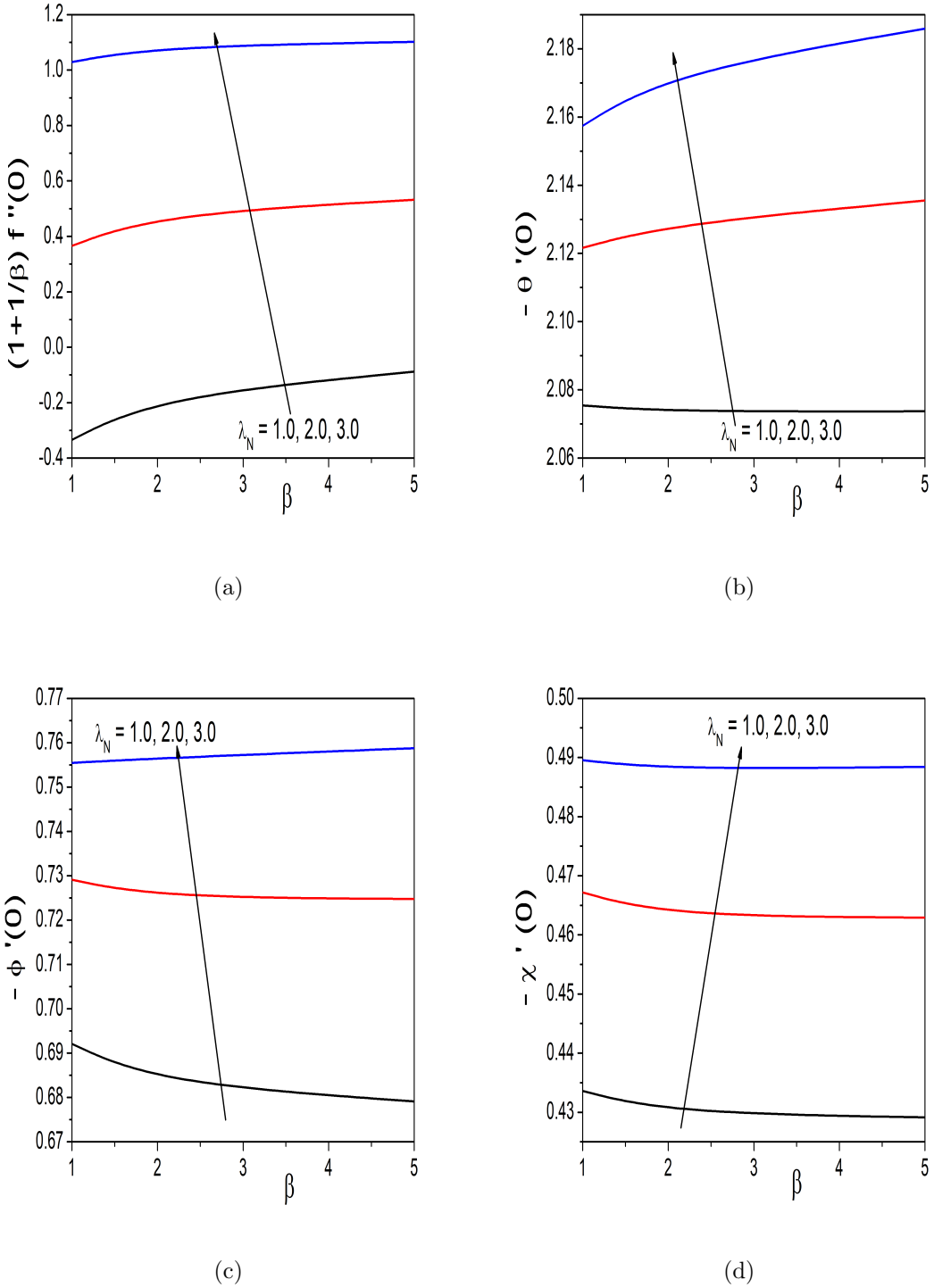

Figure 8.4: "Plots of $f''(0)$, $-\theta'(0)$, $-\phi'(0)$ and $-\chi'(0)$ for distinct values of bioconvection buoyancy parameter λ_N."

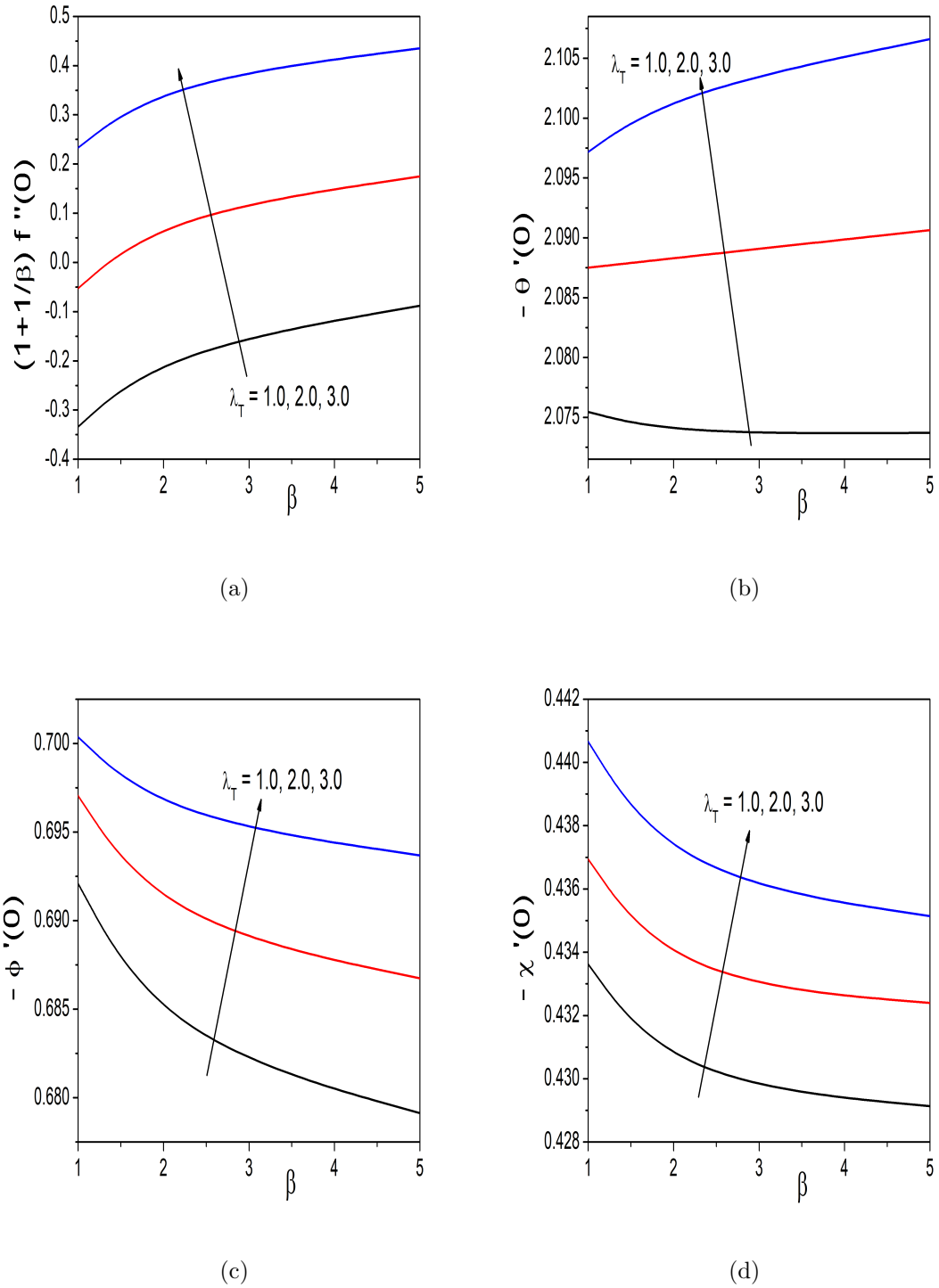

Figure 8.5: "Plots of $f''(0)$, $-\theta'(0)$, $-\phi'(0)$ and $-\chi'(0)$ for distinct values of thermal buoyancy parameter λ_T."

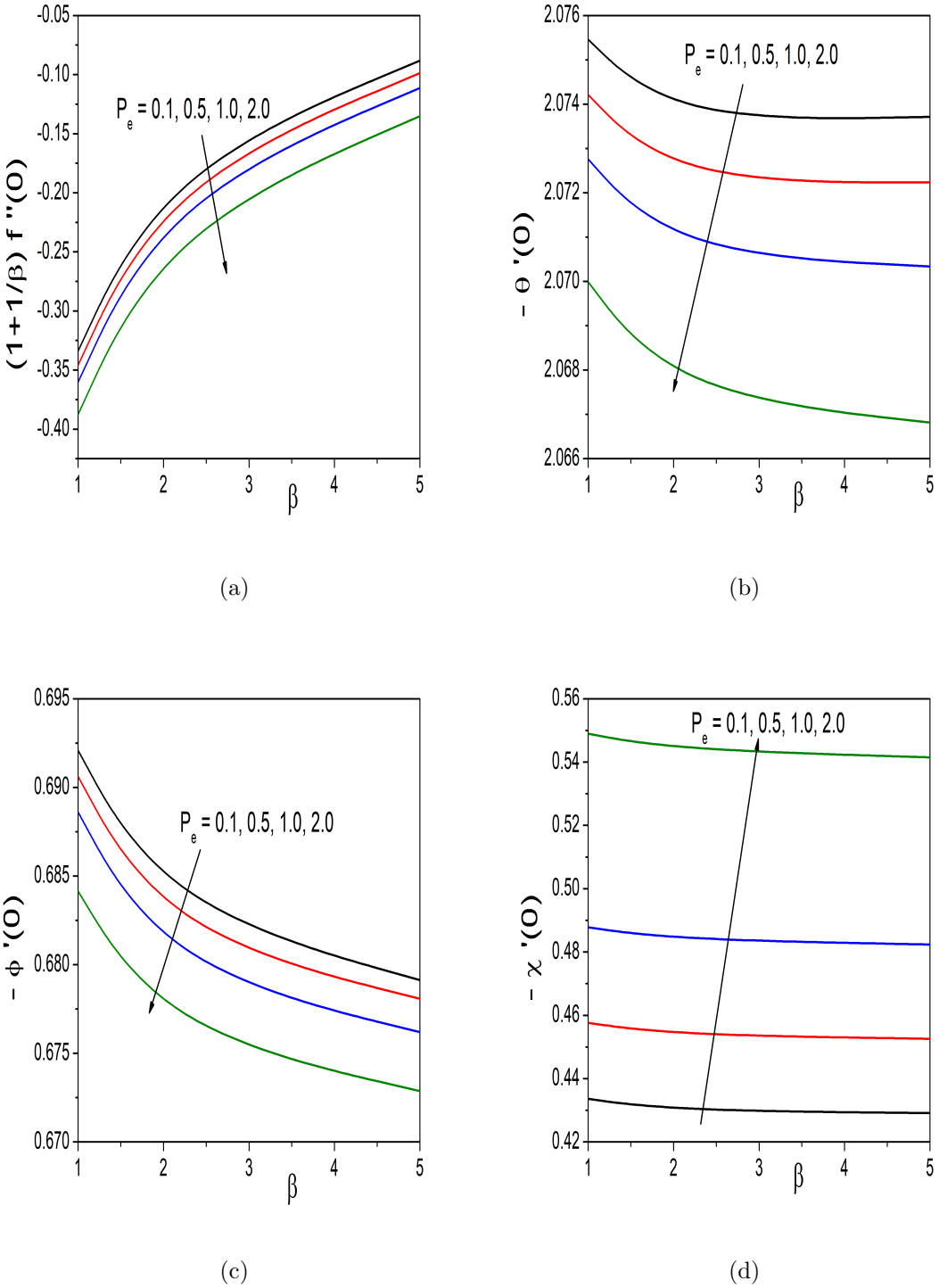

Figure 8.6: "Plots of $f''(0)$, $-\theta'(0)$, $-\phi'(0)$ and $-\chi'(0)$ for distinct values of bioconvection Peclet number P_e."

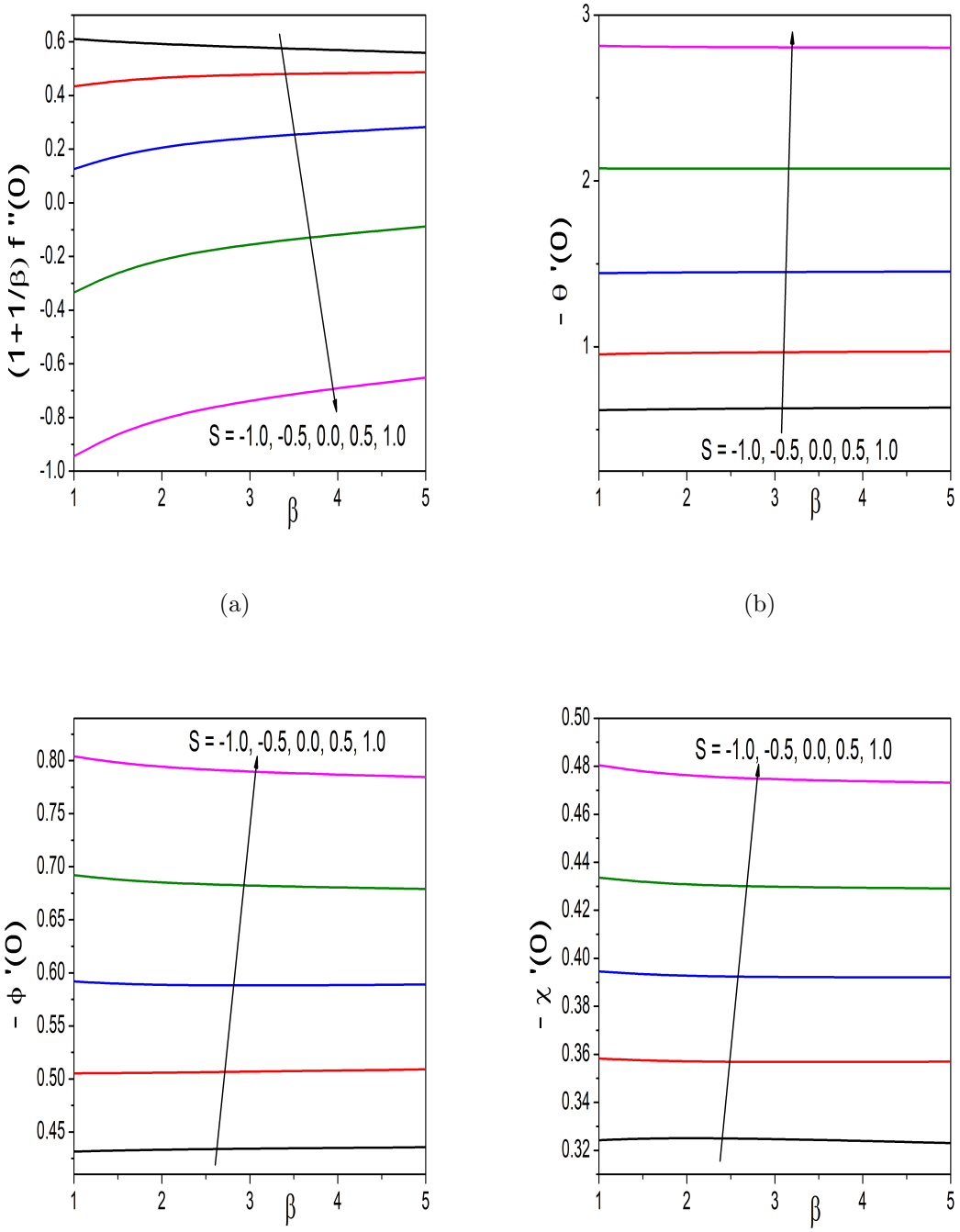

Figure 8.7: "Plots of $f''(0)$, $-\theta'(0)$, $-\phi'(0)$ and $-\chi'(0)$ for distinct values of suction/injection parameter S."

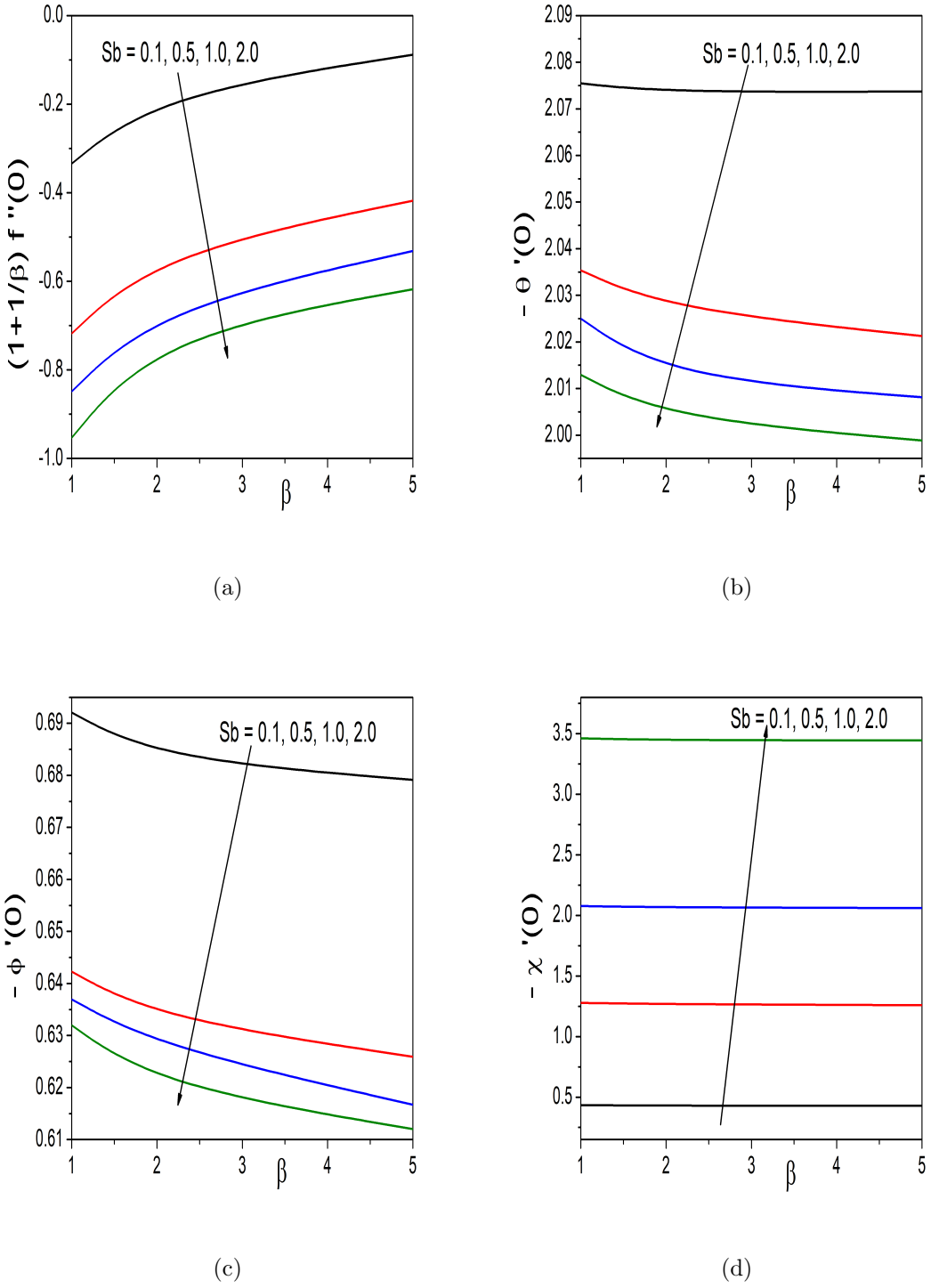

Figure 8.8: "Plots of $f''(0)$, $-\theta'(0)$, $-\phi'(0)$ and $-\chi'(0)$ for distinct values of bioconvection Schmidth number Sb."

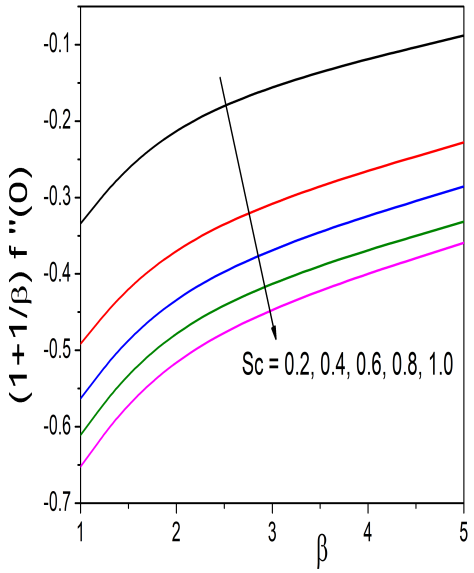

(a)

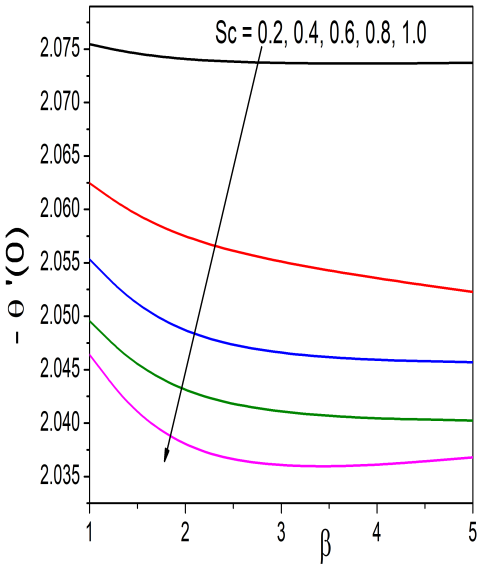

(b)

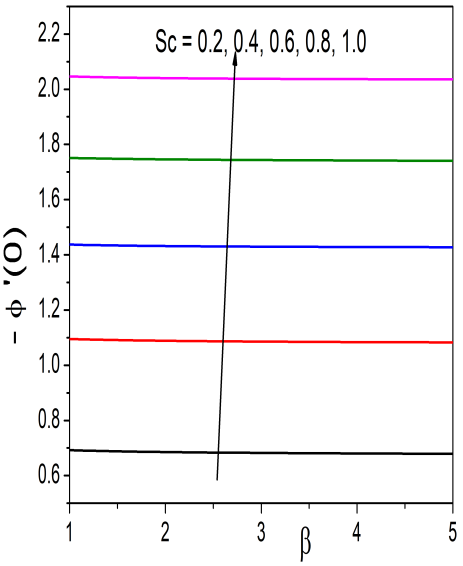

(c)

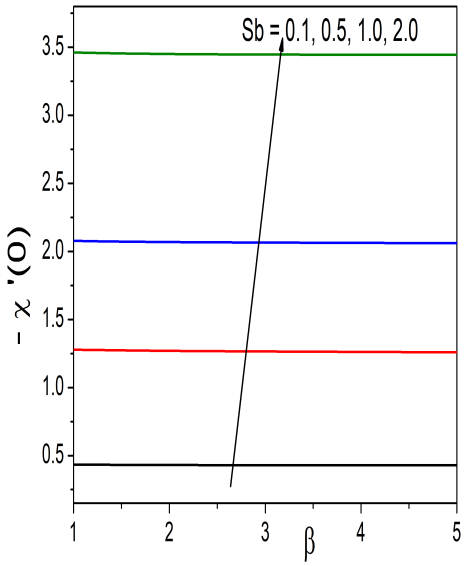

(d)

Figure 8.9: "Plots of $f''(0)$, $-\theta'(0)$ and $-\phi'(0)$ for distinct values of Schmidth number Sc."

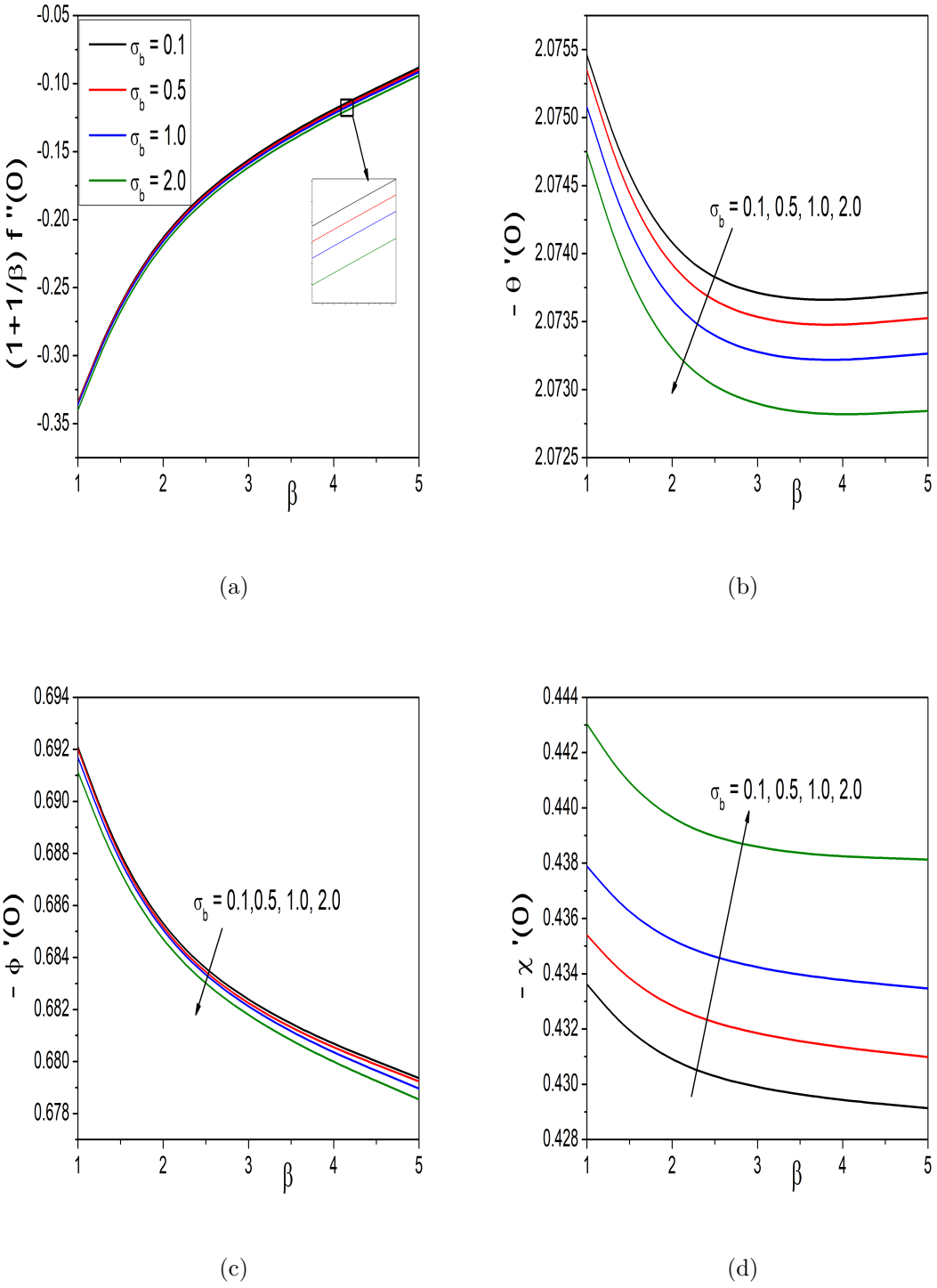

Figure 8.10: "Plots of $f''(0)$, $-\theta'(0)$, $-\phi'(0)$ and $-\chi'(0)$ for distinct values of dimensionless bioconvection constant σ_b."

Chapter 9

A Neural Network Method For Analyzing Entropy Generation in a Casson fluid Flow Over Radially Expanding Sheet With Magnetic and Viscous Dissipation Effects [1]

9.1 Introduction

The entropy generation in most industrial and technical phenomena results in the destruction of the available energy of the system. The entropy generation has a significant impact on the functioning of thermal equipment such as heat engines, power plants, heat pumps, refrigerators, and air conditioners.Hence, determining the rate of entropy generated for a system is critical in order to maximise the energy in the system for efficient operation. This aspect was proposed by Bejan[11, 12]. Many studies on the applicability of the second law of thermodynamics and entropy generation have been published in the literature.

[1]Communicated to "**Engineering Applications of Computational Fluid Mechanics**"

In this chapter the impacts of magnetic field and viscous dissipation on the entropy generation in a Casson fluid flow due to a radially extending sheet are investigated.

9.2 Formulation of the problem

Consider a steady, two dimensional, incompressible and laminar flow of a Casson fluid over a radially stretched surface at z = 0 as shown in Figure. 6.1.

The equations governing the flow are given by

$$\frac{\partial u}{\partial r}+\frac{u}{r}+\frac{\partial w}{\partial z}=0 \tag{9.1}$$

$$u\frac{\partial u}{\partial r}+w\frac{\partial u}{\partial z}=\nu(1+\frac{1}{\beta})\frac{\partial^2 u}{\partial z^2}-\frac{\sigma\, B_0^2}{\rho}u+g(\beta_T(T-T_\infty) \tag{9.2}$$

$$u\frac{\partial T}{\partial r}+w\frac{\partial T}{\partial z}=\frac{k}{\rho c_p}\frac{\partial^2 T}{\partial z^2}+\frac{\nu}{c_p}(1+\frac{1}{\beta})(\frac{\partial u}{\partial z})^2 \tag{9.3}$$

The associated boundary conditions are as follows:

$$\left.\begin{array}{ll} u=U_w,\, w=0,\, T=T_w=T_\infty+br \quad at \quad z=0 \\ u\to 0, \quad T\to T_\infty \qquad as \quad z\to\infty \end{array}\right\} \tag{9.4}$$

The quantities used in the above equations are defined in the previous chapters,

Introducing the stream function $\psi(r,z)$ through

$$u=-\frac{1}{r}\frac{\partial\psi}{\partial z} \quad \text{and} \quad w=\frac{1}{r}\frac{\partial\psi}{\partial r} \tag{9.5}$$

and the following similarity transformations

$$\psi(r,z)=-r^2U_w\mathrm{Re}^{-1/2}f(\eta), \quad \eta=\frac{z}{r}\mathrm{Re}^{1/2}, \quad \text{and} \quad \theta=\frac{T-T_\infty}{T_w-T_\infty} \tag{9.6}$$

Putting Eq, (9.6) in Eqs. (9.1) – (9.3), we obtained the momentum and heat equations (9.2) – (9.3) in their dimensionless from as follows

$$(1+\frac{1}{\beta})f'''+2ff''-(f')^2-Mf'+\lambda_T\theta=0 \tag{9.7}$$

$$\frac{1}{\mathrm{Pr}}\theta''+2f\theta'-f'\theta+(1+\frac{1}{\beta})Ec(f'')^2=0 \tag{9.8}$$

The boundary conditions given in Eq. (9.4) are transformed into the following form:

$$\begin{aligned} &f(\eta)=0, f'(\eta)=1, \theta(\eta)=1 \quad at \quad \eta=0 \\ &f'(\eta)\to 0 \; and \; \theta(\eta)\to 0 \quad as \quad \eta\to\infty \end{aligned} \tag{9.9}$$

where $M=\frac{\sigma B_0^2}{a\rho}$ is the magnetic parameter, $Ec=\frac{{U_w}^2}{c_p(T_w-T_\infty)}$ is the Eckret number,

The physical quantities of interest are the skin friction coefficient C_f and the Nusselt number N_u. In terms of dimensionless variables defined in Eq.(9.6) these quantities were changed to the following form:

$$\frac{1}{2}\sqrt{Re}C_f=(1+\frac{1}{\beta})f''(0) \quad and \quad \frac{N_u}{\sqrt{Re}}=-\theta'(0) \tag{9.10}$$

9.3 Entropy generation

The investigation of entropy creation is essential for understanding the irreversibility of thermal energy in a certain system. Entropy generation in most industrial and technical operations results in the destruction of the system's available energy. Thus, entropy formation has a significant impact on the functioning of thermal equipment such as heat engines, power plants, heat pumps, refrigerators, and air conditioners. Because of this, determining the rate of entropy generated for a system is critical in order to maximise the energy in the system for efficient operation. As per the second law of thermodynamics the relation for the entropy generation of the scheme associated with unsteady Casson fluid flow across the

radially stretched sheet in the presence of a magnetic field and chemical reaction is given by.

$$S_G = \frac{k}{T_\infty^2}\left(\frac{\partial T}{\partial z}\right)^2 + \frac{\mu}{T_\infty}\left(1+\frac{1}{\beta}\right)\left(\frac{\partial u}{\partial z}\right)^2 + \frac{\sigma\, B_0^2}{T_\infty}u^2 \tag{9.11}$$

The first term in the above expression reflects the entropy effect due to heat transfer, the second term denotes the entropy effect due to fluid friction, the third term symbolises the entropy impact caused by the magnetic field.

In terms of dimensionless variables the entropy generation has the form

$$Ns = \mathrm{Re}\left[(\theta')^2 + \frac{Br}{\Omega}\left(1+\frac{1}{\beta}\right)(f'')^2 + \frac{Br}{\Omega}M(f')^2\right] \tag{9.12}$$

where $Ns = \frac{S_G r^2 T_\infty^2}{k(T_w - T_\infty)^2}$ is the dimensionless entropy generation number, $Br = \frac{\mu U_w^2}{k(T_w - T_\infty)}$ is the Brinkman number, $\Omega = \frac{T_w - T_\infty}{T_\infty}$ is the dimensionless temperature.

9.4 Method of Solution

Consider a multilayered perceptron consisting of 3 – layers namely input layer - consisting of 'n' inputs $\bar{\eta}$=$(\eta_1, \eta_2, ...\eta_n)$, hidden layer - consisting of 'k' neurons and output layer consisting of two neurons $N_1(\eta_i, P_1)$ and $N_2(\eta_i, P_2)$ to estimate the solutions to two coupled ordinary differential equations as shown in the Fig. 9.1.

We take the network outputs $N_1(\eta_i, P_1)$ and $N_2(\eta_i, P_2)$ denote the trial solution for f and θ respectively with the adjustable parameters P_1 and P_2 respectively, which are given by the expressions

$$\left.\begin{aligned} N_1(\eta_i, P_1) &= \sum_{j=1}^{k} \varpi_{1j}^f \sigma\{\varpi_j^h \eta_i + b_j^h\} + b_1^f \\ N_2(\eta_i, P_2) &= \sum_{j=1}^{k} \varpi_{2j}^f \sigma\{\varpi_j^h \eta_i + b_j^h\} + b_2^f \end{aligned}\right\} \tag{9.13}$$

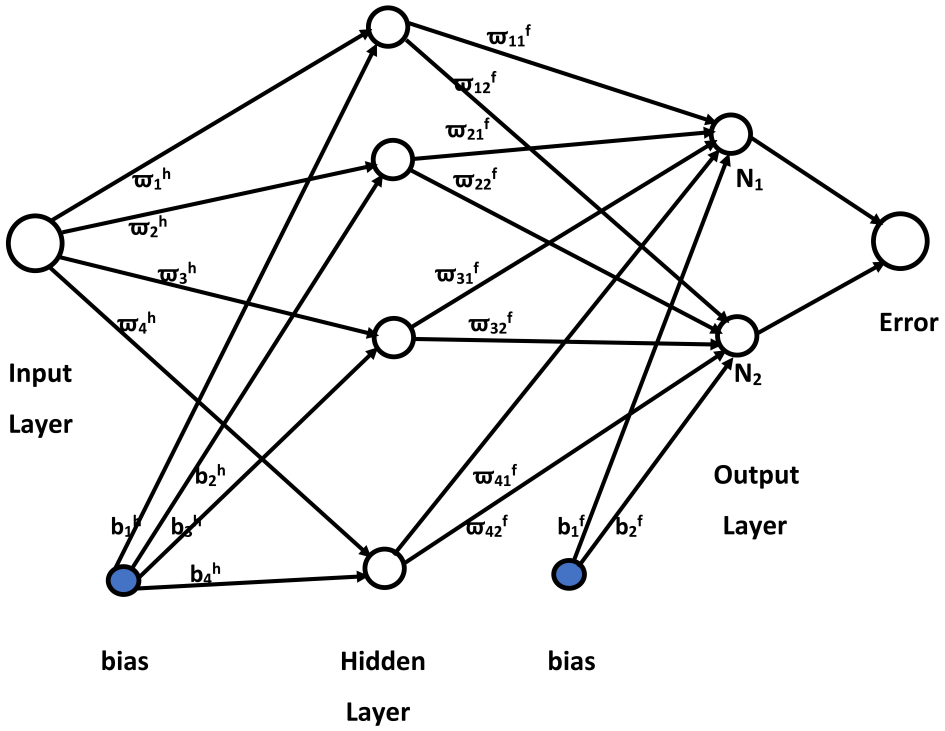

Figure 9.1: "Feed Forward Neural Network."

where, ϖ_j^h represents the weights from the input layer to the j^{th} hidden neuron, b_j^h is the bias term in the hidden layer, ϖ_{1j}^f is the weight from the j^{th} hidden neuron to the first output neuron, b_1^f is the bias term and ϖ_{2j}^f is the weight from the j^{th} hidden neuron to the second output neuron, b_2^f is the bias term. P_1 corresponds to the parameters ϖ_j^h, b_j^h, ϖ_{1j}^f, b_1^f and P_2 corresponds to the parameters ϖ_j^h, b_j^h, ϖ_{2j}^f and b_2^f respectively.

Since no data has been collected to learn from the differential equation, we have to insert Eq. (9.13) in the differential equations Eq.(9.7) and Eq. (9.8). Hence, we get

$$E_f = (1+\frac{1}{\beta}){N_1}'''(\eta_i, P_1) + 2N_1(\eta_i, P_1){N_1}''(\eta_i, P_1) - \left({N_1}'(\eta_i, P_1)\right)^2 + \lambda_T N_2(\eta_i, P_2) - M{N_1}'(\eta_i, P_1) \tag{9.14}$$

$$E_\theta = \frac{1}{Pr}{N_2}''(\eta_i, P_2) + 2N_1(\eta_i, P_1){N_2}'(\eta_i, P_2) - {N_1}'(\eta_i, P_1)N_2(\eta_i, P_2) + Ec(1+\frac{1}{\beta})N_2(\eta_i, P_2)^2 \tag{9.15}$$

where E_f and E_θ represents the errors or residuals with respect to the equations Eq. (9.7)

and Eq. (9.8) respectively. If the trial/constructed solutions for f and θ given in Eq. (9.13) are close to exact solution then the errors E_f and E_θ tend to zero. Similarly, the errors in the boundary conditions are given by:

$$N_1(\eta_1, P_1) = 0;\ N_1'(\eta_1, P_1) = 1;\ N_2(\eta_1, P_2) = 1;\ N_1'(\eta_n, P_1) = 0;\ N_2(\eta_n, P_2) = 0 \tag{9.16}$$

The mean square of error (MSE) is calculated by taking $1/n$ times the sum of the squared errors of differential equations (Eqs.(9.14) - (9.15)) along with the error in the boundary conditions Eq.(9.16) on the training set and then minimized. The solution produced by determining a set of biases and weights that minimizes the MSE (or loss function) after training is the final solution of the problem. Hence, the MSE or loss function $\mathfrak{E}(P_1, P_2)$ is given by

$$\begin{aligned}\mathfrak{E}(P_1, P_2) = \frac{1}{n}\sum_{i=1}^{n} (E_f)^2 + (E_\theta)^2 + [N_1(\eta_1, P_1)]^2 + [N_1'(\eta_1, P_1) - 1]^2 \\ +[N_1'(\eta_n, P_1)]^2 + [N_2(\eta_1, P_2) - 1]^2 + [N_2(\eta_n, P_2)]^2\end{aligned} \tag{9.17}$$

where 3^{rd} – 7^{th} terms represent error terms corresponding to the boundary conditions.

The problem is to minimize $\mathfrak{E}(P_1, P_2)$ by optimizing the biases and weights in the network for a given network configuration. The derivatives of the network output with respect to its input must be computed in order to compute the error $\mathfrak{E}(P_1, P_2)$. The derivative of networks output $N_1(\eta_i, P_1)$ and $N_2(\eta_i, P_2)$ with respect to input vector η_i are calculated using Python package called autograd. Backpropagation can then be used to pursue the optimization by evaluating the derivatives of the loss function with respect to the network parameters. Here in this paper, we used a single hidden layer, Sigmoid activation function, the Adam optimizer [38] with an initial learning rate of 0.01.

To apply this method the semi-infinite domain of the given problem i.e. $[0, \infty]$ is reduced to $[0, \eta_\infty]$ where η_∞ is a constant used to recover the conditions at infinity. We start with training points that are chosen from the domain of the given problem i.e. $[0, \eta_\infty]$ and the bias terms and weights, which are generated arbitrarily and train the model to modify

the parameters in the given domain of the problem. An ADAM optimizer [38] with an initial learning rate of 0.01 and one hidden layer is employed here along with the a Sigmoid activation function. The entire set of training points is used to ensure that the boundary conditions in the loss function are accounted for in the updating of each network parameter. It is found that one hidden layer with a minimal number of units is adequate for getting very exact results.

To check the convergence of the solution of the method, the dimensionless coefficient of skin friction ($f''(0)$) and rate of heat transfer ($\theta'(0)$) at the surface for $\beta = 1.0$, $Ec = 1.0$, $M = 1.0$, $Pr = 1.0$, $Re = 1.0$, $\frac{Br}{\Omega} = 1.0$ and $\lambda_T = 1.0$ are calculated by choosing different number of training points 50, 100 and 200 and different number of neurons 5, 10, 15 and 20 in the hidden layer and the computed results are presented in the Tables 9.1 and 9.2. It is evident from the Tables 9.1 and 9.2 that the solution has convergence of 10^{-4} when the Data points are 50 and Hidden neurons are 10.

Number Of Data points	$f''(0)$	$\theta'(0)$
50	-0.841338	-0.637062
100	-0.841312	-0.636997
200	-0.841283	-0.636962

Table 9.1: "Convergence table for the values of skin friction coefficient and Nusselt number at the surface for $\beta = 1.0$, $Ec = 1.0$, $M = 1.0$, $Pr = 1.0$, $Re = 1.0$, $\frac{Br}{\Omega} = 1.0$ and $\lambda_T = 1.0$ by the present method with different number of Data points."

Number Of Neurons	$f''(0)$	$\theta'(0)$
5	-0.8416367	-0.637278
10	-0.841338	-0.637062
15	-0.841303	-0.636998
20	-0.841324	-0.636878

Table 9.2: "Convergence table for the values of skin friction coefficient and Nusselt number at the surface for $\beta = 1.0$, $Ec = 1.0$, $M = 1.0$, $Pr = 1.0$, $Re = 1.0$, $\frac{Br}{\Omega} = 1.0$ and $\lambda_T = 1.0$ by the present method with different number of Hidden neurons."

9.5 Computational Results and Discussion

The efficacy of the ANN approach is demonstrated by comparing the present numerical findings for skin friction coefficient and rate of heat transfer coefficient to the values obtained utilising shooting method in association with the Runge-Kutta fourth order method for $\beta = 1.0$, $Ec = 1.0$, $M = 1.0$, $Pr = 1.0$, $Re = 1.0$, $\frac{Br}{\Omega} = 1.0$ and $\lambda_T = 1.0$. and presented in Table 9.3.

	Present method	Shooting method	Relative error
$f''(0)$	-0.841338	-0.84121022	1.27×10^{-4}
$\theta'(0)$	-0.637062	-0.63692850	1.33×10^{-4}

Table 9.3: "Comparison of the present method with the results of Shooting method."

Fig.9.2 illustrates the plot of error (between ANN method and Shooting technique results) in the values of f' and θ for 9 equispaced positions in $[0, 8]$. The findings acquired by the current approach are in excellent agreement with those obtained by the Shooting method, as shown in Fig.9.2.

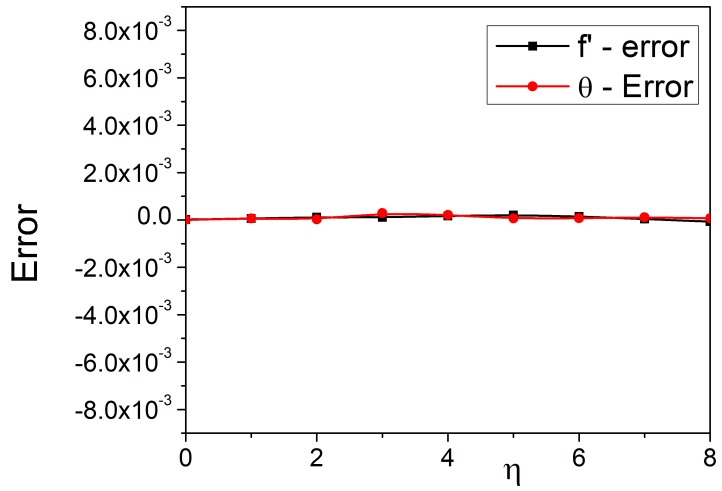

Figure 9.2: "Error plot between the results obtained by Artificial Neural Network method and Shooting method for the values of velocity and temperature profiles."

Figure 9.3 depicts the effects of Eckert number Ec on skin friction ($f''(0)$), Nusselt number

and entropy generation ($-\theta'(0)$) at fixed values of the other parameters discussed above. Figures 9.3(a) and 9.3(b) shows that as the thermal buoyancy parameter λ_T increases, skin friction is increasing and Nusselt number is decreasing. Whereas 9.3(c) reveals that the entropy generation is decreasing initially and increasing later for the increasing values of thermal buoyancy parameter.

Figure 9.4 illustrates the effects of the thermal buoyancy parameter λ_T on skin friction ($f''(0)$), Nusselt number ($-\theta'(0)$) and entropy generation with fixed values of the other factors discussed above. Figures 9.4(a), 9.4(b) shows that both skin friction, Nusselt number are increasing for the increasing values of thermal buoyancy parameter. 9.4(c) reveals that entropy generation is decreasing initially and increasing later with the increasing values of thermal buoyanvy parameter.

Figure 9.5 refers the effects of magnetic parameter M on skin friction ($f''(0)$), Nusselt number ($-\theta'(0)$) and entropy generation. It is observed from Figure 9.5(a) that entropy generation increasing initially and decreasing afterwards for the increase in magnetic parameter. Also Figures 9.5(b) and 9.5(c) shows that both skin friction and Nusselt number are decreasing for the increase in magnetic parameter M.

The consequences of the Prandtl number Pr on skin friction ($f''(0)$), Nusselt number ($-\theta'(0)$) and entropy generation given fixed values of the other parameters in the discussion as indicated above are shown in Figure 9.6. Figures 9.6(a) shows that entropy generation increasing initially and then decreasing later for the increasing values of Prandtl number Pr. Whereas skin friction is decreasing and Nusselt number is increasing for the increasing values of Prandtl number Pr as shown in Figure 9.6(b) and 9.6(c).

Fig. 9.7 reveals how the entropy generation has been effected by Casson fluid parameter β, Reynolds number Re and Brinkman number $\frac{Br}{\Omega}$. As the Brinkman number, Reynolds number increases entropy generation increases and it decreases when Casson fluid parameter β increase.

9.6 Conclusions

The entropy generation in a boundary layer flow of a Casson fluid across a radially stretching sheet in the presence of magnetic field and viscous dissipation effect using an Artificial Neural Network technique is presented. The influences of the parameters β, M, Pr, Ec, Re, $\frac{Br}{\Omega}$ and λ_T on the relevant physical quantities are investigated. The important findings are presented below:

- Skin friction is increasing for the increasing values of thermal buoyancy parameter, Eckert number and it decreases as the magnetic parameter, Prandtl number increase.
- Nusselt number increases as the thermal buoyancy parameter, Prandtl number increase and it decreases as the magnetic parameter, Eckert number increase.
- For rising values of thermal buoyancy parameter, Eckert number entropy generation decreases initially and eventually increases and the reverse trend is observed when magnetic parameter, Prandtl number increase.

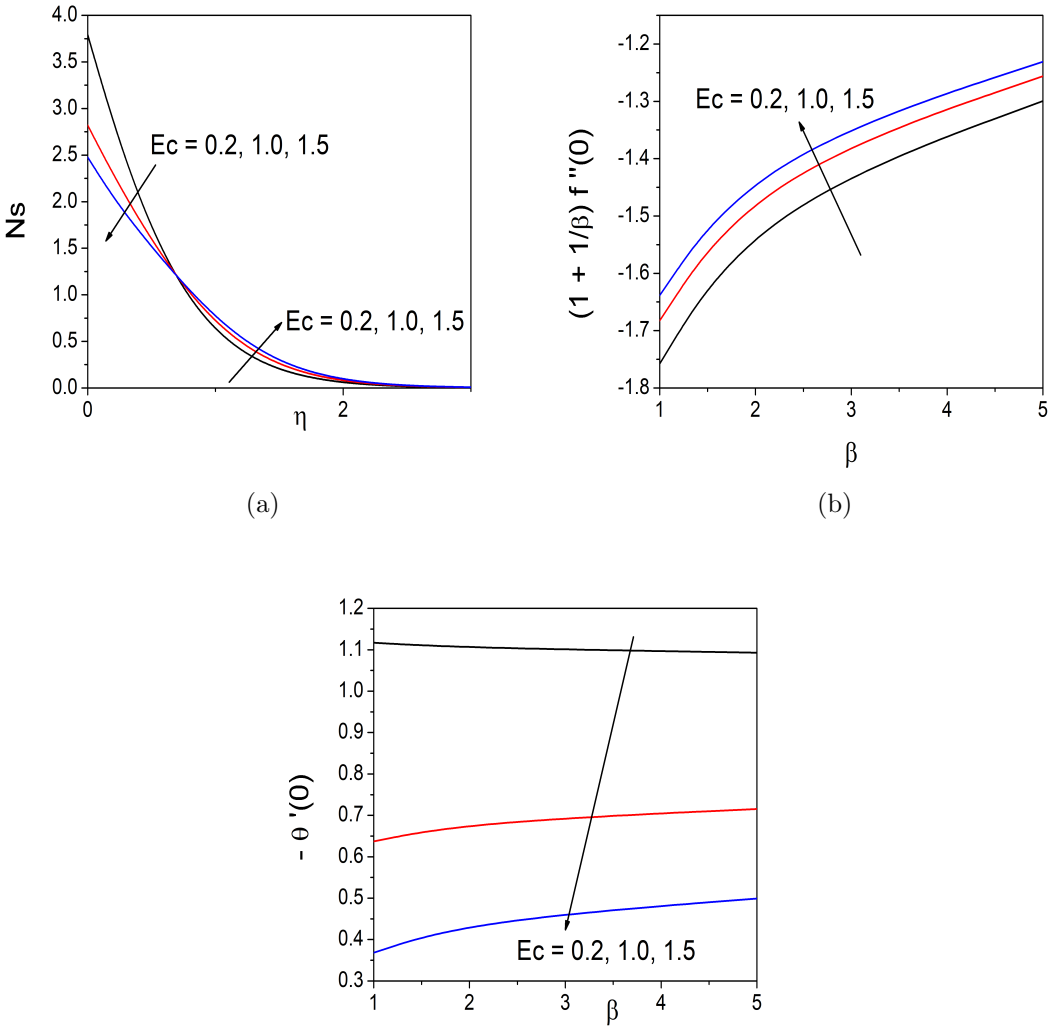

(a) (b)

(c)

Figure 9.3: "The variation of skin friction coefficient, Nusselt number and Entropy Generation with Eckert number Ec."

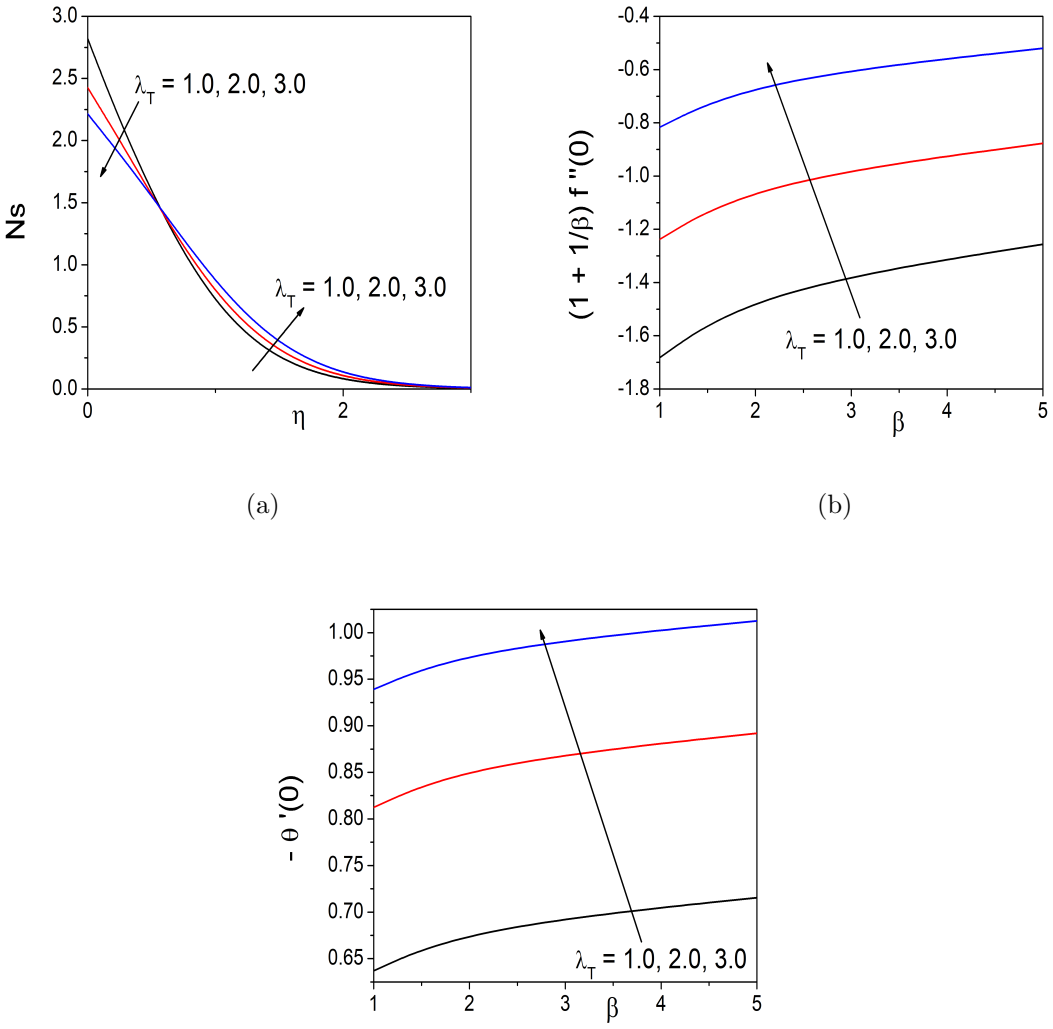

(a) (b)

(c)

Figure 9.4: "The variation of skin friction coefficient, Nusselt number and Entropy Generation with thermal buoyancy parameter λ_T."

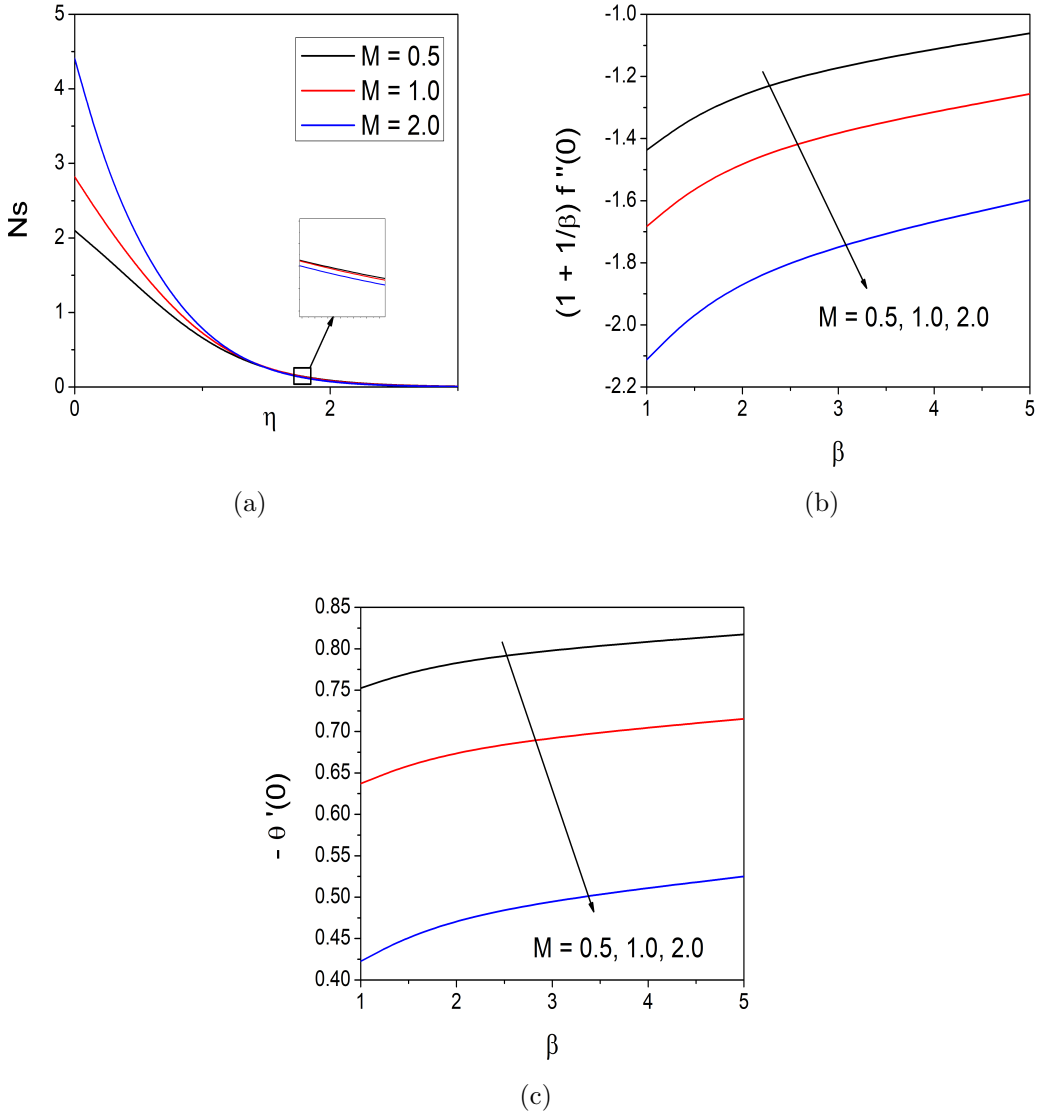

Figure 9.5: "The variation of skin friction coefficient, Nusselt number and Entropy Generation with magnetic parameter M."

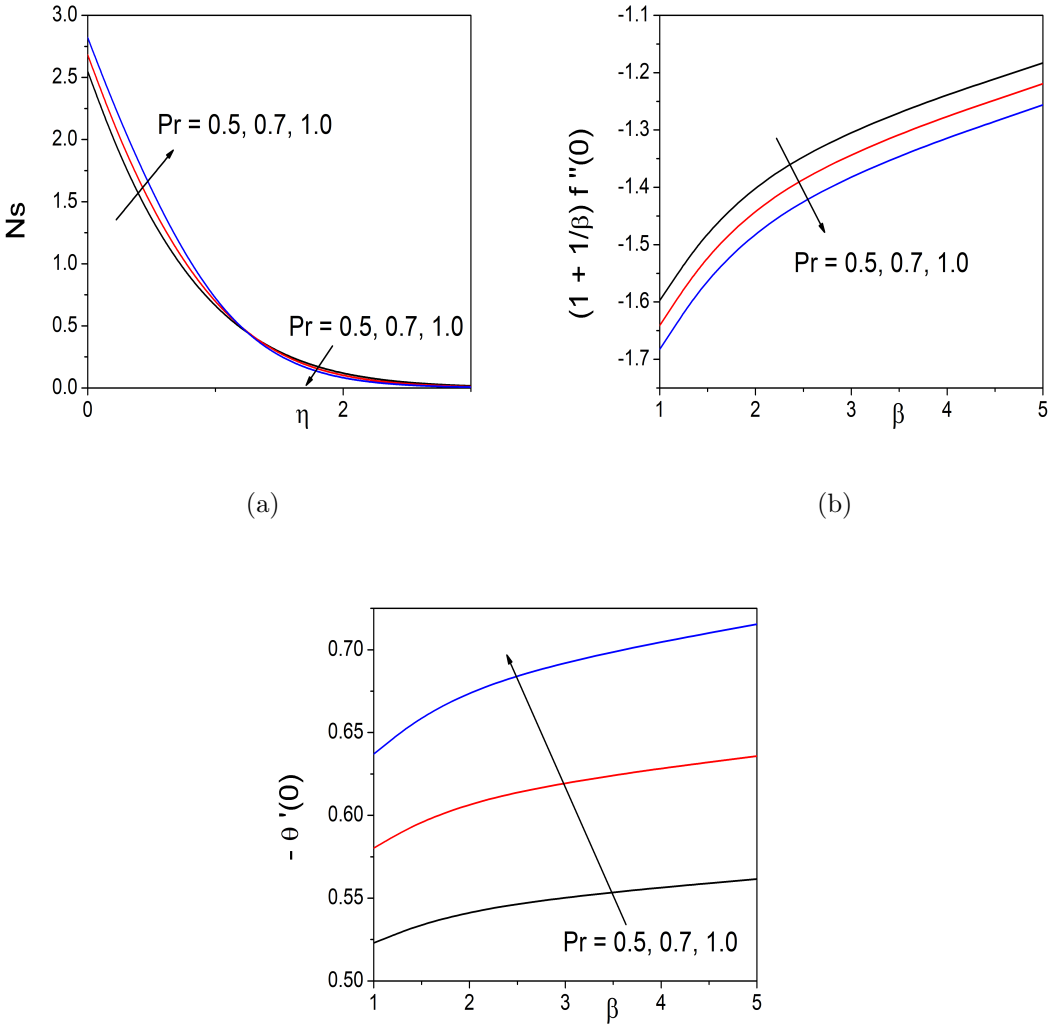

(a)

(b)

(c)

Figure 9.6: "The variation of skin friction coefficient, Nusselt number and Entropy Generation with Prandtl number Pr."

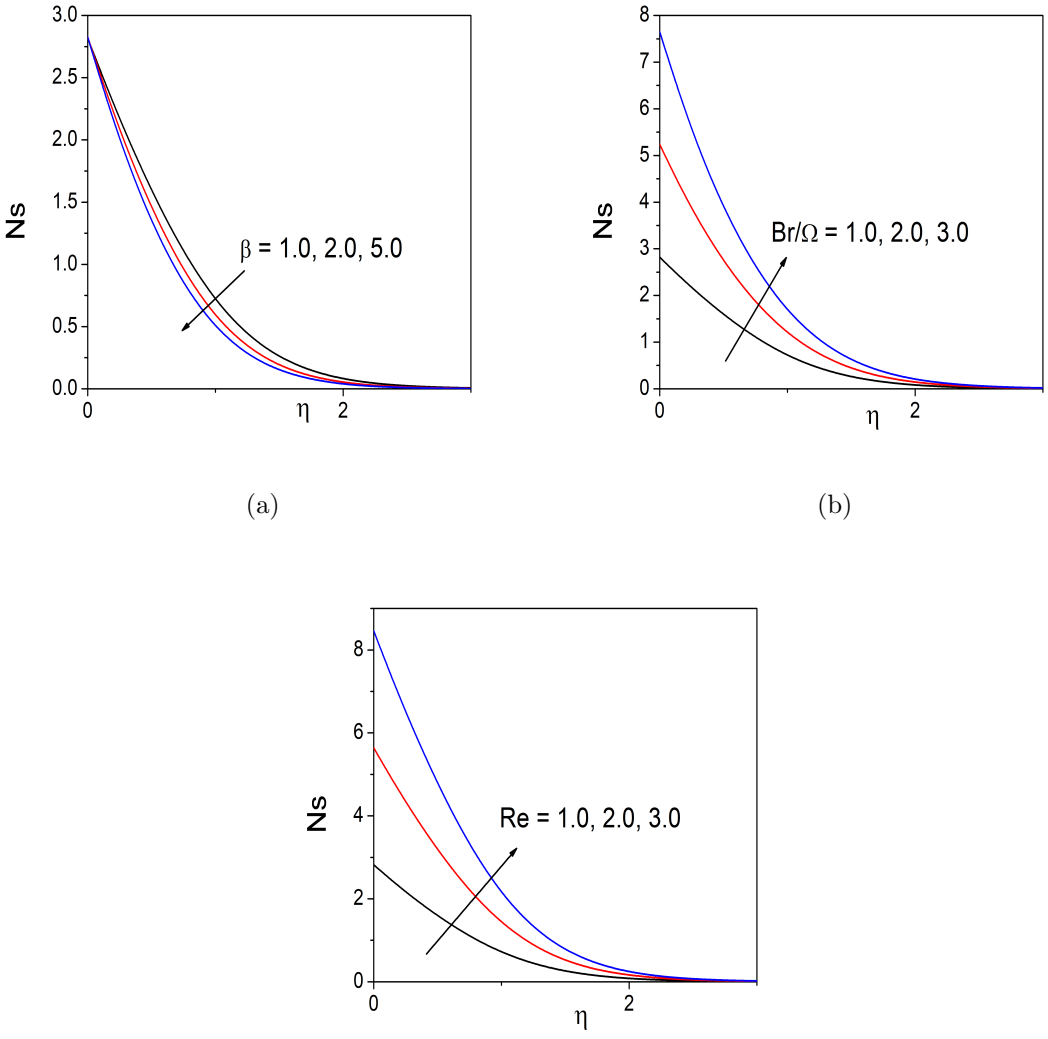

(a) (b)

(c)

Figure 9.7: "The variation of Entropy Generation with β, $\frac{Br}{\Omega}$ and Re."

Chapter 10

Summary and Conclusions

In this thesis, the artificial neural network method is used to study the flow of a Casson fluid over a radially expanding sheet under both steady and unstable conditions.

Employing similarity transformations, the equations describing the flow in Chapters 2 through Chapter 9 are reduced into a set of nonlinear ODEs. The resulting non-linear ODEs were solved using Artificial Neural Network method. The impacts of different geometrical and hydrodynamic parameters are illustrated in graphs and analysed with regard to the coefficient of skin friction, heat transfer rate (in terms of Nusselt number), mass transfer rate (in terms of Sherwood number) and density number of motile microorganisms.

Part II investigates the Casson fluid flow across an unsteady radially stretched sheet by including the effectsof suction / injection, magnetic field, cross diffusion, viscou dissipation and chemical reaction. The important observations made from this study are listed below :

- Unsteadiness parameter decreases the skin friction, whereas it increases the Nusselt number, Sherwood number and density number of motile microorganisms. Entropy generation enhances initially later decreases for the unsteadiness parameter.
- An increase in Dufour number rises the Sherwood number but decreases the Nusselt number.

- As chemical reaction parameter increase Nusselt number decreases and Sherwood number increase. Entropy generation enhances initially later decreases for the chemical reaction parameter.

- The magnetic parameter decreases skin friction coefficient, heat transfer rate as well as the mass transfer rate. Entropy generation enhances initially later decreases for the magnetic parameter.

- As the bioconvection Peclet number increase, both the heat and mass transfer rates decrease, whereas the density number of motile microorganisms increase.

- The Nusselt number, Sherwood number and density number of motile microorganisms increases with the suction / injection parameter, but the skin friction coefficient decreases.

- An enhancement in bioconvection Schmidth number enhances the skin friction coefficient, Nusselt number and density number of motile microorganisms, whereas the Sherwood number increases initially and reduces later with the bioconvection Schmidth number.

- The Soret number increases the Nusselt number and decreases the Sherwood number.

Part-III deals with the flow of the fluid over a steady radially stretching sheet. The objective of this part is to study the effects of Casson fluid parameter, Eckret number, suction / injection parameter, magnetic parameter, radiation parameter, chemical reaction parameter, thermal buoyancy parameter, concentration buoyancy parameter, bioconvection buoyancy parameter, Schmidth number, bioconvection Schmidth number, dimensionless bioconvection constant and bioconvection Peclet number on velocity, temperature, concentration, skin friction coefficient, Nusselt number, Sherwood number, density number of motile microorganisms and entropy generation. The important observations made from this study are listed below :

- Eckert number improves the skin friction coefficient but it declines the Nusselt number.

- The chemical reaction parameter reduces the skin friction coefficient as well as Nusselt number.
- The enhancement in thermal buoyancy parameter, concentration buoyancy parameter, bioconvection buoyancy parameter causes the increment in skin friction coefficient, Nusselt number, Sherwood number and density number of motile microorganisms.
- Skin friction and the Nusselt number both diminish when a magnetic parameter is enhanced..
- The bioconvection Peclet number reduces skin friction, Nusselt number and Sherwood number, but it improves the density number of motile microorganisms.
- An increment in radiation parameter raises both the skin friction and Nusselt number.
- The suction / injection parameter enhances the Nusselt number, Sherwood number and density number of motile microorganisms, whereas it reduces the skin friction.
- For the increased values of Schmidth number the Sherwood number increases while skin friction and Nusselt number decreases.
- The bioconvection Schmidth number declines the skin friction, Nusselt number and Sherwood number,but it improves the density number of motile microorganisms.

The work presented in the thesis can be extended to analyze the various effects like Hall effect, Hall and Ion slip, etc. Further, this work can be extended by studying the analysis in other non-Newtonian fluids like Jeffrey fluids, Power-law fluids, and the geometry can be changed to an oscillatory vertical plate, inclined plate, and through pipes. This work can also be extended to porous media.

In the recent past, the study of Physics Informed Neural Networks (PINN) has attracted the curiosity of many researchers. Thus, the work presented in the thesis can be extended to use the PINNs to solve the fluid flow problems.

Bibliography

[1] Abd El-Aziz, M., and Afify, A. A. Mhd casson fluid flow over a stretching sheet with entropy generation analysis and hall influence. *Entropy 21*, 6 (2019), 592.

[2] Adomian, G. *Solving Frontier Problems of Physics: The Decomposition Method*. 1993.

[3] Afify, A. A. The influence of slip boundary condition on casson nanofluid flow over a stretching sheet in the presence of viscous dissipation and chemical reaction. *Mathematical Problems in Engineering 2017* (2017).

[4] Ahmed, J., Shahzad, A., Begum, A., Ali, R., and Siddiqui, N. Effects of inclined lorentz forces on boundary layer flow of sisko fluid over a radially stretching sheet with radiative heat transfer. *Journal of the Brazilian Society of Mechanical Sciences and Engineering 39*, 8 (2017), 3039–3050.

[5] Akhmet, M. U., Aruğaslan, D., and Cengiz, N. Exponential stability of periodic solutions of recurrent neural networks with functional dependence on piecewise constant argument. *Turkish Journal of Mathematics 42* (2018), 272–292.

[6] Alkasasbeh, H. T., Abu-Ghurra, S., and Alzgool, H. A. Similarity solution of heat transfer for the upper-convected maxwell casson fluid over a stretching/shrinking sheet with thermal radiation. *JP Journal of Heat and Mass Transfer 16*, 1 (2019), 1–17.

[7] Ariel, P. D. Axisymmetric flow due to a stretching sheet with partial slip. *Computers & Mathematics with Applications 54*, 7-8 (2007), 1169–1183.

[8] Awais, M., Raja, M. A. Z., Awan, S. E., Shoaib, M., and Ali, H. M. Heat and mass transfer phenomenon for the dynamics of casson fluid through porous medium over shrinking wall subject to lorentz force and heat source/sink. *Alexandria Engineering Journal 60*, 1 (2021), 1355–1363.

[9] Babu, M. J., and Sandeep, N. Effect of nonlinear thermal radiation on non-aligned bio-convective stagnation point flow of a magnetic-nanofluid over a stretching sheet. *Alexandria Engineering Journal 55*, 3 (2016), 1931–1939.

[10] Behrang, M., Ghalambaz, M., Assareh, E., and Noghrehabadi, A. A new solution for natural convection of darcian fluid about a vertical full cone embedded in porous media prescribed wall temperature by using a hybrid neural network-particle swarm optimization method. *World Academy of Science, Engineering and Technology 49* (2011), 1098–1103.

[11] Bejan, A. Second-law analysis in heat transfer and thermal design. In *Advances in heat transfer*, vol. 15. Elsevier, 1982, pp. 1–58.

[12] Bejan, A., and Kestin, J. Entropy generation through heat and fluid flow.

[13] Casson, N. A flow equation for pigment-oil suspensions of the printing ink type. *In: Rheology of disperse systems, Mill CC (Ed.)*.

[14] Chakraverty, S., and Mall, S. *Artificial neural networks for engineers and scientists: solving ordinary differential equations*. CRC Press, 2017.

[15] Chedjou, J. C., and Kyamakya, K. A novel general and robust method based on naop for solving nonlinear ordinary differential equations and partial differential equations by cellular neural networks. *Journal of Dynamic Systems, Measurement, and Control 135* (2013), 031014.

[16] Crane, L. Flow past a stretching plate. *Zeitschrift für angewandte Mathematik und Physik ZAMP 21* (1970), 645–647.

[17] Devi, R. L., Poply, V., and Mani, M. Effect of aligned magnetic field and inclined outer velocity in casson fluid flow over a stretching sheet with heat source. *Journal of Thermal Engineering 7*, 4 (2021), 823–844.

[18] Eckert, E. R. G., and Drake Jr, R. M. Analysis of heat and mass transfer.

[19] El-Aziz, A., Afify, A. A., et al. Influences of slip velocity and induced magnetic field on mhd stagnation-point flow and heat transfer of casson fluid over a stretching sheet. *Mathematical Problems in Engineering 2018* (2018).

[20] Elayarani, M., and Shanmugapriya, M. Artificial neural network modeling of mhd stagnation point flow and heat transfer towards a porous stretching sheet. In *AIP Conference Proceedings* (2019), vol. 2161, AIP Publishing LLC, p. 020043.

[21] Faraz, F., Haider, S., and Imran, S. M. Study of magneto-hydrodynamics (mhd) impacts on an axisymmetric casson nanofluid flow and heat transfer over unsteady radially stretching sheet. *SN Applied Sciences 2*, 1 (2020), 1–17.

[22] Faraz, F., Imran, S. M., Ali, B., and Haider, S. Thermo-diffusion and multi-slip effect on an axisymmetric casson flow over a unsteady radially stretching sheet in the presence of chemical reaction. *Processes 7*, 11 (2019), 851.

[23] Gireesha, B. J., Shankaralingappa, B. M., Prasannakumar, B. C., and Nagaraja, B. Mhd flow and melting heat transfer of dusty casson fluid over a stretching sheet with cattaneo–christov heat flux model. *International Journal of Ambient Energy* (2020), 1–9.

[24] Hamid, M., Usman, M., Khan, Z. H., Ahmad, R., and Wang, W. Dual solutions and stability analysis of flow and heat transfer of casson fluid over a stretching sheet. *Physics Letters A 383*, 20 (2019), 2400–2408.

[25] Hayat, T., Shehzad, S., and Alsaedi, A. Soret and dufour effects on magneto-hydrodynamic (mhd) flow of casson fluid. *Applied Mathematics & Mechanics 33*, 10 (2012).

[26] He, J. H. A new approach to nonlinear partial differential equations. *Communications in Nonlinear Science and Numerical Simulation 2*, 4 (1997), 230–235.

[27] He, J. H. Some new approaches to duffing equation with strongly and high order nonlinearity (ii) parametrized perturbation technique. *Communications in Nonlinear Science and Numerical Simulation 4* (1999), 78–80.

[28] He, J. H. Homotopy perturbation method for bifurcation of nonlinear problems. *International Journal of Nonlinear Sciences and Numerical Simulation 6* (2005), 207–208.

[29] Hornik, K., Stinchcombe, M., and White, H. Multilayer feedforward networks are universal approximators. *Neural Networks 2* (1989), 359–366.

[30] Hornik, K., Stinchcombe, M., and White, H. Universal approximation of an unknown mapping and its derivatives using multilayer feedforward networks. *Neural Networks 3* (1990), 551–560.

[31] Hsu, C. H., and Yang, S. Y. On camel-like traveling wave solutions in cellular neural networks. *Journal of Differential Equations 196*, 2 (2004), 481–514.

[32] Hussanan, A., Salleh, M. Z., Alkasasbeh, H. T., and Khan, I. Mhd flow and heat transfer in a casson fluid over a nonlinearly stretching sheet with newtonian heating. *Heat transfer research 49*, 12 (2018).

[33] Ibrahim, S., Lorenzini, G., Kumar, P. V., and Raju, C. S. K. Influence of chemical reaction and heat source on dissipative mhd mixed convection flow of a casson nanofluid over a nonlinear permeable stretching sheet. *International Journal of Heat and Mass Transfer 111* (2017), 346–355.

[34] Kameswaran, P. K., Shaw, S., and Sibanda, P. Dual solutions of casson fluid flow over a stretching or shrinking sheet. *Sadhana 39* (2014), 1573–1583.

[35] Khan, M., Manzur, M., and Rahman, M. On axisymmetric flow and heat transfer of cross fluid over a radially stretching sheet. *Results in physics 7* (2017), 3767–3772.

[36] Khan, M. I., Waqas, M., Hayat, T., and Alsaedi, A. A comparative study of casson fluid with homogeneous-heterogeneous reactions. *Journal of colloid and interface science 498* (2017), 85–90.

[37] Khan, S. A., Nie, Y., and Ali, B. Multiple slip effects on magnetohydrodynamic axisymmetric buoyant nanofluid flow above a stretching sheet with radiation and chemical reaction. *Symmetry 11*, 9 (2019), 1171.

[38] Kingma, D. P., and Ba, J. Adam: A method for stochastic optimization. *arXiv preprint arXiv:1412.6980* (2014).

[39] Kumar, G. V., Kumar, R., and Varma, S. V. K. Multiple slips and chemical reaction effects on mhd stagnation point flow of casson fluid over a stretching sheet with viscous and joules heating. *Frontiers in Heat and Mass Transfer 10* (2018).

[40] Lagaris, I. E., Likas, A., and Fotiadis, D. I. Artificial neural networks for solving ordinary and partial differential equations. *IEEE transactions on neural networks 9*, 5 (1998), 987–1000.

[41] Lee, H., and Kang, I. S. Neural algorithm for solving differential equations. *Journal of Computational Physics 91*, 1 (1990), 110–131.

[42] Li, J., Luo, S., Qi, Y., and Haung, Y. Numerical solution of elliptic partial differential equation using radial basis function neural networks. *Neural networks : the official journal of the International Neural Network Society 16* (2003), 729–34.

[43] Li, X., and Song, S. Impulsive control for existence, uniqueness, and global stability of periodic solutions of recurrent neural networks with discrete and continuously distributed delays. *IEEE Transactions on Neural Networks and Learning Systems 24*, 6 (2013), 868–877.

[44] Liao, S. Homotopy analysis method: A new analytical technique for nonlinear problems. *Communications in Nonlinear Science and Numerical Simulation 2*, 2 (1997), 95–100.

[45] Mabood, F., and Das, K. Outlining the impact of melting on mhd casson fluid flow past a stretching sheet in a porous medium with radiation. *Heliyon 5*, 2 (2019), e01216.

[46] Magagula, V. M., Shaw, S., and Kairi, R. R. Double dispersed bioconvective casson nanofluid fluid flow over a nonlinear convective stretching sheet in suspension of gyrotactic microorganism. *Heat Transfer 49*, 5 (2020), 2449–2471.

[47] Majeed, K., Masood, Z., Samar, R., and Zahoor, R. M. A. A genetic algorithm optimized morlet wavelet artificial neural network to study the dynamics of nonlinear troesch's system. *Applied Soft Computing 56* (07 2017), 420–435.

[48] Meade, A. J., and Fernandez, A. A. The numerical solution of linear ordinary differential equations by feedforward neural networks. *Mathematical and Computer Modelling 19*, 12 (1994), 1–25.

[49] Meade Jr, A. J., and Fernandez, A. A. Solution of nonlinear ordinary differential equations by feedforward neural networks. *Mathematical and Computer Modelling 20*, 9 (1994), 19–44.

[50] Mouli, G. B., Gangadhar, K., and Raju, B. On spectral relaxation approach for thermal diffusion and diffusion thermo effects on viscous dissipative casson fluid through a stretched surface. *International Journal of Applied and Computational Mathematics 6*, 6 (2020), 1–21.

[51] Mutuk, H. A neural network study of blasius equation. *Neural Processing Letters 51*, 3 (2020), 2179–2194.

[52] Nagaraja, B., and Gireesha, B. Exponential space-dependent heat generation impact on mhd convective flow of casson fluid over a curved stretching sheet with chemical reaction. *Journal of Thermal Analysis and Calorimetry 143* (2021), 4071–4079.

[53] Naidu, K. K., Babu, D. H., and Narayana, P. V. S. Bioconvection in magneto hydrodynamics casson nanoliquid (fe3o4-sodium alginate) with gyrotactic microorganisms over an exponential stretching sheet. *Journal of Nanofluids 10*, 3 (2021), 327–338.

[54] Narayana, P. V. S., Babu, D., and Venkateswarlu, B. Soret and dufour effects on mhd radiative heat and mass transfer flow of a jeffrey fluid over a stretching sheet. *Frontiers in Heat and Mass Transfer 8* (2017).

[55] Narayana, P. V. S., and Venkateswarlu, B. Influence of variable thermal conductivity on mhd casson fluid flow over a stretching sheet with viscous dissipation, soret and dufour effects. *Frontiers in Heat and Mass Transfer 7*, 1 (2016).

[56] Narla, V., Biswas, C., and Rao, G. A. Entropy analysis of mhd fluid flow over a curved stretching sheet. In *AIP Conference Proceedings* (2020), vol. 2246, AIP Publishing LLC, p. 020099.

[57] Nawaz, M., Naz, R., and Awais, M. Magnetohydrodynamic axisymmetric flow of casson fluid with variable thermal conductivity and free stream. *Alexandria engineering journal 57*, 3 (2018), 2043–2050.

[58] Nayak, B., Mishra, S. S., and Krishna, G. G. Chemical reaction effect of an axisymmetric flow over radially stretched sheet. *Propulsion and Power Research 8*, 1 (2019), 79–84.

[59] Nazari, M. A., Salem, M., Mahariq, I., Younes, K., and Maqableh, B. B. Utilization of data-driven methods in solar desalination systems: a comprehensive review. *Frontiers in Energy Research* (2021), 541.

[60] Oyelakin, I. S., Mondal, S., and Sibanda, P. Unsteady casson nanofluid flow over a stretching sheet with thermal radiation, convective and slip boundary conditions. *Alexandria engineering journal 55*, 2 (2016), 1025–1035.

[61] Pal, D., Mandal, G., and Vajravalu, K. Soret and dufour effects on mhd convective–radiative heat and mass transfer of nanofluids over a vertical non-linear stretching/shrinking sheet. *Applied Mathematics and Computation 287* (2016), 184–200.

[62] Pal, D., and Mondal, S. K. Mhd nanofluid bioconvection over an exponentially stretching sheet in the presence of gyrotactic microorganisms and thermal radiation. *BioNanoScience 8*, 1 (2018), 272–287.

[63] Pedley, T. J., Hill, N. A., and Kessler, J. O. The growth of bioconvection patterns in a uniform suspension of gyrotactic micro-organisms. *Journal of Fluid Mechanics 195* (1988), 223–237.

[64] Pham, D. T., Liu, X., Pham, D. T., and Liu, X. Dynamic system identification using recurrent neural networks. *Neural Networks for Identification, Prediction and Control* (1995), 47–61.

[65] Piscopo, M. L., Spannowsky, M., and Waite, P. Solving differential equations with neural networks: Applications to the calculation of cosmological phase transitions. *Physical Review D 100*, 1 (2019), 016002.

[66] Ramudu, A. C. V., Kumar, K. A., V. Sugunamma, V., and Sandeep, N. Impact of soret and dufour on mhd casson fluid flow past a stretching surface with convective–diffusive conditions. *Journal of Thermal Analysis and Calorimetry 147*, 3 (2022), 2653–2663.

[67] Rashidi, M. M., Alhuyi, N. M., Mahariq, I., and Ali, N. Modeling and sensitivity analysis of thermal conductivity of ethylene glycol-water based nanofluids with alumina nanoparticles. *Experimental Techniques* (2022), 1–8.

[68] Rashidi, M. M., Nazari, M. A., Mahariq, I., Assad, M. E. H., Ali, M. E., Almuzaiqer, R., Nuhait, A., and Murshid, N. Thermophysical properties of hybrid nanofluids and the proposed models: An updated comprehensive study. *Nanomaterials 11*, 11 (2021), 3084.

[69] Ray, A. K., Vasu, B., Anwar, B. O., Gorla, R. S. R., and Murthy, P. V. S. N. Magneto-bioconvection flow of a casson thin film with nanoparticles over an unsteady stretching sheet: Ham and gdq computation. *International Journal of Numerical Methods for Heat & Fluid Flow* (2019).

[70] Raza, J. Thermal radiation and slip effects on magnetohydrodynamic (mhd) stagnation point flow of casson fluid over a convective stretching sheet. *Propulsion and power research 8*, 2 (2019), 138–146.

[71] Reddy, J. V. R., Kumar, K. A., Sugunamma, V., and Sandeep, N. Effect of cross diffusion on mhd non-newtonian fluids flow past a stretching sheet with non-uniform heat source/sink: A comparative study. *Alexandria engineering journal 57*, 3 (2018), 1829–1838.

[72] Reddy, N. N., Rao, V. S., and Reddy, B. R. Chemical reaction impact on mhd natural convection flow through porous medium past an exponentially stretching sheet in presence of heat source/sink and viscous dissipation. *Case studies in thermal engineering 25* (2021), 100879.

[73] Reddy, P. B. A., and Das, R. Estimation of mhd boundary layer slip flow over a permeable stretching cylinder in the presence of chemical reaction through numerical and artificial neural network modeling. *Engineering Science and Technology, an International Journal 19*, 3 (2016), 1108–1116.

[74] Reza-E-Rabbi, S., Arifuzzaman, S., Sarkar, T., Khan, M. S., and Ahmmed, S. F. Explicit finite difference analysis of an unsteady mhd flow of a chemically reacting casson fluid past a stretching sheet with brownian motion and thermophoresis effects. *Journal of King Saud University-Science 32*, 1 (2020), 690–701.

[75] Sabir, Z., Akhtar, R., Zhiyu, Z., Umar, M., Imran, A., Wahab, H. A., Shoaib, M., and Raja, M. A. Z. A computational analysis of two-phase casson nanofluid passing a stretching sheet using chemical reactions and gyrotactic microorganisms. *Mathematical Problems in Engineering 2019* (2019).

[76] Sahari, M. F., and Nezhad, A. H. Estimation of the flow and heat transfer in mhd flow of a power law fluid over a porous plate using artificial neural networks. *Middle East J. Sci. Res 22*, 9 (2014), 1422–1429.

[77] Sakiadis, B. C. Boundary-layer behavior on continuous solid surfaces: I. boundary-layer equations for two-dimensional and axisymmetric flow. *AiCHE Journal 7* (1961), 26–28.

[78] Sakiadis, B. C. Boundary-layer behavior on continuous solid surfaces: Ii. the boundary layer on a continuous flat surface. *AICHE Journal 7* (1961), 221–225.

[79] Sankad, G., Maharudrapppa, I., and Dhange, M. Bioconvection in casson fluid flow with gyrotactic microorganisms and heat transfer over a linear stretching sheet in presence of magnetic field. *Advances in Mathematics: Scientific Journal 10*, 1 (2021), 155–169.

[80] Saravana, R., Sailaja, M., and Reddy, R. H. Effect of aligned magnetic field on casson fluid flow over a stretched surface of non-uniform thickness. *Nonlinear Engineering 8*, 1 (2019), 283–292.

[81] Shahzad, A., Ali, R., Hussain, M., and Kamran, M. Unsteady axisymmetric flow and heat transfer over time-dependent radially stretching sheet. *Alexandria Engineering Journal 56*, 1 (2017), 35–41.

[82] Shahzad, A., Gulistan, U., Ali, R., Iqbal, A., Benim, A. C., Kamran, M., Khan, S. U.-D., Khan, S. U.-D., and Farooq, A. Numerical study of axisymmetric flow and heat transfer in a liquid film over an unsteady radially stretching surface. *Mathematical Problems in Engineering 2020* (2020).

[83] Sharada, K., et al. Mhd mixed convection flow of a casson fluid over an exponentially stretching surface with the effects of soret, dufour, thermal radiation and chemical reaction. *World Journal of Mechanics 5*, 09 (2015), 165.

[84] Shateyi, S., Mabood, F., and Lorenzini, G. Casson fluid flow: Free convective heat and mass transfer over an unsteady permeable stretching surface considering viscous dissipation. *Journal of Engineering Thermophysics 26*, 1 (2017), 39–52.

[85] Sohail, M., Shah, Z., Tassaddiq, A., Kumam, P., and Roy, P. Entropy generation in mhd casson fluid flow with variable heat conductance and thermal conductivity over non-linear bi-directional stretching surface. *Scientific Reports 10*, 1 (2020), 1–16.

[86] Soret, C. *Influence de la température sur la distribution des sels dans leurs solutions.* 1880.

[87] Sparrow, E. M., and Cess, R. D. *Radiation Heat Transfer: Augmented Edition.* Routledge, 2018.

[88] Sreelakshmi, K., Sarojamma, G., and Murthy, J. V. Homotopy analysis of an unsteady flow heat transfer of a jeffrey nanofluid over a radially stretching convective surface. *Journal of Nanofluids 7*, 1 (2018), 62–71.

[89] Sreenadh, S., Babu, V. R., Krishna, G. G., Mishra, S., and Srinivas, A. Entropy generation on mhd flow and heat transfer of non-newtonian fluid flow over a non-linear radially stretching sheet. *International Journal of Engineering & Technology 7*, 4.10 (2018), 863–868.

[90] Talaván, P. M., and Yáñez, J. A continuous hopfield network equilibrium points algorithm. *Computers & Operations Research 32*, 8 (2005), 2179–2196.

[91] Ullah, I., Khan, I., and Shafie, S. Soret and dufour effects on unsteady mixed convection slip flow of casson fluid over a nonlinearly stretching sheet with convective boundary condition. *Scientific Reports 7* (2017).

[92] Ullah, I., Shafie, S., and Khan, I. Effects of slip condition and newtonian heating on mhd flow of casson fluid over a nonlinearly stretching sheet saturated in a porous medium. *Journal of King Saud University-Science 29*, 2 (2017), 250–259.

[93] Vijaya, N., Arifuzzaman, S. M., Sai, N. R., and Rao, C. M. Analysis of arrhenius activation energy in electrically conducting casson fluid flow induced due to permeable elongated sheet with chemical reaction and viscous dissipation. *Frontiers in Heat and Mass Transfer (FHMT) 15*, 1 (2020).

[94] Wang, Q. F. Theoretical and computational issues of optimal control for distributed hopfield neural network equations with diffusion term. *SIAM Journal on Scientific Computing 29*, 2 (2007), 890–911.

[95] Xu, C., Wang, C., Ji, F., and Yuan, X. Finite-element neural network-based solving 3-d differential equations in mfl. *IEEE Transactions on Magnetics 48*, 12 (2012), 4747–4756.

[96] Yadav, N., Yadav, A., Kumar, M., et al. *An introduction to neural network methods for differential equations*, vol. 1. Springer, 2015.

[97] Zhou, J.-C., Abidi, A., Shi, Q.-H., Khan, M. R., Rehman, A., Issakhov, A., and Galal, A. M. Unsteady radiative slip flow of mhd casson fluid over a permeable stretched surface subject to a non-uniform heat source. *Case Studies in Thermal Engineering 26* (2021), 101141.

[98] Ziaei-Rad, M., Saeedan, M., and Afshari, E. Simulation and prediction of mhd dissipative nanofluid flow on a permeable stretching surface using artificial neural network. *Applied Thermal Engineering 99* (2016), 373–382.